TECHNISCHE UNIVERSITÄT MÜNCHEN

Lehrstuhl für Biologische Bildgebung

The application of *in vivo* and *ex vivo* multispectral epi-fluorescence imaging for the preclinical discovery and development of monoclonal antibodies in tumor xenograft models

Michael Dobosz

Vollständiger Abdruck der von der Fakultät für Medizin der Technischen Universität München zur Erlangung des akademischen Grades eines

Doktor der Naturwissenschaften (Dr. rer. nat.)

genehmigte Dissertation.

Vorsitzende:	Univ.-Prof. Dr. G. Multhoff
Prüfer der Dissertation:	1. Univ.-Prof. Dr. V. Ntziachristos
	2. Univ.-Prof. Dr. H. J. Wester

Die Dissertation wurde am 03.06.2014 bei der Technischen Universität München eingereicht und durch die Fakultät für Medizin am 17.09.2014 angenommen.

Statutory Declaration

I hereby declare that this thesis has been written by myself without any external unauthorized help, that it has been neither presented to any institution for evaluation nor previously published in its entirety or in parts. Any parts, words or ideas, of the thesis, however limited, and including tables, graphs, maps etc., which are quoted from or based on other sources, have been acknowledged as such without exception.

Penzberg, 03.06.2014

.....

(Michael Dobosz)

Acknowledgment

PhD research often appears a solitary undertaking. However, it is impossible to maintain the degree of focus and dedication required for its completion without the help and support of the kind people. I wish to express my sincere appreciation to those who have contributed to this thesis and supported me during this long journey.

First and foremost, I would like to express my heartfelt gratitude to my supervisor and mentor Dr. Werner Scheuer from Roche Diagnostics GmbH in Penzberg and Prof. Vasilis Ntziachristos from the Institute for Biological and Medical Imaging (IBMI) at the Technical University of Munich. Both arranged, initiated, and instructed the execution of this thesis.

Werner, your almost unlimited passion and enthusiasm about molecular imaging arouse my interest about this technology and brought me eventually into this scientific field. During the PhD thesis, I really enjoyed our unburdened working relationship and appreciate your constant support, encouragement, patience, and the many insightful scientific midnight discussions. It is a great pleasure for me to work with you and being a part of the Roche imaging team.

Vasilis, I am extremely grateful for giving me the research opportunity at IBMI and being the mentor for my PhD thesis. Many thanks for your scientific advice and constant support and I also very much appreciate that you gave me the freedom to pursue my scientific goals at Roche and keep me on a long leash. Your scientific work was always a great inspiration for me and thus I hope that we can accomplish further collaborative projects in the future.

I am greatly indebted to my wonderful colleagues from the Roche/Penzberg imaging group, in particular Ute Haupt, Anja Renner, Steffen Strobel, Franz Osl, Thomas Weber, Stefan Bissinger, and Dr. Thomas Pöschinger, for their constant help, support, constructive critiques and recommendations. A special thank goes out to Steffen, who created and programmed the quantification software for the ultramicroscopy and brought my basic understanding of image processing and analysis to a totally new level. I am very thankful that I shared the lab and also my spare time with such great people. Guys, I couldn't have done it without you!

A very special thank goes to Dr. Rudolf Vogel and Axel Wessner form the Roche/Penzberg chemistry department for the labeling and purification of the different antibody formats and imaging compounds. I further appreciate the help and support of the Roche/Penzberg histology department, especially Dr. Natascha Rieder, Adriana Zabarella, Gabriele Dietmann, and Marc Zätschky, for providing me histological protocols and performing different tissue staining's. I also want to acknowledge all people form the Roche/Penzberg animal facility for supporting my *in vivo* experiments and providing ideal animal care. Special thanks to all my wonderful colleagues at Roche and IBMI who in some way supported and contributed to the progress of this work.

Finally and above all, I would like to acknowledge the most important person in my life - my girlfriend Susanne and my daughter Lara. The past several years have not been an easy ride, both academically and personally, but their unconditional love, encouragement and support were always been a constant source of strength and inspiration. I truly thank Susanne for standing by my side, during the good and bad times of my life.

I would like to dedicate this work to my deceased mother, who left me too soon. I hope that this work makes you proud.

Abstract

Today's discovery and development process of therapeutic monoclonal antibodies is very complex and cost-intensive, requires long development periods ranging from 8-12 years and is associated with high attrition rates. The standard procedures for the preclinical development of new antibodies, such as blood analysis and conventional immunohistochemistry, provide only a limited insight into the complex tumor biology which aggravates an effective evaluation and selection of clinical relevant antibodies.

The present thesis is dedicated to improve established standard procedures in preclinical drug development by using *in vivo* and *ex vivo* fluorescence imaging modalities. These inexpensive, fast, easy to handle, and radiation-free imaging techniques provide the ability for the multispectral detection of relevant tumor and drug parameters on a macroscopic and microscopic scale. A detailed and profound examination of the great potential of these imaging methods in the application field of preclinical monoclonal antibody development was initially verified in the present work.

The combination of eye and whole-body fluorescence *in vivo* imaging enables not only a non-invasive, longitudinal, and high throughput measurement of pharmacokinetic serum profiles of fluorescent labeled substances through the animals eye, but rather to capture their biodistribution, penetration, accumulation, and clearance in subcutaneous tumor xenografts. The subsequent *ex vivo* tumor analysis provided detailed cellular information regarding the penetration behavior and specific antibody-target interaction. To overcome the existing limitation of two-dimensional single tumor tissue slice analysis, multispectral fluorescence ultramicroscopy in combination with a novel set of custom-developed image analysis algorithms were used for the three-dimensional visualization and automatic quantification of different tumor and drug parameter.

The combination of the different *in vivo* and *ex vivo* imaging techniques enabled the perfect determination of important parameters for the preclinical antibody development process, such as the expression level of tumor cell receptors and the evaluation of the binding site, affinity, and specificity of monoclonal antibodies to the relevant tumor target. These modalities could also prioritize the best therapeutic antibody, select the most suitable xenograft model, and determine the optimal treatment dosage and application time point for a preclinical efficacy study. The imaging results correlated perfectly with the corresponding efficacy data and by analysis of already approved therapeutic antibody formats (such as Trastuzumab and Pertuzumab) the clinical relevance of the performed imaging experiments was illustrated. Furthermore, multispectral fluorescence ultramicroscopy in combination with a novel automatic quantification software was applied in to the field of tumor analysis and provided unprecedented three-dimensional and quantitative insights into whole tumors with cellular resolution.

The present work could clearly demonstrate that the combination of *in vivo* and *ex vivo* epi-fluorescence imaging modalities is a great and powerful tool for the preclinical discovery and development process of monoclonal antibodies. These imaging techniques provide the possibility for a profound determination and analysis of preclinical relevant tumor and drug parameters and therefore enable a fast and purposeful selection of clinical relevant antibodies.

Contents

1 Introduction

1.1 The drug discovery and development process of biologics

Besides cardiovascular and infectious diseases, cancer is the most common cause of death in the world. In a recently published study, the total predicted number of cancer death in the European Union in 2013 is 1,314,296 person (737 747 men and 576 489 women). Comparing this prognosis with the mortality data of 2009, it would be an increase of 2.5 %. Considering the increased age-standardized mortality rate (ASR) of affected persons in this elicitation, however, a distinct anti-trend is showing. In the past five years, ASRs for men decreased by 6 % and for women by 4 %. This development can be mainly attributed to the increasing progress in cancer check-ups, early diagnosis and the development of new innovative treatment methods and therapeutic approaches [1, 2].

With the grand scientific commitment of universities, institutes, biotech- and pharmaceutical companies over the last decades, breakthrough success in tumor biology research could be celebrated. The resultant deeper understanding of tumor development, growth and spread; lead to the development of highly diverse therapeutic approaches. Besides the classic „three main pillars“ of cancer therapy: (i) the surgical removal of the tumor tissue, (ii) the radio- and (iii) chemotherapy; target-oriented cancer therapies become more and more important. In principle, these target specific therapeutics are subdivided in small-molecules and biologics, including monoclonal antibodies. Instead of a broad, uniform and unspecific therapy, both categories are specifically directed against biological and cytological characteristics of the tumor tissue. Across the targeted interaction and/or the selective binding with tumor relevant structures, these therapeutics are able to specifically block signaling pathways of proliferation and/or angiogenesis and can therefore prevent uncontrolled tumor growth [3]. Furthermore, some of these molecules are able to induce directly tumor cell apoptosis or to stimulate and activate the endogenous immune defense [4, 5].

1.1.1 Monoclonal antibodies in cancer therapy

In general, intact antibody formats (such as IgA, IgD, IgE, IgM and IgG) are highly specific targeting reagents, which provide our key defense against pathogenic organisms and toxins. They can be roughly divided in two different groups by means of their binding behavior. One group recognizes soluble messengers in the blood (e.g. vascular endothelial growth factor [VEGF] is detected by the anti-VEGF mAb Bevacizumab), whereas the others are directed against protein and receptor structures on the tumor surface (e.g. human epidermal growth factor receptor 2 [HER2] is detected by the anti-HER2 mAb Trastuzumab). Most of the monoclonal antibodies used today for therapeutic purpose, correspond to the classic IgG-antibody format (Y-shaped) with a molecular weight of approx. 150 kDa [6, 7].

The bivalent IgG structure allows the detection of two antigens, which increases their functional affinity and avidity on many cell-surface receptors and antigens. Furthermore, the interaction of the mAb Fc domain with Fc- and/or Fc-γ receptors provide long serum half live

and recruits cytotoxic effector functions through the complement system [8, 9]. The structural homology between humanized and endogenous antibodies reduces the immunogenicity and the range of unwanted side effects [10]. Beside the classical IgG antibody format, different antibody related molecules currently being investigated, including Fc fusion proteins, antibody fragments (Fab_2, Fab, Fv), single chain antibodies, protein scaffolds, immunoliposomes and bi-, tri-, and tetra-specific antibodies [11-15]. These new antibody formats captivate with improved pharmacokinetic properties (such as biodistribution, tumor penetration, serum half-life, and blood clearance) and/or possess the capability to attack several tumor antigens with multiple binding sites. The improved penetration behavior of such therapeutic agents and consequently, its enhanced availability in the tumor region, combined with a specific blocking of different signal transduction pathways, increases the therapeutic pressure on the tumor cells and reduces possible escape mechanisms.

In the past decades, the development of different monoclonal antibody formats in particular showed great therapeutic success in a number of clinical applications, leading to enormous growth rates in this pharmaceutical market segment [1, 16, 17]. In 2010, sales of biologics exceeded for the first time the 100 billion US-dollar (USD) limit. Five out of ten of the world's top selling drugs are now antibody based molecules [18].

1.1.2 Problems and challenges of drug discovery and development

Despite this success and the great progress in the development of different targeted anti-cancer agents and therapies, the pharmaceutical industry faces huge challenges and problems. Today's development process for such biological therapeutics is very complex, cost-intensive and requires long development periods. Estimated development costs of a drug approved by the U.S. Food and Drug Administration (FDA) are currently adding up to nearly 1 billion USD with a development period of 10-12 years [19]. One of the biggest problems, however, is the very high attrition rates, which reflects the level of failures of new drug candidates during the drug development process. About 5% of the anticancer drugs that reach a clinical Phase I study gain a marketing authorization [20, 21]. Even more, it has been reported that only 1 in 10,000 preclinical compounds ever reach the market [22]. The reasons for such high attrition rats are very versatile and include scientific, financial and political reasons. Numerous solution approaches have been proposed to find a way out of „The Valley of Death in anticancer drug development" and how to select the best drug candidate in preclinical and early clinical studies [23-29].

The more effective organization and structuring of the preclinical drug development is a key position to overcome these problems. This early and very complex development process splits up in the following sections: (i) identification and validation of tumor relevant target structures, (ii) the development, optimization, expression, purification and characterization of suitable substances, and (iii) the *in vitro* and *in vivo* selection of appropriate candidates, as well as the validation of their therapeutic effect and toxicity. Especially the *in vivo* evaluation in the animal model plays an important but also critical role, as the behavior and interaction of a new therapeutic agent is initially analyzed in a living organism.

The preclinical *in vivo* studies provide pharmacokinetic and pharmacodynamic drug information that allows inferences about a specific antigen binding, the modulation of the

target structure, and the resultant therapeutic treatment effect. In an ideal situation, a suitable *in vivo* model should deliver the following information about the therapeutic agent: the absorption, distribution, metabolism and clearance of the drug; dose-related effects on drug plasma levels and tumor target modulation; and also dose-related anti-tumor efficacy [30, 31]. Through these parameters, an ideal drug candidate with the best therapeutic efficacy and the slightest toxic side-effects is going to be identified [32]. Even more, the preclinical *in vivo* information of pharmacokinetic and pharmacodynamic behavior of a drug, can be used to plan the starting dose and schedule of subsequent clinical phase I studies [30].

However, the validity of the produced data sets and its transferability to the clinical application is very much depending on the chosen experimental model and the applied analysis method. The processing of the large and various number of biological target structures and consequential the therapeutic molecules, requires a myriad of preclinical animal models (such as murine tumor models, *in vivo* hollow fiber assay, s.c. human tumor xenografts, orthotopic and metastatic human tumor xenografts and/or genetically engineered cancer models) [33-36]. This great variability of *in vivo* models makes it nearly impossible to standardize the preclinical development process, and at the same time, raises the question about the performance and predictive value of commonly used *in vivo* xenograft models in predicting clinical efficacy of molecularly targeted drugs. Today, the consent about universal guidelines regarding the extent of such preclinical *in* vivo studies and the definition of solid parameter for the selection of suitable drug candidates is only partly available [30].

If we manage to orientate our preclinical models more towards the clinical situation and receive, by means of new innovative technologies, deeper insights and a more universal understanding for the biological and molecular origins of cancer disease and also the complex interaction between the therapeutic agent and its target structure, we will be able to prioritize a suitable drug candidate more efficiently and also enhance the predictability for his clinical success [37, 38].

1.1 Molecular imaging in drug development

In the last decades, innovative developments in the field of molecular imaging revolutionized preclinical and clinical cancer research and influenced the drug discovery and development process to a great extent. This non-invasive and repetitive technology opened in-depth insights into tumor biology and provides detailed information about the complexity, diversity and *in vivo* behavior of cancer. Beside the morphological/anatomical characterization of tumors in living organisms, the development of novel reporter gen technology, targeted and activatable ("smart") probes enables specific target assessment and molecular analysis. Such molecular fingerprint of tumors visualizes the expression and activity of specific molecules (e.g. proteins, proteases, protein kinases, receptors) and biological processes (e.g. metabolism, proliferation, angiogenesis, hypoxia, apoptosis, and metastasis) that influence tumor behavior. Furthermore, molecular imaging provides the potential for longitudinal monitoring of distribution, accumulation, binding specificity, metabolism and clearance of labeled drugs. These information can be used to understand disease mechanisms at the molecular level; helping to design, characterize and optimize therapeutic drugs and strategies; contribute decision making and therefore enhance the drug discovery and development process [39-41].

1.1.3 Overview of the different molecular imaging technologies

Nearly all of today's imaging systems were initially designed for clinical applications, but the development of more suitable animal models, contrast agents and new hardware design blazed the trail for classical imaging methods into preclinical research. Down scaled *in vivo* imaging systems possess a higher spatial/temporal resolution and detection sensitivity and in combination with novel imaging probes they can quantify and characterize biological processes at a cellular and subcellular level in intact animals [42, 43]. The basic principle of any imaging process is the interaction of energetic particles (x-ray, positrons, photons or sound waves) with the examining tissue, which provides anatomical, physiological, cellular and molecular information of macroscopic, mesoscopic and microscopic resolution [44].

Macroscopic imaging methods like computed tomography (CT), magnetic resonance imaging (MRI) and ultrasound are used to detect morphological and anatomical tissue variances, in both preclinical and clinical applications. They offer relatively high spatial resolution, deep tissue penetration and excellent soft tissue contrast, but the major limitation is the poor sensitivity. Furthermore, these imaging modalities are incapable to detect pharmacokinetic drug information, drug-target interaction and the resulting molecular changes inside the tumor [45-47]. Non-invasive visualization of such parameter can only be realized by positron-emission tomography (PET), single-photon-emission computed tomography (SPECT) or optical imaging (OI). An administrated reporter probe (labeled with radioactive isotopes or fluorochromes) can be easily targeted to report on specific molecular processes *in vivo*. The tender spot of these methods are the relatively low spatial resolution [45-47]. The combination of morphological/anatomical and molecular imaging modalities (e.g. PET-CT, PET-MRI, SPECT-CT, FMT-CT) unifies the strength of both fields and thereby enables molecular and structural tumor analysis at an early point of disease [48, 49].

The selection of the most suitable imaging modality to answer a specific biological question is driven by many factor, including: (i) biological (animal model, small molecule or protein, anatomical or molecular information), (ii) chemical (radioactive and/or non-radioactive tracer, labeling), (iii) technical (spatial/temporal resolution, sensitivity, high throughput, preclinical and clinical translation), and (iv) financial aspects (Table 1) [44].

Imaging methods, like PET, CT, MRI, and their various combinations, provide the large advantage of quantitative parameter analysis and the possibility to transfer preclinical data into the clinical setting. On the other hand, high acquisition and follow-up coasts, the usage of nuclear radiation and isotopes for image-generation (CT and PET), no multi-channel imaging, and especially long measurement times and associated low throughput rates (e.g PET: 1-2 animals per 10-30 min scan) are limiting their application and prevent broad spreading in preclinical research. In addition to this, the resolution of histological PET analysis is not sufficient to reach cellular resolution and thus unspecific penetration and circulation of PET imaging probes cannot be distinguished from a specific antigen binding [50].

Table 1: Overview of the different imaging modalities

Technique	Resolution	Depth	Time	Quantitation	Multi channel imaging	Imaging agents	Target	Cost	Preclinical use	Clinical use
MRI	10-100 µm	No limit	Min to hours	Absolute	No	Paramagnetic chelates, Magnetic particles	Anatomical, physiological, molecular	$$$	Yes	Yes
CT	50 µm	No limit	Sec to min	Absolute	No	Iodinated molecules, Gold particles	Anatomical, physiological molecular[2]	$$	Yes	Yes
Ultrasound	50 µm	cm	Sec to min	Absolute	No	Microbubbles	Anatomical, physiological molecular[2]	$$	Yes	Yes
PET	1-2 mm	No limit	Min to hours	Absolute	No	^{11}C-, ^{13}N-, ^{15}O-^{18}F-, ^{64}Cu-, ^{68}Ga-, ^{124}I-labled compounds	Physiological, molecular	$$$	Yes	Yes
SPECT	1-2 mm	No limit	Min to hours	Absolute	Two	^{99m}Tc-, ^{111}In-, ^{131}I-labled compounds, ^{67}Ga, ^{201}Tl	Physiological, molecular	$$	Yes	Yes
OI-FRI	1-2 mm	< 1 cm	Sec to min	Relative	Multiple	Fluorescent proteins, fluorochromes	Physiological, molecular	$	Yes	Yes
OI-FMT	1-2 mm	< 10 cm	min	Absolute	Multiple	NIR-fluorochromes	Physiological, molecular	$$	Yes	Yes
OI-BLI	Several mm	cm	min	Relative	Multiple	Luciferins	Molecular	$$	Yes	No
OI-IVM (confocal, multi-photon)	1 µm	< 400-800 µm	Sec to hours	Relative	Multiple	Fluorescent proteins, fluorochromes	Anatomical, physiological, molecular	$$$	Yes	Yes

Cost of the imaging system: $ < 150 K; $$ 150–300 K; $$$: > 300 K. The Resolution and Cost columns refer to high-resolution, small animal imaging systems and are different for clinical imaging systems. Quantitation: "absolute" and "relative" refer to techniques that generate signals that are depth independent and dependent, respectively. "Relative" quantitation techniques typically require extensive controls; however, some of them (e.g., multi-photon microscopy, MPM) can be used to derive truly quantitative parameters (e.g., cell velocity, interaction time). Target: area(s) that a given imaging modality interrogates; [2] a limited number of molecularly targeted agents has been described. BLI, bioluminescence imaging; C, carbon; Cu, copper; CT, computed tomography; F, fluorine; FRI, fluorescence reflectance imaging; FMT, fluorescence molecular tomography; Ga, Gallium; I, iodine; In, indium; IVM, intravital microscopy; MRI, magnetic resonance imaging; N, nitrogen; NIR, near infrared; O, oxygen; OI, optical imaging; PET, positron-emission tomography; SPECT, single-photon-emission computed tomography; Tl, thallium ^{99m}Tc, technetium metastable. The table was adapted from different publication [39, 42, 44, 48, 51].

In comparison to this, optical imaging modalities, such as fluorescent based imaging, are inexpensive and easy to handle; permit non-radiative, highly sensitive, and multi-channel imaging; possess simple conjugation chemistry; and provide the possibility for high throughput measurements (up to 100 animals per hour) [50]. The disadvantages of those semiquantitative imaging methods are the strong absorption and scattering of fluorescent light in tissue and consequentially the limited penetration depth of several millimeters. These aspects reduce the application of optical imaging mainly to the investigation of subcutaneous tumor models, but since those are the most commonly used xenografts in preclinical drug development, fluorescence imaging is eminently suitable for PK and PD *in vivo* studies. Another important point, which prioritizes this modality for the preclinical drug discovery and development process, is the possibility for a direct comparison between *in vitro*, *in vivo* and *ex vivo* imaging results using the same fluorescent labeled molecule for investigation.

1.2 Optical imaging technologies

No other technological development has changed and influenced our biological understanding in such fundamental way as optical imaging. Since the construction of the first elementary light microscope (by Zacharias & Hans Jansen, 1590) and the first description of cellular structures (by Robert Hooke, 1665) a rapid development, both in the technological and biological sector, took place. Today, a great number of different optical imaging modalities, in particular fluorescence imaging, are in daily research and clinical practice, where they provide us with bright field, bioluminescence and fluorescence light microscopic, mesoscopic and macroscopic information. Because of their common basic physical principle, the different optical imaging technologies can be excellently combined. The symbiosis of *in vitro*, *in vivo* and *ex vivo* optical imaging modalities allows a universal consideration of biological processes and a deeper analysis of existing coherences. These methods open up the possibility to analyze morphological/anatomical, physiological, molecular, genetic and pharmacokinetic questions at single cells, 3D cell cultures, in single tissue slices, compact tissue samples and/or in a living organism. Especially, non-invasive optical imaging in small animals gains more and more relevance, because it is close to the clinical situation and thereby reflecting biological complexity in a much better way. The possibility to monitor biological and molecular processes in the intact organism is very attractive for basic research but even more so for pharmaceutical companies, who can use the techniques for proof-of-concept and proof-of-efficacy studies. Because of their variability and specificity, optical imaging modalities are the most common imaging tools in today's preclinical research and they also find more and more the way in clinical application [52, 53].

The following sections summarize the basic principle and limitations of fluorescence reflectance imaging and fluorescence tomography, gives an overview of different microscopic and macroscopic imaging modalities and highlight areas of application.

1.3 Fluorescence imaging

Basic principle

In the year 1852 the mathematician and physician Georg Gabriel Stokes defined the term of fluorescence [54]. He describes the ability of certain minerals (e.g. fluorspar) to absorb light at a particular wavelength and almost immediately re-emit at a longer, lower-energy wavelength after a short dwelling time. The shift between the excitation and emission wavelength caused by the dissipation of energy is termed Stokes-Shift. In the following centuries this fundamental principle of fluorescent light emitting molecules led to the development of various fluorochromes and fluorescent proteins and in combination with novel labeling techniques, highly specific molecular targeting probes and advanced macroscopic optical imaging modalities, which build the basis of modern *in vivo* fluorescence molecular imaging [44]. The process of fluorescence imaging always needs the following four basic requirements: (i) an excitation light source, (ii) a fluorochrome (single or labeled to a molecule), (iii) specific filter (to remove the unspecific excitation and/or autofluorescence light) and (iv) a highly sensitive detector.

Imaging probes

The development of various types of multi-functional imaging probes enables the specific and non-invasive detection of various tumor targets in living animals. The basic element of every imaging probe is the reporter (e.g. fluorochrome, fluorescence protein, and/or nanoparticle). Such a fluorescent particle can be attached to other molecules (such as antibodies, antibody fragments, peptide varieties, and/or small molecules) [55-57] with high affinity to specific targets (defined as direct imaging) or is expressed as a fluorescent protein in genetically engineered organisms (defined as indirect imaging).

Direct fluorescence imaging

Direct fluorescence imaging strategies use active (reporter-molecule construct) and/or activatable imaging probes (reporter-quencher-molecule construct) for target detection. The latter, a fluorescence absorbing molecule (e.g. fluorochrome or quencher) is attached with an enzyme-specific peptide substrate in close proximity to the reporter; thereby "quenching" the emitted fluorescence from the excited reporter. After a subsequent enzyme-substrate reaction the specific peptide sequence is cleaved and the fluorescence signal is activated. In comparison to conventional "always on" imaging agents, such techniques provide higher target to background ratios which improve contrast and increase detection sensitivity [58]. Furthermore, they are used to determine the expression and activation status of genes and proteins and also identify the interaction between macromolecules [59-61]. Another variety of imaging probes are dye-encapsulated nanoparticles which are conjugated on the surface with tumor specific ligands (such as antibodies, proteins, peptides and small molecules) for tumor detection [62].

Today different reporter systems are available including inorganic and organic molecules. In the last years, inorganic molecules (e.g. quantum dots, nanoparticals) have rapidly emerged as fluorescent reporter probes in biological research [63, 64]. Quantum dots (QDs) are nanoscale-sized semiconductor nanocrystals with a particle size ranging from 2-50 nm. They have a broad excitation wavelength rang (400-600 nm) and the narrow-band emission depending on the physical particle size. QDs possess a high intrinsic brightness and photostability, but their heavy metal cores (such as Cd, Se) causes fundamental cytotoxicity problems therefore challenges *in vivo* applications [65-67]. Furthermore, the manufacturing of those particles cost-prohibitive and includes difficulties in reproducibility and comparability [68].

Because of those limitations organic molecules are still the most qualified reporter systems both in preclinical and clinical practices [69-71]. A wide range of fluorochromes are commercially available and their improved photo-physical properties as well as the availability for covalent or non-covalent conjugation (via ε-amino group of lysine, α-amino group of the N-terminus, thiol group of cystein) [72] to cancer-targeting molecules, let them become the standard tool in molecular imaging. Nevertheless, only a few of those fluorescent dyes are suitable for *in vivo* applications. Ideal fluorochromes for whole-body fluorescence imaging have to fulfill the following aspects: (i) emission spectrum in the NIR range to reduce autofluorescence and improve penetration behavior, (ii) large Stokes-Shift to reduce spectral overlapping between excitation and emission spectrum, (iii) high molar extinction coefficient and quantum yield for intense fluorescence, (iv) sufficient chemical and photostability under imaging conditions, and (v) good water solubility to avoid dye aggregation in aqueous

environment [62, 73]. Large efforts to generate molecules with such properties have been undertaken; leading to the development of novel NIR-dyes (such as cyanine dyes, squaraine, phthalocyanines, porphyrin derivatives and borondipyrromethane (BODIPY) analogues) with improved chemical and optical characteristics [74-80].

Indirect fluorescence imaging

Another class of organic reporter molecules which play an important role in molecular imaging includes fluorescent proteins (FPs). In the last decades those genetically encoded proteins (such as the green fluorescent protein [GFP] which was isolated from the jellyfish *Aequorea victoria*) became a popular tool in cell and molecular biology to study the expression and regulation of different genes and proteins [81, 82]. For this, the GFP encoding reporter gene is genetically integrated into a regulatory promoter sequence of the cell genome. The transcription and translation of this specific protein sequence leads to the simultaneous expression of the cell protein and fluorescent protein. Measuring the fluorescent protein intensity provides indirect information regarding the activation, expression and regulation of target genes. Furthermore, the location and distribution of a target protein can be visualized *in vivo* by genetically integrating GFP into the target protein structure without changing functionality (such a protein is called fusion protein) [83]. Today, a number of multiple spectral GFP-like proteins are available ranging from blue, cyan, green, yellow-green, orange, red to far-red [2,3]. Those multiple fluorescent proteins enable the investigation of protein-protein interactions using fluorescence resonance energy transfer (FRET) [84-86].

The diversity of those reporter molecules enables researchers to monitor complex coherences and multiple interactions of genes and proteins in living organisms. FPs are resident in many biological areas including structural (organism- [87], cell- [88], organelle- [89], nuclide acid- [90], and protein-labeling [91]) and functional (promoter activity [92], protein-protein interaction [93], drug screening [94], reactive oxygen species [ROS] production [95]) applications. Despite the increasing number of those biosensors, their application has been mostly limited to microscopy and not macroscopy.

Bioluminescence imaging (BLI) is an alternative indirect fluorescence imaging technique which can be used for macroscopic *in vivo* imaging of molecular events. This technique is based on an enzyme-catalyzed chemoluminescence reaction, wherein light is emitted after a specific substrate oxidation by the enzyme luciferase. Equal to the fluorescent protein expression, the luciferase reporter gene is spliced constitutively or non-constitutively into a regulatory reporter sequence of a target genome. Activation and transcription of the promoter sequence induces luciferase expression. The substrates for those enzymes are not produced in the animal and must be injected for *in vivo* experiments [96]. The common luciferases for bioluminescence imaging are the *Photinus pyralis* (firefly, Fluc), *Renilla reniformis* (sea pansy, Rluc), *Pyrophorus plagiophalamus* (click beetle, CBR) and the *Gaussia princeps* (marine copepod, Gluc) luciferase. Since most of those molecules emit in the blue (Rluc and Gluc) and green (Fluc) spectral range, the development of red-shifted luciferases from *Pyrophorus plagiophthalamus* (Jamaican click beetle) [97], *Photinus pyralis* (American firefly) [98], *Luciola italica* (Italian firefly) [99] and railroad worm [100], reduces light absorption and scattering and enhance sensitivity [101]. Furthermore, BLI require no excitation light for signal induction, thereby avoiding inherent background noise and increase the signal-to-noise ratio [102]. In the last decades, BLI using different luciferases varieties became a powerful tool in cancer research

for imaging molecular and cellular events such as: tumorigenesis and tumor treatment effects [103-106], hypoxia [107], and apoptosis [108].

Beside the strong and positive aspects of indirect fluorescence reporter probes, using fluorescent proteins and luciferases, the utilization of such genetically modified material is limited to preclinical research and cannot be transferred into a clinical application.

1.3.1 Macroscopic fluorescence *in vivo* imaging

1.3.1.1 Fluorescence reflectance imaging

Since fluorescence reflectance imaging was developed in the nineties of the last century it became the workhorse of optical imaging modalities and it significantly influenced our understanding of tumor biology. It is a very simple, flexible and cost-effective technique which provides high throughput measurements of non-radiated compounds with high sensitivity and specificity [109-111].

Basic principle and application

The FRI imaging systems can be grouped in epi-illumination (reflectance mode; source and detector are reside on the same side of the animal) and trans-illumination geometries (transmission mode; source and detector are on the opposite side of the sample illuminating the tissue from one side and detecting emitted light that has passed through the tissue). Both share the same primary measurement principle: the exogenous fluorochromes inside the animal are exited with monochromatic light (e.g. broad beam or raster-scan illumination) of an external source (e.g. halogen/xenon lamps, diodes or laser) and the emission is captured by a sensitive detector (charged-coupled device (CCD), photomultiplier tube (PMT) or avalanche photodiode (APD)). Different filtering strategies (e.g. interference filters, liquid crystal tunable filter or spectrograph gratings) are used to spectrally separate the fluorescence emission spectrum from the excitation and background light signals [112]. All commercially available systems possess the ability to detect and differentiate multiple fluorochromes. The most versatile system in terms of multi-spectral imaging is the Maestro imaging system (PerkinElmer), which uses a liquid crystal tunable filter for the isolation of specific spectral bandwidths. Spectral processing with unmixing algorithms ensures robust and accurate autofluorescence removal and thereby enhancing image contrast and improving signal quantification [113, 114]. Further improvements in terms of image quality, depth sensitivity and image accuracy has been shown for normalized reflectance and trans-illumination data [115].

The interaction of light with different tissue components and the resultant optical contrast is the basic principle of optical imaging, but this also generates intrinsic limitations. Small molecules (e.g. water, ions, sugar, fatty acids), macromolecules (e.g. hemoglobin, proteins, lipids), and cell components (membrane boundaries, collagen fibers) causes strong light absorption and scattering in the ultraviolet (UV) through the visible (VIS) wavelength range and thereby limiting depth penetration in this spectral range to a few millimeter [111]. Shifting the excitation into the near-infrared (NIR) wavelength range (650-900nm) reduces absorption and scattering of light, minimizes tissue autofluorescence, increases photon penetration up to several centimeter and improve target/background ratios [116, 117]. Those aspects enable the

usage of NIR fluorescence for whole-body *in vivo* imaging of small animals [118-120]. Several biological questions were addressed with FRI including: targeting cell-surface receptors [109, 121], enzyme activity [110, 122], tumor growth and metastases [111] and apoptosis [123].

Limitation

Nevertheless, beside the positive aspects of non-invasive NIR-FRI in whole-body analysis, diffuse propagation of light caused by absorption and scattering events are still the bottleneck of this technology. Especially the restricted light penetration and the nonlinear relationship between signal intensity, lesion depth, and optical properties of the lesion and the surrounding tissue limit quantitative analysis [47, 58, 124].

1.3.1.2 Fluorescence molecular tomography

The development of new imaging hardware [58, 125, 126] and novel reconstruction algorithms [127-129] overcome the limitations of planar fluorescence imaging approaches (such as depth resolution and quantification) and enable the three-dimensional localization and quantification of fluorescence probes in deep animal tissue using optical tomography.

Basic principle

The basic principle of this imaging technique contains two mature aspects: First, the illumination of the tissue sample at different points or projections and light measurements collected at the tissue boundary. Second, a mathematical model which describes the diffusive nature of light propagation in tissue [58]. Instead of broad bean illumination, fluorescence molecular tomography utilize sequential tissue illumination with a focused NIR light beam at multiple positions on the animal surface and the emanating excitation and fluorescent light is captured by an array detector. The intensity measurement on the sample surface for each source-detector pair gives an explanation about the diffuse photon propagation in tissue as a function of the specific scattering and absorption coefficient. In the early days of FMT, optical fibers rings were arranged around a cylindrical cavity and coupled with a matching fluid directly to the vertical animal surface [125]. Nowadays, state-of-the-art equipment uses a liquid free, non-contact, 360° free-space excitation/detection concept for horizontal animal scanning in irregular geometries. Furthermore, white light projection illumination offers a detailed surface capture of the animal, which improves reconstruction performance [130-132].

Reconstruction

The results of the surface intensity and boundary measurements are transferred into a mathematical model to compute the photon propagation for each source-detector pair (so-called forward problem). It allows estimating the surface intensity distribution for each source location yielding the sensitivity matrix (also called weight matrix). There are different functions and simulations available (such as Green's function and Monte Carlo simulation) who solve the diffusion equation and describe the photon propagation in a diffuse medium from the point source to the fluorochrome and from the fluorochrome to the detector [133]. Ntziachristos et al. developed the normalized Born approximation to solve the forward problem leading to very robust, accurate and instrumental independent data sets for the fluorochrome distribution in heterogeneous media [127, 134]. Nevertheless, the computation of the unknown fluorochrome concentration distribution in each voxel results in an ill-posed, ill-conditioned and underdetermined problem (so-called inverse problem) [135]. Since this inverse problem

cannot be solved analytically, different algebraic reconstruction techniques (ART) and simultaneous iterative reconstruction techniques (SIRT) trying to eliminate the problem but the reconstruction results are still more or less error-prone [136].

Further improvements can be achieved by incorporating a priori structural information into the image reconstruction process [137, 138]. For this, optical imaging methods are combined with high resolution anatomical imaging techniques such as CT or MR. These prior anatomical information are utilized to improve the accuracy of the photon propagation model and restrict and reduce the uncertainty of the inverse problem, thereby improving optical imaging performance (such as higher resolution and sensitivity) and quantification accuracy [139]. Beside the improvement of data reconstruction, hybrid systems (like FMT-CT [140, 141] or FMT-MRI [142]) merge molecular/functional and anatomical/morphological information and thus enable a more detailed and comprehensive analysis of biological coherences.

Application

Fluorescence molecular tomography and their multimodality approaches have already been used in different applications to monitor tumor location [143], tumor cell activity [144], receptor expression [145] and antitumor treatment effects [146].

1.3.2 Microscopic fluorescence *in vivo* imaging

Macroscopic fluorescence imaging modalities possess the ability for noninvasive monitoring of biological and pharmacological aspects in living animals over time. However, low spatial resolution is the drawback of this technology allowing no *in vivo* visualization of cellular events. The access to cellular resolution is a crucial point for studying basic mechanisms of tumor development, proliferation and metastasis, and it also provides detailed information about drug delivery and response to therapy. Several *in vitro* and *ex vivo* imaging methods have been used to monitor such events, but most of the results are static and thus does not necessarily reflect the physiological *in* vivo situation of dynamic cancer processes [147].

1.3.2.1 Intravital microscopy

Intravital microscopy (IVM) in living animals can overcome these limitations and has provided cellular and/or molecular insights into the complex interaction between tumorigenesis, angiogenesis, tumor microenvironment, and drug treatment response.

Basic principle

Microscopic imaging modalities were initially used for *in vitro* and *ex vivo* imaging but the development of innovative hardware and molecular reporter systems and the availability of suitable animal models pioneered the way for *in vivo* application. To perform IVM four different components are required: (i) an animal model which provide sufficient access for visualization, (ii) a molecular probe for specific target detection and contrast enhancement, (iii) a microscopic imaging modality, and (iv) an appropriate software (algorithms and/or mathematical models) for data extraction and reconstruction [148, 149].

Animal models for IVM

As already discussed in the previous section, skin and tissue of the animal causes strong absorption and scattering of fluorescence light and reduces penetration depth even in the NIR wavelength range. To overcome those limitations and provide a more or less unrestricted optical access to the implanted tumor area, various intravital models such as chronic-transparent windows (e.g. cranial window [150], dorsal skin [151] and ear chamber [152]), *in situ* preparations (e.g. tail lymphatics [153]), and acute tissue preparations (e.g. liver [154], pancreas [155] and mammary gland [156]) are generated. These transparent chamber preparations enable repetitive and high-resolution *in vivo* imaging of dynamic possesses in the living animal up to several weeks.

Fluorescent probes

The development of new fluorescent reporter probes (exogenous fluorochromes and fluorescent proteins) and fluorescent transgenic reporter mice further enhanced the power of IVM by improving signal-to-noise and optical contrast, leading to high imaging specificity and sensitivity. Since microscopic and macroscopic fluorescence imaging modalities utilize the same basic measurement principle, direct and indirect reporter probes, as already described for macroscopic fluorescence imaging, can be transferred one-to-one into microscopic *in vivo* application.

Microscopic imaging modalities for IVM

Nowadays, different microscopic fluorescence imaging modalities are utilized for intravital applications including: confocal laser-scanning microscopy (CLSM) and multi-photon laser-scanning microscopy (MPLSM) [157]. Both imaging techniques using focused laser beams scanned in a raster pattern to generate high spatial resolution and contrast rich images. Unlike CLMS, multi-photon microscopes do not contain a spatial pinhole aperture in front of the detector to eliminate out-of-focus emission light. In contrast to classical fluorescence and confocal microscopy where the fluorochrome is excited by a single photon, MPLSM uses two pulsed low energy photons (or even more) from the IR or NIR wavelength range for specific fluorochrome excitation. This non-linear two-photon excitation event occurs only at the focus point where the photon density is high enough for a simultaneous absorption, whereby reducing the out-of-focus emission to a minimum. Furthermore, the illumination with NIR light reduces absorption and scattering artifacts and increase depth penetration up to 1 mm [158]. Both modalities are eminently suitable for three-dimensional real-time observation of multiple biological *in vivo* events down to cellular resolution (until 500 nm). The drawback of those imaging technics is the slight penetration depth of below one millimeter and a small field of view which prevent entire tumor scanning [151, 159]. Further limitations of laser-scanning microscopy are the marked differences between the lateral and axial resolution, long exposure and measurement times, and photo-bleaching of the fluorochromes outside the focus planes [160].

Other IVM techniques, such as optical coherence tomography (OCT) and optical frequency domain imaging (OFDI), can measure a large FOV with penetration depths beyond 1 mm and a spatial resolution of about 10-50 µm, but their basic principle (optical interferometry) of measuring the various optical scattering properties in tissue can provide “only” morphological and physiological tissue information [161-163]. Direct visualization of a molecular reporter

probe and its penetration, accumulation and interaction with the target structure is not possible using classical fluorochromes [164].

Application of IVM

IVM opened a new age of real-time tumor analytics in living animals in four dimensions (x, y, z and time) down to cellular resolution and have provided unprecedented insight into tumor microcirculation and microenvironment. In the last decades, these microscopic imaging modalities were used for different applications ranging from molecular imaging (such as micro-pharmacokinetics [165], microenvironment [166], enzyme activity [167] and gene expression [168]), cellular imaging (like tracking of cancer [169] and immune effector cells [170]), anatomical imaging (e.g. tumor size [171], vascular [150] and lymphatic architecture [172]), functional imaging (such as blood-flow [151] and lymph-flow rate [173], vascular permeability [174], interstitial diffusion and pressure [175]) and imaging of treatment response (from chemo-therapeutics, small molecules and/or biologics [171]) [159].

Limitation of IVM

Beside the positive aspects and great potential of this method in cancer research, the slight penetration depth and the small FOV allows only a detailed tumor observation at an early time point of tumor development [147, 157, 176]. When the tumor becomes solid and reaches a critical size, strong light absorption and scattering prevent entire acquisition of the heterogeneous tumor event.

1.3.3 Mesoscopic fluorescence *ex vivo* imaging

All the different macroscopic and microscopic fluorescence imaging modalities which were introduced in the previous chapter possess corresponding strengths but they also have clear limitations. Macroscopic *in vivo* imaging methods are able to non-invasively detect dynamic biological processes in living species in a large field of view over time, but they suffer from a low spatial resolution and cannot resolve individual cells. On the other hand, microscopic *in vivo* imaging techniques provide excellent temporal and spatial resolution down to cellular events, but they have penetration depths of less than 1 mm and thus are incapable to image large specimens. Only standard *ex vivo* histological sectioning provide detailed microscopic information from macroscopic specimens. Nevertheless, single tissue slices represent only a very small fraction of the examined tissue sample and therefore do not reflect the inhomogeneous tissue composition. The 3D reconstruction of serial tissue slices is also not an appropriate alternative, because it is a very laborious and time-consuming process and the mechanical distortion of the tissue slices makes it hard to obtain.

1.3.3.1 Light-sheet based fluorescence microscopy

Those existing limitation for the visualization of cellular structures in large tissue specimens, inspired the development of light-sheet based fluorescence microscopy (LSFM).

Basic principle

The basic principle of this technology was already described over a century ago by Siedentopf and Zsigmondy [177], where they illuminated the sample from the side with a thin sheet of light that overlap with the focal plane of the detection optics. Since that time further technical

developments yield to different versions of light-sheet microscopy, including orthogonal-plane fluorescence optical sectioning (OPFOS) [178], thin-light sheet microscopy (TLSM) [179], selective plane illumination microscopy (SPIM) [160] and ultramicroscopy (UM) [180, 181]. Latter will be explained in more detail because this imaging technique is an essential part of this work.

Ultramicroscopy

Ultramicroscopy, as described by Hans-Ulrich Dodt and colleagues [180], uses focused laser light for a double-side, in-focus plane illumination of the specimen (i.e. optical sectioning) and the fluorescent detection is performed with a highly efficient detector perpendicular to the illumination axis. By moving the tissue sample vertical through the planar laser beam, a *z* stack of serial optical sections is produced. Since only the in-focus plane is illuminated, the photo-bleaching of fluorochromes from outer sample regions are reduced to a minimum and no out-of-focus fluorescent light has to be excluded by a pinhole later on, like in confocal microscopy. Furthermore, this simple and easy to handle optical sectioning setup provides several crucial properties, including high acquisition speed, high signal-to-noise ratio, and a good penetration depth [182, 183].

Tissue clearing

To overcome the problem of strong light absorption and scattering and further increase penetration depth it is necessary to make the tissue samples optical transparent. This can be achieved by a chemical clearing procedure which was also developed nearly a century ago by Werner Spalteholz [184]. During optical clearing, the water in biological samples is removed by tissue dehydration followed by impregnation with an optical clearing agent which has approx. the same refractive index as solid tissue components, like lipids and proteins. The most frequently used dehydration solutions are ethanol or tetrahydrofuran (THF), whereas optical immersion is mainly performed with dibenzyl ether (DBE) or a mixture of benzyl alcohol plus benzyl benzoate (BABB; Murray's clear) [185]. The alignment of the refractive indices of the intra- and extracellular compartments render the tissue sample transparent. The improved optical property of the cleared specimen reduces light scattering to a minimum, therefore providing higher imaging contrast and resolution and enables optical imaging deep within the tissue [186].

Application

In the early days light-sheet microscopy remained largely unnoticed by the general public and had only little impact in the scientific community, because proper three-dimensional reconstruction software was not available and the applicability of optical clearing to relevant biological samples was not realized [178, 179]. After the ground-breaking study by Ernst Stelzer's lab [160], which used LSFM to monitor GFP expressing muscles in transparent fish embryos, optical sectioning of large transparent and/or cleared tissue samples became more and more relevant in different areas of application such as evolutionary biology (embryonic development) [187-191], neuroscience [180, 181, 192, 193] and immunology [194]. The transfer of this promising imaging technique into the field of cancer research and drug development was described only very rarely in single publication until today [186].

Limitation

Light-sheet fluorescence ultramicroscopy in combination with optical tissue clearing open up new unprecedented three-dimensional insights into biology down to cellular resolution, but like other imaging modalities it also possesses crucial limitation. First, the method can only be applied to postmortem end point specimens and therefore measurement of dynamic processes and longitudinal studies are not feasible. Second, the measurement of large tissue samples is still limited to a resolution of ~2 µm with a 4-5 mm and ~5 µm with 15 mm imaging field. Third, appropriate algorithms and software applications for an automatic quantification of large and complex three-dimensional data sets are not available. Current semiautomatic software solutions are user dependent and therefore time consuming and prone to mistakes [180, 181, 186].

1.4 Impact of molecular imaging on cancer research

Preclinical application

Recent advances in molecular and cell biology and the increased knowledge of the human and other mammalian genomes have improved our understanding of the molecular and cellular mechanisms that control biological processes and underlie many diseases, including cancer. However, despite a richness of drug targets arising from our understanding of the human genome and diversity of potential therapeutic modalities (such as small molecules, biologics, vaccines, and siRNA), a key challenge for basic scientists and clinicians is defining which molecules and/or pathways, among many, control disease initiation and progression in intact animals or patients. Ongoing discoveries of potential target molecules in disease also drive pharmaceutical and biotechnology companies to find agents that selectively regulate these signal transduction pathways *in vitro* and *in vivo*. This selection process contains an extremely low probability of success for unprecedented mechanisms and is also highly cost-intensive [195, 196]

Scientists in drug discovery and drug development are trying to increase the probability of success by identifying of the most appropriate targets responsible for primary tumor growth, metastasis and tumor angiogenesis, optimizing their validation, selecting the best molecules and driving them expeditiously toward proof-of-concept in patients. Advances in non-invasive optical imaging are playing an increasingly important role in our efforts to address these challenges and provide exciting opportunities for discovery, validation and development of novel therapeutics. These technologies provide a non-invasive or minimally invasive means of visualizing, characterizing, and quantifying anatomical structures and physiological processes at the cellular and subcellular levels with exquisite spatial, temporal, and biochemical resolution *in situ* and *in vivo* [48, 197].

As the arsenal of detection devices and strategies, injectable active and activatable probes, genetically encoded reporters, and animal models rapidly expands; molecular fluorescence imaging adding a new dimension to our understanding of basic biological and pharmacological mechanisms and is therefore becoming indispensable for drug discovery and development. Those new imaging tools open up the possibility for non-invasive longitudinal monitoring of gene expression, signal transduction, regulatory pathways, biochemical reactions, target expression and facilitate as an integrative tool to discover new drug targets, identify novel

drug candidates and validate their potency, sensitivity, specificity, PK, PD and even toxicity, metabolism and adverse drug–drug interactions in living subjects [39, 41, 44, 51]. Furthermore, the inexpensive, fast, sensitive, non-invasive, and non-radioactive optical imaging techniques allows high throughput testing on a larger number of new cancer drugs and therapies and therefore reduce the time, cost and workload associated with conventional destructive endpoint assays, such as tissue sampling and the analysis of body fluids (e.g. blood and urine) [41, 198].

Non-invasive imaging of the same laboratory animal at multiple time points avoids many of the potential artifacts and pitfalls that can be associated with tissue processing in *ex vivo* and *in vitro* model systems by imaging in a physiologically relevant tissue context. It also results in a decreased consumption of laboratory animals and reduces the statistical variability that is inherent in traditional *ex vivo* methodologies in which data are compared among different groups of animals that must be sacrificed during the course of the protocol in order to obtain the data. In whole-animal imaging technologies, each experimental animal is its own statistical control, improving the statistical quality of the data [199, 200]. According to these arguments, one can assume that optical imaging techniques are speeding up drug development, improve effective decision-making, helping to eliminate failures earlier in the drug development process and contribute to increased efficiency and effectiveness of drug discovery and development programs. The resultant preclinical imaging information regarding pharmacokinetic and pharmacodynamic drug behavior (like effective treatment dosage and application time point) can be used for designing later clinical trials. In this way, optical imaging already possess a substantial impact on basic and translational medical research [48, 198].

The linkage of microscopic and macroscopic fluorescence imaging modalities provides a unique opportunity to monitor multiple biological processes from the whole animal down to the cellular and genetic level. No other imaging modality can offer such a detailed, versatile and comprehensive insight into tumor biology. This huge and decisive advantage of fluorescence imaging makes it a powerful tool for cancer research and the drug discovery and development process.

Clinical application

Recent advances in the development of new optical instrumentation and nontoxic fluorescent probes and nanoparticles pave the way to transfer optical fluorescence imaging approaches into clinical practice. These methods have the potential to visualize endogenous and exogenous tissue contrast and therefore facilitate human cancer diagnostic and surgery by providing specific and sensitive information of normal and disease processes. Today, the main areas of optical imaging in clinical application comprise non-invasive breast imaging by diffuse optical spectroscopy [142, 201-203] and endoscopic [204-206], laparoscopic [207, 208], and intraoperative surgery applications [209-212] for the localization and resection of malignant tumors and metastasis. Especially real-time intraoperative imaging approaches, which can guide the surgeon during primary tumor resection and give some indications of the presence of lymph metastasis, will improve surgical decision making, patient care and possible outcome [211].

Despite many recent advances in the field, there are still relatively few molecular imaging agents in the clinic. This can be attributed to regulatory hurdles that preclude rapid translation of molecular imaging technologies from the laboratory to the clinic, the economics of development costs (100 to 200 million USD) and eventual sales, and finally the high attrition rates for new molecular imaging agents [213, 214].

2 Aim of this work

The entry of different imaging modalities into the preclinical drug development initially opened the opportunity to non-invasive monitor pharmacokinetic and pharmacodynamic processes of therapeutic agent in the living experimental animal. Such *in vivo* information is of particular importance to study and characterize the kinetic behavior, therapeutic efficacy, and possible side effects of new drugs more precisely. Furthermore, those insights help to understand the biological coherences of a disease, design appropriate drug formats, and select potential candidates in a more effective way.

As already shown on a variety of different examples in the prior introduction, fluorescent labeled molecules and fluorescent proteins can be used to non-invasively monitor molecular mechanisms and interactions between therapeutic agents and their target structures over the course of time. Especially fluorescent labeled antibodies and their different formats are eminently suitable as molecular probes, because they possess a high affinity and specificity to the relevant target antigen. The utilization of labeled antibody formats to characterize their PK and PD behavior and/or to determine biological tissue properties (such as the presence and expression level of tumor associated cell surface antigens), was already described and discussed in published literature. The overall consensus of those publications is clear: molecular imaging increases our understanding of tumor biology and drug behavior in a fundamental way and therefore should improve and speed up the drug discovery and development process. Despite the demonstration of the advantages of *in* vivo and *ex vivo* imaging, classical analytical methods, such as tumor volume measurement via caliper, blood taking and analysis to determine serum kinetics, and conventional immunohistochemistry, are still the gold standards of monoclonal antibody development in preclinical animal models.

The exact quantification of relevant parameters and other issues of antibody development (like receptor and epitope evaluation, selection of the most suitable antibody candidate, and/or the determination of the optimal treatment dosage and application cycle) by fluorescence imaging methods and the subsequent verification of these results in preclinical efficacy studies were only insufficiently posed until today. Furthermore, the relevance of such preclinical fluorescence imaging data for the prediction of therapeutic effects in clinical studies has not been addressed in the past and is therefore still unclear.

The present thesis picks up the addressed problems and investigated the possibilities and potential of *in vivo* and *ex vivo* epi-fluorescence imaging methods in the preclinical discovery and development process of therapeutic monoclonal antibodies and fragments thereof. The different topics of this work can be basically divided in three main sections.

First, the combination of *in vivo* and *ex vivo* fluorescence imaging was used to determine and analyze preclinical relevant parameters and issues in a subcutaneous NSCLC xenograft model, including: (i) the determination of the expression level of different tumor cell receptors, (ii) epitope mapping and evaluation of binding specificity of different mabs, (iii) the selection of the most suitable xenograft model for a preclinical efficacy study, (iv) identification of the optimal treatment dosage, and (v) the selection of the best application time point. Thereafter, the imaging results obtained were validated in preclinical efficacy studies. The two therapeutic

antibodies Trastuzumab (Herceptin) and Pertuzumab (Perjeta) were used in the majority of the experiments, because both are already approved as mono- and/or combination therapy with chemotherapeutics in clinical cancer therapy (such as CLEOPATRA study). Therefore both antibodies are perfectly suited for the evaluation and validation of fluorescence imaging in preclinical antibody development.

The second part of the work considers the question if pharmacokinetic parameters of fluorescent labeled molecules can be detected by non-invasive NIR planar-reflectance imaging through the eye of experimental animals. The proof-of-concept and the utility of this “eye-imaging” method were demonstrated by evaluating the pharmacokinetic behavior of three different fluorescent labeled compounds (Indocyanine green, OsteoSense-750, and Trastuzumab-Alexa750). The “eye imaging” method was further combined with whole-body fluorescence imaging for the simultaneous determination of compound pharmacokinetics, biodistribution, and accumulation in the target tissue over time.

Last but not least, to overcome the existing limitations of conventional single tissue slice analysis, multispectral fluorescence ultramicroscopy was for the first time transferred into the field of tumor biology. This technology allows the three-dimensional analysis of whole tumor specimen at cellular resolution. In order to analyze the received three-dimensional data sets, a novel set of algorithms for the automatic segmentation and quantification of multiple tumor parameters were developed. The utility of this new imaging method was evaluated in a preclinical efficacy study to determine the therapeutic treatment effect of Bevacizumab and to investigate the influence of anti-angiogenic pre-treatment on subsequent therapeutic antibody penetration.

3 Materials and Methods

3.1 Materials

3.1.1 Equipment

Table 2: Equipment overview

Equipment	Manufacturer
Biacore, surface plasmon resonance analysis	GE Healthcare, Little Chalfont, UK
Caliper, Digimatic	Mitutoyo Messgeräte GmbH, Neuss
Centrifuge, Biofuge 15	Heraeus Instruments, Hanau
Compartment dryer	Heraeus Instruments, Hanau
Cryostat, Microm HM 560	Thermo Fisher Scientific, Fremont, USA
Fluorescence microscope, DM4000B	Leica Microsystems, Wetzlar
Pipette (10-100 µl, 50-200 µl, 100-1000 µl)	Eppendorf, Hamburg
Illumination lamp, PhotoFluor II NIR	89 North, Burlington, USA
Illumination module, Spectra	Lumencor, Beaverton, USA
Incubator, CO2-Auto Zero	Heraeus Instruments, Hanau
In vivo Imaging System, Maestro®	PerkinElmer, Rodgau
Multispectral imaging Camera, Nuance®	PerkinElmer, Rodgau
Weighing scale, BL 150 S	Sartorius, Göttingen
Slide scanner, Pannoramic 250	3D Histech, Budapest, Hungary
Stephens Anesthetic machine	Eickemeyer Medizintechnik, Tuttlingen
Surgical instruments	B. Braun Melsungen, Melsungen
Tissue Microtome, SM2000R	Leica Instruments, Nussloch
Tissue-Tek	Sakura Finetek, Heppenheim
Tissue-Tek VIP	Sakura Finetek, Heppenheim
Transponder injector	Euro I.D. Identifikationssysteme, Weilerswist
Ultramicroscope	LaVision BioTec, Bielefeld
Vi-CELL cell viability analyzer	Beckman Coulter, Krefeld
Water bath	Medite, Burgdorf

3.1.2 Reagents

Table 3: Reagents overview

Reagents	Manufacturer
Antibody Diluent	Ventana Medical Systems, Tucson, USA
Benzyl alcohol	Sigma Aldrich, Taufkirchen
Bezyl benzoate	Sigma Aldrich, Taufkirchen
Cell Conditioner 1	Ventana Medical Systems, Tucson, USA
Citric acid	Merck, Darmstadt
Citrat buffer	Vector Laboratories, Peterborough, UK
Diaminobenzidine	Dako, Hamburg
Dulbecco´s modified eagle medium	PAN Biotech, Aidenbach
Ethanol	Roche Diagnostics, Mannheim
Ethylenediaminetetraacetic acid	PAN Biotech, Aidenbach
Eosin	Merck, Darmstadt
Fast enzyme	Zytomed Systems, Berlin
Fetal calf serum	PAN Biotech, Aidenbach
Fluoro-Gel II with DAPI	Science Services, Munich
Formaldehyd	VWR International, Ismaning
Hematoxylin	Merck, Darmstadt
Hydrogen peroxide (3%)	Merck, Darmstadt
Inhibitor CM	Ventana Medical Systems, Tucson, USA
Isofluran	Delta Select, Pfullingen
Isopentane	VWR International, Ismaning
Lectin	Sigma Aldrich, Taufkirchen
L-Glutamin (200 mM)	PAN Biotech, Aidenbach
Paraffin	Thermo Scientific, Dreieich
Permanent red	Zytomed Systems, Berlin
Phosphate buffert saline	PAN Biotech GmbH, Aidenbach
Rodent decloaker	Biocare Medical, Concord, USA
Rodent protein block M	Biocare Medical, Concord, USA
Protein block solution	Dako, Hamburg
RPMI-1640 medium	PAN Biotech GmbH, Aidenbach
Target retrieval solution	Dako, Hamburg
Tris-buffered saline tween-20	Carl Roth, Karlsruhe
Trypsin / EDTA	PAN Biotech, Aidenbach
Xylene	Merck, Darmstadt

3.1.3 Consumable material

Table 4: Consumable material overview

Consumable material	Manufacturer
Catheter (26G) / i.v. application	Terumo, Leuven, Belgium
Cell culture bottles (T75 = 250 ml)	Greiner Bio-One, Frickenhausen
Cover slides (24 x 50 mm)	Menzel-Gläser, Braunschweig
Disposable scalpel	B. Braun, Melsungen
Falcon tubes (15, 50 ml)	Becton Dickinson, Heidelberg
Heidelberger extension	B. Braun, Melsungen
Injection needle (18, 26, 27G)	B. Braun, Melsungen
Microtome Blades	Feather, Osaka, Japan
Pipette (5, 10, 25, 50 ml)	Greiner Bio-One, Frickenhausen
Pipette tip (10, 50, 100, 200, 1000 µl)	Greiner Bio-One, Frickenhausen
Slide (24 x 75 mm)	Menzel-Gläser®, Braunschweig
Syringe (1,0 ml)	B. Braun, Melsungen
Transponder	Euro I.D. Identification systems, Weilerswist

3.1.4 Antibodies and proteins for *in vivo* imaging

Table 5: Imaging molecules

Antibodies	Manufacturer
Anti-HER3-Alexa647	Roche Diagnostics, Penzberg
Anti-HER3-Cy5	Roche Diagnostics, Penzberg
Anti-IGF-1R-Alexa555	Roche Diagnostics, Penzberg
Anti-IGF-1R-Cy5	Roche Diagnostics, Penzberg
Cetuximab-Alexa488 (anti-HER1)	Roche Diagnostics, Penzberg
Cetuximab-Cy5 (anti-HER1)	Roche Diagnostics, Penzberg
Crossmab-Cy5 (anti-HER2)	Roche Diagnostics, Penzberg
Omalizumab-Cy5 (anti-IgE)	Roche Diagnostics, Penzberg
Pertuzumab-Alexa750 (anti-HER2)	Roche Diagnostics, Penzberg
Pertuzumab-Cy5 (anti-HER2)	Roche Diagnostics, Penzberg
Trastuzumab-Alexa647 (anti-HER2)	Roche Diagnostics, Penzberg
Trastuzumab-Alexa750 (anti-HER2)	Roche Diagnostics, Penzberg
Trastuzumab-Cy5 (anti-HER2)	Roche Diagnostics, Penzberg
Lectin-Alexa647	Roche Diagnostics, Penzberg

3.1.5 Primary antibodies for immunohistochemistry

Table 6: Primary antibodies for IHC

Antibodies	Manufacturer
Rat anti-mouse CD34 (clone MEC14.7)	HycultBiotech, Uden, Netherlands
Rabbit anti-human HER1 (clone 5B7)	Ventana Medical Systems, Tucson, USA
Mouse anti-human HER1 (clone 3C6)	Ventana Medical Systems, Tucson, USA
Rabbit anti-human HER2 (clone SP3)	Thermo Fisher Scientific, Fremont, USA
Rat anti-human HER2 (clone ICR55)	Biozol Diagnostica, Eching
Mouse anti-human HER3 (clone H3-IC)	Dako, Hamburg
Mouse anti-human HER2 (clone M-15E4F2)	Roche Diagnostics, Penzberg
Rabbit anti-human HER2 (clone 4B5)	Ventana Medical Systems, Tucson, USA
Mouse anti-human IGF1R (clone 24-31)	Merck, Darmstadt

3.1.6 Secondary antibodies for immunohistochemistry

Table 7: Secondary antibodies for IHC

Antibodies	Manufacturer
ImmPRESS-Kit, Goat anti-rat IgG + HRP-polymer	Vector Laboratories, Peterborough, UK
MM-Kit, Goat anti-mouse IgG + HRP-polymer	Biocare Medical, Concord, USA
Envision-Kit, Goat anti-rabbit IgG + HRP-polymer	Dako, Hamburg
ZytoChem-Plus AP Polymer Kit, Goat anti-mouse IgG + HRP-polymer, Goat anti-rabbit IgG + HRP-polymer	Zytomed, Berlin
UltraMap, anti-rabbit IgG + HRP-polymer	Ventana Medical Systems, Tucson, USA
UltraMap, anti-mouse IgG + HRP-polymer	Ventana Medical Systems, Tucson, USA
UltraVision LP-Kit, Goat anti-mouse IgG + HRP-polymer, Goat anti-rabbit IgG + HRP-polymer	Thermo Fisher Scientific, Fremont, USA

3.1.7 Antibodies for therapy

Table 8: Therapeutic antibodies

Antibodies	Manufacturer
Anti-HER3	Roche Diagnostics, Penzberg
Anti-IGF1R	Roche Diagnostics, Penzberg
Cetuximab (anti-HER1)	Merck, Darmstadt
Crossmab-003 (anti-HER2)	Roche Diagnostics, Penzberg
Crossmab-OmniE (anti-HER2)	Roche Diagnostics, Penzberg
Omalizumab (anti-IgE)	Novartis, Nuremberg
Pertuzumab (anti-HER2)	Roche Diagnostics, Penzberg
Trastuzumab (anti-HER2)	Roche Diagnostics, Penzberg

3.1.8 Software

Table 9: Software overview

Software	Provider
Definiens Developer XD	Definiens, Munich
GIMP	Open-souce software
ImageJ	Open-source software
OsiriX	Open-source software

3.1.9 Tumor cell lines

Calu-1

The Calu-1 tumor cells are a human small-cell lung cancer cell line, which was isolated from epidermoid carcinoma of the lung. The culturing of the tumor cells was performed in McCoy`s 5a medium.

Calu-3

The Calu-3 tumor cells are a human small-cell lung epithelial cell line, which was isolated from adenocarinoma of the lung. The culturing of the tumor cells was performed in RPMI-1640 medium.

NCI-H322M

The NCI-H322M tumor cells are a human non-small cell lung epithelial cell line, which was isolated from adenocarinoma of the lung. The culturing of the tumor cells was performed in RPMI-1640 medium.

KPL-4

The KPL-4 tumor cells are a human breast cancer cell line, which was isolated from the malignant pleural effusion of a breast cancer patient with an inflammatory skin metastasis. The cells were kindly provided by Prof. J. Kurebayashi (Kamakura Medical School, Kanagawa, Japan). The culturing of the tumor cells was performed in DMEM medium.

3.1.10 Cell culture medium

DMEM

DMEM	500 ml
FCS	50 ml (10%)
L-Glutamin	5 ml (200 mM)

McCoy`s 5a

McCoy`s 5a	500 ml
FCS	50 ml (10%)
L-Glutamin	5 ml (200 mM)

RPMI-1640

RPMI-1640	500 ml
FCS	50 ml (10%)
L-Glutamin	5 ml (200 mM)

The different reagents were fused under the flow box and stored in the fridge at 4°C.

3.2 Methods

3.2.1 Protein labeling

Several therapeutic antibody formats and proteins were labeled with different cyanin and alexa fluorophores. They were attached via mono-reactive NHS ester to lysine residues of the protein with a labeling ratio of three fluorophores per molecule. All proteins were purified by size-exclusion chromatography, and afterwards surface plasmon resonance (SPR) analysis was performed to verify the biological binding characteristics of the antibody. There were no significant changes in the kinetic constants and the resulting affinity between labeled and non-labeled antibodies.

3.2.2 Experimental animals /animal husbandry

SCID Beige Mouse

In the conducted experiments, female SCID beige mice (Charles River, Sulzfeld) have been used. The mutation of the mouse results in severe combined immunodeficiency affecting both the B and T lymphocytes and also leads to defective natural killer (NK) cells.

SCID Hairless Outbred Mouse

In the conducted experiments, female SCID hairless outbred (SHO) mice (Charles River, Sulzfeld) have been used. The mutation of the mouse results in severe combined immunodeficiency affecting both the B and T lymphocytes.

Upon arrival of the 6-8 weeks old animals in the facility, they were put in quarantine for monitoring for one week and a further week for adaption to the new environment. Afterwards they were transferred in the specific pathogenic free (SPF) area of the animal facility, where they were kept under pathogenic free conditions in ventilated typ III Makrolon cages. As required the animals were given pelleted rodent-single food and water (pH 2,5-3,0). A 12 hour rhythm of light and dark was being predefined. The general health condition was checked on a daily basis and once a week the animals were put in new cages. The mice were handled according to committed guidelines (GV-Solas; Felasa; TierschG) and the animal facility has been accredited by the Association for Assessment and Accreditation of Laboratory Animal Care International (AAALAC). All experimental study protocols were reviewed and approved by the local government (AZ 55.2-1-54-2531.2-26-09 and AZ 55.2-1-54-2531.2-3-08).

3.2.3 Cell culture

The various cell lines were thawed in a water bath with a temperature of 37°C and put in a 50 ml Falcon with an appropriate culture medium. Afterwards the cells were centrifuged for 3 min at 1200 rpm. The supernatant was discarded and the pellet was dissolved in 10 ml of fresh culture medium. The following determination of the number of cells in the suspension was being conducted with the cell counter Vi-CELL. The suspension was adjusted to $1x10^5$ cells / ml, put in a cell culture bottle (T75) and incubated at 37°C, 5% CO_2 and 95% humidity. Depending on the growth rate, the medium was exchanged and/or the tumor cells were split. This process was being conducted until a sufficient amount of cell suspension for the inoculation of every animal existed. On the day of inoculation, all used tumor cell lines amounted to over 85% vitality.

3.2.4 Tumor cell and transponder inoculation

The inoculation of tumor cells into different tissue areas of the mouse, was being conducted under inhalation anesthesia (Isofluoran, 2 Vol%) (Table 10). In addition to this, every animal received a subcutaneous transponder. This mark can be gathered electronically and thus makes it easier to identify and memorize the data of every single animal throughout the experiment. General animal conditions were controlled daily and tumor volume and body weight were monitored once weekly. The tumors grew until they reached their final tumor size for the randomization.

Table 10: Inoculation parameters for the different cell lines

Cell lines	Cell concentration	Inoculation place
Calu-1	$5x10^6$cells / 100 µl PBS	subcutan / right flank
Calu-3	$5x10^6$cells / 100 µl PBS	subcutan / right flank
KPL-4	$3x10^6$cells / 20 µl PBS	Intramammary fat pad

3.2.5 Tumor volume measurement and randomization

Tumor growth and body weight was monitored at least once weekly using caliper measurement. The tumor volume calculation is an approximation of elliptical shaped tumors, which comprises the length (longest dimension) and width (shortest dimension) of the tumor. It was calculated using the subsequent equation:

$$Tumor\ volume\ (mm^3) = 0.5 \times Tumor\ length \times (Tumor\ width^2)$$

Both, the tumor volume and the body weight were automatically gathered and saved with the PHASIS software (Pharmacology Animal Study Information System), specifically developed for Roche. PHASIS recognizes the individual experimental animal through their transponder, assigns the data (tumor volume and body weight) to the respective transponder number and saves it in a data basis. On the basis of this data, PHASIS is capable of automatically conducting a random and regular distribution of the animals within the control and treatment groups so that the differences between the single experimental groups regarding average tumor volume and body weight are insignificantly. Furthermore, the software automatically depicted those animals that showed predefined termination criteria. These guideline criteria were being determined by the respective experimental study protocols. The removal and euthanization of an animal with a xenograft tumor had to be performed at a maximum tumor volume of 1.5 cm^3 or a maximum tumor diameter of 15 mm. A tumor related reduction of the body weight by more than 20% also constituted a termination criterion. The removed animals were euthanized painlessly according to German Animal Protection Act (cervical fracture or CO_2 treatment).

3.2.6 Application of drugs and imaging agents

The treatment of the experimental animals with the various therapeutic antibodies took place on the day of randomization. The intravenous application of the different therapeutic drugs was administrated into the tail vein of the mouse. The fluorescent labeled antibodies, proteins and fluorochromes were applied to the mice in two different ways. In the majority of performed experiments, the fluorescent labeled substance was injected into the tail vein of the mouse. After an appropriate incubation period, the fluorescence intensity was measured via non-invasive imaging methods. In order to detect the pharmacokinetic progress of fluorescent labeled molecules through the eye of the experimental animal, substances were applied via tail vein catheter with a connected Heidelberger extension. Afterwards the signal intensity was being measured using non-invasive fluorescence imaging.

3.2.7 *In vivo* fluorescence imaging

All *in vivo* fluorescence imaging experiments were performed with the 2D planar-reflectance imaging system (Maestro®). The system is based on three main components: (i) illumination module, (ii) imaging chamber, and (iii) workstation computer with the acquisition and analyzing software. The overall performance of the system allows a very fast (5 to 10 seconds per multispectral image cube) and high-throughput measurement.

Acquisition of Maestro data sets

The illumination module used a 300 watt xenon lamp for generating white light. Thereafter, an excitation filter created monochromatic light of a specific range (Table 11), which was transferred by optical fibers into the imaging chamber. The narcotized experimental animals were pleased on a heating plate (37°C) inside the imaging chamber and received further inhalation anesthesia (Isofluoran, 2 Vol%).

Table 11: Filter settings of the Maestro imaging system

Filter set	Fluorophore	Excitation filter	Emmision filter	Spectal range
Blue	Alexa488	445-490 nm	515 nm / longpass	500-720 nm
Green	Alexa555	503-555 nm	580 nm / longpass	550-800 nm
Red	Alexa647, Cy5	615-665 nm	700 nm / longpass	680-950 nm
Deepred	Alexa750	671-705 nm	750 nm / longpass	730-950 nm
ICG	ICG	710-760 nm	800 nm / longpass	780-950 nm

For standard imaging experiments the flexible fiber-optic illuminator arms and the specimen stage high were set on position two. The monochromatic light excited the fluorescent labeled molecules inside animal and the emitted light traverse through an emission filter to the highly sensitive CCD camera with a resolution of 1392 x 1040 pixels (pixel size of 6.45). The air cooled camera system of Maestro is based on a solid-state liquid crystal tunable filter (LCTF), which allows multispectral fluorescence imaging from the visible to near-infrared (NIR) range (450-950 nm). The LCTF enables a selective 12-bit image (4096-level) measurement of fluorescent emissions light at multiple points in the spectral emission range with a wavelength step size of 10 nm. The series of single 12-bit images of the different specific wavelengths were saved as an “image cube” (Fig. 1b).

Thereafter, autofluorescence and fluorochromes signals with overlapping emission spectra were spectrally unmixed from the image cube using sophisticated spectral unmixing algorithms (Fig. 1c,d). The autofluorescence signals emitted from the animal’s tissue and skin were removed from the image cube. The resultant improvement in signal-to-noise increased fluorescence sensitivity up to several hundred-fold. Unmixed grayscale “component images” of fluorescent labeled molecules were used to quantify the fluorescence signal intensity in the region of interest (ROI) (Fig. 1e). The gray scale values were converted into pseudo-color and overlaid with the monochrome image of the animal (Fig. 1g).

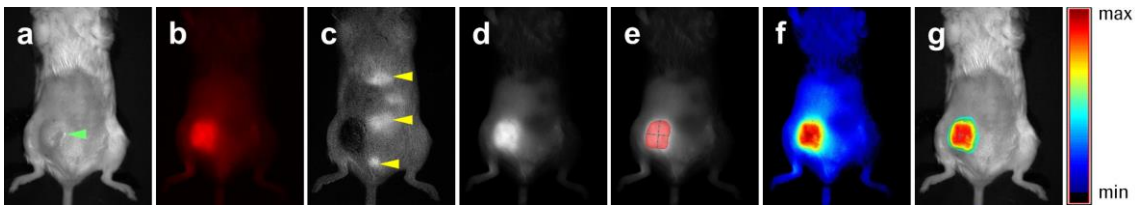

Figure 1: *In vivo* multispectral fluorescence imaging with Maestro. (a) Monochrome image of the animal with an orthotopicly implanted KPL-4 tumor (green arrowhead). (b) Image cube acquired with the red filter set. (c) Unmixed autofluorescence grayscale component image with strong food signals (yellow arrowhead). (d) Unmixed grayscale component image of Cy5 labeled Trastuzumab. (e) Unmixed grayscale component image with measurement region (red area). (f) Unmixed grayscale component image converted into pseudo-color (jet). (g) Monochrome image with pseudo-color image overlay.

Quantification of Maestro data sets:

Maestro quantification software was used to determine the fluorescence signal intensity inside the manually drawn measurement regions of the spectrally unmixed component images. The signal intensities were specified as scaled counts per second, which indicated count levels from the CCD camera after scaling for the effects of exposure time, binning (2x2), camera gain (3) and bit-depth (12-bit). Thus, the measurement pixel unit is essentially independent of these settings.

The calculation of the measurement value was carried out using the following equation:

$$\frac{scaled\ counts}{second} = \frac{counts}{full\ scale} \times \frac{1}{exp^{(s)}} \times \frac{1}{bin^2} \times \frac{1}{gain}$$

full scale = 4096 for 12-bit

s = Exposure time (sec)

bin = Binning

Furthermore, the software contains a tool to compare unmixed grayscale images with each other. It enables the possibility to visualize signal intensity differences between the component images. Images compared with this tool do not need to have the same scaling or image display parameter. Compare images were displayed on the same scale, accounting for differences in intensity due to bit-depth, exposure time and binning. The created compare images were converted into pseudo color (jet) (Fig. 1f) and merged with the corresponding monochrome image of the animals (Fig. 1g).The software ImageJ and GIMP were also used for image fusion and preparation of the individual images.

3.2.8 Tissue explantation, fixation, clearing and embedding

Upon completion of the *in vivo* imaging experiments all animals were sacrificed, the tissue of interest was explanted and transferred into an embedding cassette. The tumor tissue was fixed in 10% buffered formalin for about 12 hours at 4 °C in the dark and then the specimens were dehydrated in a graded ethanol and xylene series (3 x 70%, 2 x 95%, 2 x 100% ethanol and 2 x 100% xylene for 1.5h each). Afterwards, the tissue samples were incubated (4 x paraffin for 1 h each) and embedded in paraffin. All the incubation steps were carried out using the Tissue Tek® VIP Vacuum Infiltration Processor.

For three-dimensional *ex vivo* fluorescence imaging using ultramicroscopy all specimens were dehydrated in a graded ethanol series (3 x 70%, 2 x 95%, 2 x 100% ethanol for 30 min each, Tissue Tek® VIP). Thereafter, the dehydrated tissue samples were placed in a clearing solution of two parts benzyl benzoate and one part benzyl alcohol and incubated for at least two days at 4 °C in the dark. After performing ultramicroscopy the specimens were shortly incubated in xylene to remove the superficial clearing solution and further they were incubated (4 x paraffin for 1h each, Tissue Tek® VIP) and embedded in paraffin.

To generate cryo slice section the tissue explant was shortly incubated in cooled iso-pentane solution and transferred instantly into liquid nitrogene. The deep frozen tissue material was taken out of the fluid and upon its slicing stored at -80 °C.

3.2.9 Tissue slicing

The paraffin embedded tumors were cooled down to -2 °C with a cooling plate and afterwards sliced with a microtome. The 2.5 µm tissue slices were applied on a slide and fixed on a heating plate at 40 °C for 2-3 minutes. The main fixation followed overnight in the compartment dryer at 37 °C. The slices were kept in the refrigerator at 4 °C until further use. These paraffin tissue slices, fixed in the above mentioned way, were the basis for the following tissue analysis.

The preparation of cryo slices rendered from the deep frozen samples was done with cryostat at -20 °C. The slices of approx. 5 µm in diameter were applied on a slide and stored at – 80 °C until their histological staining.

3.2.10 *Ex vivo* fluorescence imaging

To proof the different tumor parameter as well as the penetration- and absorption performance of fluorescent labeled molecules the tumor tissue was analyzed with 2D and 3D microscopic procedures. For this purpose, classical two-dimensional bright field and fluorescence microscopy, as well as the initial three-dimensional ultramicroscopy were used. Both procedures offer the possibility for a multispectral assessment of cellular structures.

3.2.10.1 2D histology using multispectral fluorescence microscopy

The paraffin and/or cryo slices, rendered from fluorescent labeled tumors, were covered with a DAPI containing medium and locked with a cover slide. Before that, the tissue slices were de-paraffinized in a declining row of xylene and ethanol (3 x 100% xylene, 2 x 100%, 2 x 95%, 2 x 80%, 2 x 70% ethanol and for 2 min each) and the cryo slices were fixed in cooled acetone (0 °C). Afterwards, the fluorescence signal intensities in the tissue slices were detected via classic fluorescence microscope with a built-in multispectral imaging camera (Nuance®) and/or with a fluorescence-slide scanner.

Acquisition and quantification of Nuance data sets

The Nuance camera system was installed via c-mount on a conventional fluorescence microscope. The illumination module used a 200 watt metal halide lamp for generating white light. Several excitation and emission filter were utilized to generate specific excitation light and separate the emitted fluorescent light. The Nuance camera system is based on the same technical principle as already described in chapter 3.2.7. Hence, it was also possible to perform multispectral detection and unmixing of different fluorophores inside a tissue slide. The resultant unmixed grayscale component images of a specific fluorophore were normalized to compare their signal intensities.

High-throughput fluorescence measurements of whole tissue slice sections were carried out via commercial fluorescent slide scanner with a slide capacity up to 250 slides. Independently operating multiple solid state light sources were used in the SPECTRA illumination module for excitation. The system utilizes an air cooled sCMOS pco-edge camera with a resolution of 2560

x 2160 pixels (pixel size of 6.5 µm) for fluorescence detection. Image visualization and analysis were accomplished with the slide scanner software (Pannoramic viewer). The software ImageJ and GIMP were also used for image fusion and preparation of the individual images.

3.2.10.2 3D histology using multispectral fluorescence ultramicroscopy

The cleared tissue samples were scanned with the commercial available light-sheet laser-scanning ultramicroscope. This post-mortem imaging method allows the three-dimensional visualization of multiple tissue parameters on cellular resolution.

Acquisition of ultramicroscopy data sets

The ultramicroscope is based on a macro zoom fluorescence stereomicroscope (MVX10, Olympus) with an integrated double-sided light-sheet illumination. The supercontinuum white-light laser (SuperK Extreme 80 mHz VIS, NKT Photonics) covers the entire wavelength range of 400-2400 nm and enables the excitation of every commonly used fluorophore.The air cooled Imager 3QE camera (LaVisionBiotec) with a resolution of 1376 x 1040 pixels (pixel size of 6.45 µm) was used for fluorescence detection. Variable stereomicroscope magnifications (1.26x-12.6x) leading to final xy-resolution ranging from 5.1 µm down to 0.5 µm. For the majority of the executed imaging experiments the final xy-resolution and step size were set to a value of 5.1 µm. Specimen diameter up to about 6 mm were scanned with this hardware configuration.

The cleared tissue sample was fixed in the sample holder and pleased in the imaging chamber of the UM. Double-side illumination with a thin laser sheet leading to a homogenous excitation of the illumination plane and the emitted fluorescent light was detected by the camera. Further optical sections were generated by stepping the cleared tissue through the thin illumination plane. The different optical properties of vital and necrotic tissue and the strong autofluorescence emission of the erythrocytes were utilized to create a detailed illustration of the tumor morphology (excitation range: 543/22 nm; emission range: 593/40 nm). Lectin-Alexa647 (excitation range: 655/40 nm; emission range: 716/40 nm) and Trastuzumab-Alexa750 (excitation range: 710/40 nm; emission range: 775/46 nm) showed a strong binding affinity to their target structure and provided high signal intensities. Thus, the measurements were performed with short exposure times (100-400 ms per slice) resulting in a total acquisition time of about 30 to 40 minutes per tumor depending on its size. Thereafter, the generated TIFF slices were converted into DICOM files and visualized using the OsiriX software. Furthermore, ImageJ and GIMP were also used for the preparation of the individual images and videos in this manuscript.

Quantification of ultramicroscopy data sets

The quantification of the raw data was performed with a set of custom-developed image analysis algorithms implemented as a “Definiens Cognition Network Technology” ruleset (Definiens). To increase performance the skeletonization and branchpoint detection was written in C++ utilizing the “Insight Segmentation and Registration Toolkit” (ITK) and loaded as a custom plugin. With Definiens requiring a 6 pixel 3D neighborhood an existing ITK implementation [215] was modified so that the skeleton had no more diagonal pixels (26 neighborhood). On one CPU core (Intel Xenon X5670 @ 2,93 GHz) it took between 10 minutes (peak RAM usage 8 GB) and 2 hours (peak RAM usage 20 GB) to quantify a single tumor, depending on the tumor size and desired software settings (half resolution and no penetration

analysis up to full resolution with penetration analysis). Multiple engines can run simultaneously if enough hardware resources and Definiens licenses are available thus enabling the timely and fully automatic quantification of large groups with our software. For the present thesis the software was configured to use the full resolution of the UM datasets. Furthermore, vasculature with a distance to the surface of the tumor smaller than 20 percent of the radius of a fictional sphere with same volume as the tumor was defined as periphery.

3.2.11 *Ex vivo* immunohistochemistry

Besides *in vivo* and *ex vivo* imaging of fluorescent labeled molecules, also conventional immunohistochemistry staining was performed. For this purpose the tissue slices were de-paraffinized in a declining alcoholic row of xylene and ethanol (3 x 100% xylene, 2 x 100%, 2 x 95%, 2 x 80%, 2 x 70% ethanol and for 2 min each). Afterwards, antigen retrieval, blocking of free peroxidases, and a protein block were conducted. Various primary detection antibodies were used for the immunohistochemical detection of different tumor antigens. The primary antibody was captured by a secondary antibody-chromogene detection system. Additionally a staining of the nucleus via hematoxilin was conducted in most of the cases. Then the stained IHC slices were dehydrated in a graded alcoholic row of ethanol and xylene (2 x 70%, 2 x 80%, 2 x 95%, 2 x 100%, ethanol and 3 x 100% xylene for 2 min each), covered with eukitt mounting medium and eventually locked air bubble-free with a cover slip. After curing, the tissue slides were measured in the slide scanner. The protocols of the different IHC stainings are listed in the following section.

HER1 staining

Antigen retrieval:	
- Cell Conditioner 1	45 min, 96 °C
Endogenous peroxidase block:	
- Inhibitor CM	4 min, 37 °C
Protein block:	
- Antibody Diluent (EDTA)	16 min, RT
Primary antibody:	
- Rabbit anti-human HER1 (clone 5B7)	ready to use, 16 min, RT
Secondary antibody:	
- UltraMap, goat anti-rabbit HRP	ready to use, 30 min, RT
Chromogen:	
- DAB	ready to use, 10 min, RT
Counter stain:	
- Hematoxylin	ready to use, 4 min, RT
Wash buffer:	
- TBST	

HER2 staining

Antigen retrieval:	
- Rodent Decloaker	40 min, 96 °C
- Citrat buffer	40 min, 95 °C
- Fast Enzyme	5 min, RT
Endogenous peroxidase block:	
-3% hydrogen peroxide in PBS	5 min, RT
Protein block:	
- Protein block solution	10 min, RT
- Rodent block M solution	10 min, RT
Primary antibody:	
- Rabbit anti-human HER2 (clone SP3)	1:100, 60 min, RT
- Rabbit anti-human HER2 (clone 4B5)	ready to use, 60 min, RT
- Rat anti-human HER2 (clone ICR55)	1:100, 60 min, RT
- Mouse anti-human HER2 (clone M15E4F2)	1:67, 60 min, RT
Secondary antibody:	
- Envision, anti-rabbit HRP	ready to use, 30 min, RT
- ImmPRESS, anti-rat HRP	ready to use, 30 min, RT
- MM, anti-mouse HRP	ready to use, 30 min, RT
Chromogen:	
- DAB	ready to use, 10 min, RT
- Permanent red	ready to use, 10 min, RT
Counter stain:	
- Hematoxylin	ready to use, 4 min, RT
Wash buffer:	
- TBST	

HER3 staining

Antigen retrieval:	
- Target retrieval solution	40 min, 96 °C
Endogenous peroxidase block:	
-Hydrogen peroxide solution	5 min, RT
Protein block:	
- Ultra V	10 min, RT
Primary antibody:	
- Mouse anti-human HER1 (clone DAK-H3-IC)	1:30, 60 min, RT
Secondary antibody:	
- Ultra vision LP, goat anti-mouse HRP	ready to use, 30 min, RT
Chromogen:	
- DAB	ready to use, 10 min, RT
Counter stain:	
- Hematoxylin	ready to use, 4 min, RT
Wash buffer:	
- TBST	

IGF1R staining

Antigen retrieval:	
- EDTA buffer (0.001 M, pH 8)	20 min, 96 °C
Endogenous peroxidase block:	
-3% hydrogen peroxide in PBS	5 min, RT
Protein block:	
- Protein blocking solution	10 min, RT
Primary antibody:	
- Mouse anti-human IGF1R (clone 24-31)	1:100, 60 min, RT
Secondary antibody:	
- Envision, goat anti-mouse HRP	ready to use, 30 min, RT
Chromogen:	
- DAB	ready to use, 10 min, RT
Counter stain:	
- Hematoxylin	ready to use, 4 min, RT
Washbuffer:	
- TBST	

H&E staining

- Hematoxylin/ Mayer	4 min
- Blueing in faucet water	1-10 min
- dH_2O	5 sec
- Eosin solution(1%)	1-3 min

CD34 staining

Antigen retrieval:	
- Rodent Decloaker	20 min, 96 °C
Endogenous peroxidase block:	
-3% hydrogen peroxide in PBS	5 min, RT
Protein block:	
- Protein blocking solution	10 min, RT
Primary antibody:	
- Rat anti-mouse CD34 (clone MEC14.7)	1:50, 60 min
Secondary antibody:	
- ImmPRESS-HRP, anti-rat	ready to use, 30 min, RT
Chromogen:	
- DAB	ready to use, 10 min, RT
Counter stain:	
- Hematoxylin	ready to use, 4 min, RT
Washbuffer:	
- TBST	

4 Experiments and Results

4.1 Tumor cell receptor evaluation

For examining the effectiveness of new antibody formats in preclinical studies, suitable tumor models are required. Therefore, the used xenografts have to overexpress a sufficient number of respective target receptors on the tumor cell surface. To determine the receptor expression in tumor tissue, classical immunohistochemical tissue staining with specific antibody assays still represent the gold standard in both, the preclinical and clinical area.

The creation of a well-established immunohistochemical staining assay for a new target protein is a very time- and labor-consuming process. The main difficulties are the selection of the primary and secondary detection system as well as the ideal adjustment and alignment of the large number of staining parameter. Latter can contain up to 20 individual parameter (such as fixation; dehydration; typ of paraffin embedding; slide storage; deparaffination; antigen retrieval; temperature, concentration and pH of the different solutions; washing steps; incubation times and so on) [216-221]. Especially the tissue fixation and the antigen retrieval of fixed tissue samples is a very critical point and represent the bottle-neck of IHC.

Several publications have revealed that this parameter variability of staining protocols can cause problems of reproducibility and may also lead to different staining results in clinical tissue samples [222, 223]. Kaoru Hashizume and colleagues have shown the differential reactivity of three anti-HER2 antibodies (HercepTest/Dako; mAb CB11/Novocastra Lab. and mAb TAB250/Zymed Lab.), resulting in a high HER2 receptor staining variability in human breast carcinomas. Depending on the staining protocols used, both negative and positive staining results have been obtained from the same tissue sample [224].

In the following sections it was examined, if the results obtained in clinical tissue material regarding staining variability, is also relevant in preclinical xenograft tumor tissue. During this preclinical experiments both the binding affinity of different primary anti-HER2 antibodies and the influence of antigen retrievals on the binding affinity were tested in a NSCLC xenograft (Calu-3). Furthermore, the expression level of four different tumor cell receptors (Her1, Her2, Her3 and IGF1R) was evaluated in the Calu-3 xenograft model via conventional IHC staining protocol in comparison to fluorescence *in vivo* and *ex vivo* imaging. The results obtained from both histological receptor evaluation techniques were compared to preclinical efficacy data.

4.1.1 Problems of receptor evaluation using immunohistochemistry

4.1.1.1 Binding affinity of different anti-HER2 antibodies

To examine the various binding affinity of different HER2 antibodies, serial tissue slices of a Calu-3 tumor xenograft were created. The serial tumor tissue slices were de-paraffinized followed by antigen retrieval (with rodent decloaker and fast enzyme) and endogenous peroxidase and protein block (protein blocking solution). Afterwards the HER2 receptor expression level of the Calu-3 tissue slices was detected with different anti-HER2 primary mabs (4B5/Ventana, M15/Roche, ICR55/Biozol, SP3/Thermo Fisher) and stained via secondary mab and chromogens (DAB). The tissue slices were also counter stained with hematoxylin to visualize the nucleus of the cells (Fig. 2).

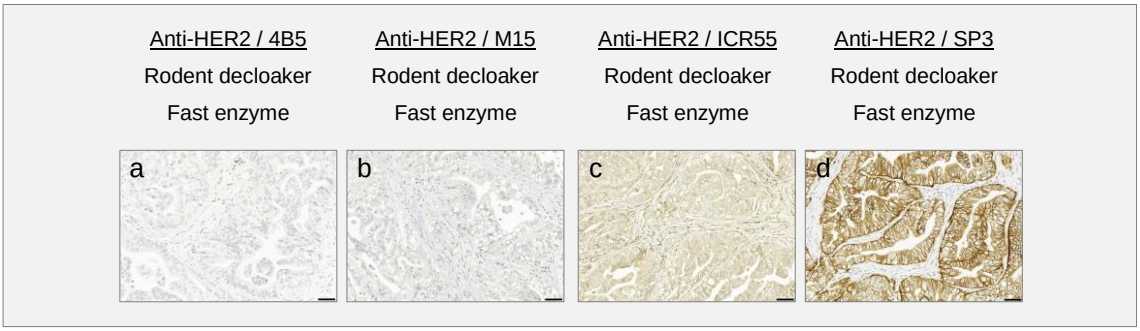

Figure 2: Binding affinity of different anti-HER2 antibodies in Calu-3 xenograft using the same antigen retrieval buffer. (a) No specific HER2 staining with the anti-HER2 mab-4B5. (b) No specific HER2 staining with the anti-HER2 mab-M15. (c) The anti-HER2 mab-ICR55 showed specific tumor cell binding and cross reactivity with the surrounding murine stroma tissue. (d) Optimal HER2 receptor staining with the anti-HER2 mab-SP3. Magnification: x40. Scale bar: 50 µm.

The receptor staining results with the four anti-HER2 antibodies showed different receptor colorings by using identical staining parameter (Fig. 2). The staining with the anti-HER2 antibody 4B5 (Fig. 2a) and anti-HER2 antibody M15 (Fig. 2b) resulted in no specific receptor coloring, whereas the anti-HER2 antibody ICR55 displayed a specific binding to the tumor cells as well as a cross reaction with the murine stroma tissue (Fig. 2c). Only the staining with the anti-HER2 antibody SP3 could achieve a positive staining result and have the ability to display the HER2 receptor status in Calu-3 tissue correctly (Fig. 2d).

Conclusion

The determination of the receptor status of preclinical tissue samples very much depends on the selected detection antibody.

4.1.1.2 Influence of antigen retrieval buffer to antibody binding affinity

In the following section, the influence of different antigen retrieval buffer on the binding capacity of anti-HER2 antibodies is being examined.

Comparison of one anti-HER2 antibody with different antigen retrieval buffer

To determine the possible influence on the binding performance of the anti-HER2 antibody SP3 with different antigen retrieval buffer, serial tissue slices of a Calu-3 tumor xenograft were

created. The serial tumor tissue slices were de-paraffinized and three different solutions were used for antigen retrieval (citrate buffer; rodent decloaker and rodent decloaker plus fast enzyme). Afterwards an endogenous peroxidase and protein block (protein blocking solution), an HER2 receptor staining with anti-HER2 mab-SP3, and counter staining of the nucleus with hematoxylin was performed (Fig. 3).

The antigen retrieval with the various buffer solution lead to a different HER2 staining result within the tissue slices (Fig. 3). The slice treated with a citrate buffer showed no HER2 receptor staining (Fig. 3a), whereas the incubation with rodent decloaker induced a slight HER2 staining (Fig. 3b). Only the combination of rodent decloaker with fast enzyme showed a strong staining result and can thus display the actual HER2 receptor status of the tumor tissue (Fig. 3c).

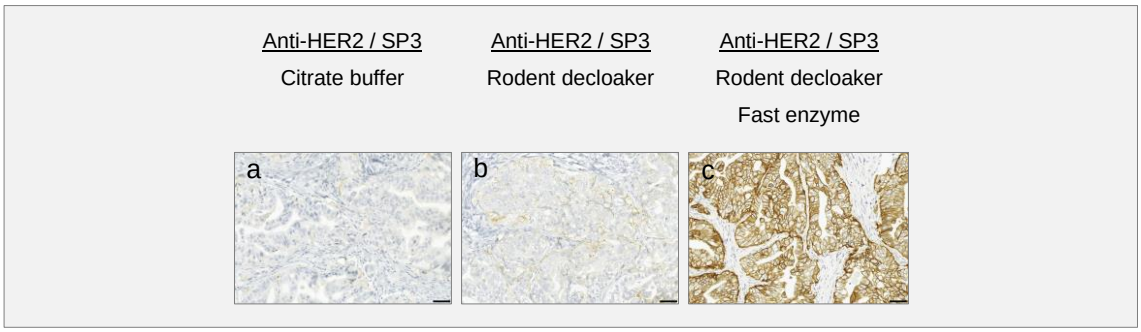

Figure 3: Influence of different antigen retrieval buffer to anti-HER2 mAb-SP3 binding affinity. (a) HER2 receptor staining with mab-SP3 after antigen retrieval with citrate buffer. (b) HER2 receptor staining with mab-SP3 after antigen retrieval with rodent decloaker. (c) HER2 receptor staining with mab-SP3 after antigen retrieval with rodent decloaker plus fast enzyme. Magnification: x40. Scale bar: 50 µm.

Comparison of two anti-HER2 antibodies with different antigen retrieval buffer

For further illustration of the influence of antigen retrieval on the binding affinity of primary detection antibodies, a direct comparison between two different anti-HER2 antibodies (SP3 and 4B5) was being conducted. Therefore serial tissue slices of a Calu-3 xenograft tumor were made and afterwards the de-paraffinization, antigen retrieval with two different solutions (citrate buffer and rodent decloaker plus fast enzyme), endogenous peroxidase and protein block (protein blocking solution), HER2 receptor staining with anti-HER2 mab-SP3 and anti-HER2 mab-4B5, and counter staining of the nucleus was performed. The influence of the antigen retrieval buffer on the determination of the receptor status could also be displayed with this example (Fig. 4).

The anti-HER2 antibody SP3 showed no specific receptor staining in the citrate buffer pre-treated tissue slices (Fig. 4a). As opposed to this the anti-HER2 antibody 4B5 had only a very intense HER2 receptor staining in the same tumor tissue sample (Fig. 4b). The above mentioned process was compared to the prior treatment of the same tissue slices with rodent decloaker in combination of fast enzyme. This antigen retrieval procedure leads to a contrary receptor staining, where the anti HER2 antibody 4B5 reached a negative (Fig. 4c) and the anti HER2 antibody SP3 a positive staining result (Fig. 4d).

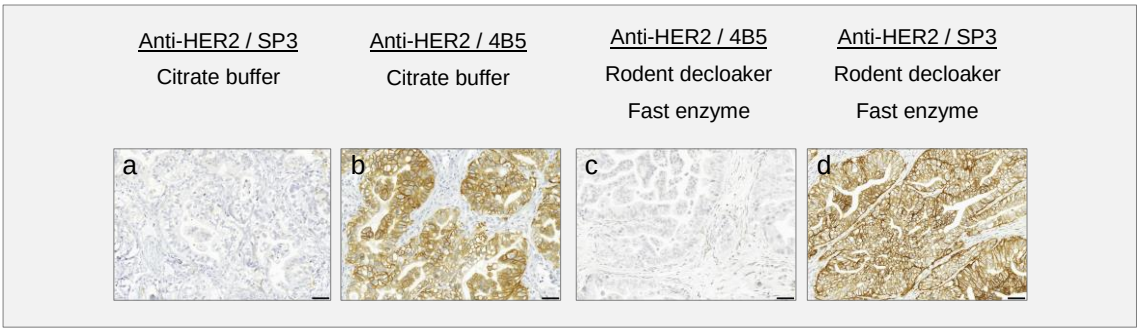

Figure 4: The influence of different antigen retrieval buffer on the binding affinity of two anti-HER2 antibodies. (a) Citrate buffer antigen retrieval followed by anti-HER2/SP3 receptor staining showed no specific HER2 receptor coloring. (b) Citrate buffer antigen retrieval followed by anti-HER2/4B5 receptor staining showed strong HER2 receptor coloring. (c) Antigen retrieval with rodent decloaker plus fast enzyme followed by anti-HER2/4B5 receptor staining showed no specific HER2 receptor coloring. (d) Antigen retrieval with rodent decloaker plus fast enzyme followed by anti-HER2/SP3 receptor staining showed strong HER2 receptor coloring. Magnification: x40. Scale bar: 50 µm.

Conclusion

The evaluation of the receptor status of preclinical tissue samples very much depends on the selected antigen retrieval buffer.

4.1.2 Receptor evaluation using immunohistochemistry

To prioritize a xenograft model for a preclinical efficacy study, the receptor status of a tumor must be evaluated. Immunohistochemical analysis of tumor tissue slices is the standard detection method for the evaluation of tumor cell receptor expression. In the following experiment, the expression level of four different receptors (HER1, HER2, HER3, and IGF1R) in Calu-3 tissue slices was determined via optimized IHC staining protocols. The HER2 staining was conducted with rodent decloaker plus fast enzyme and the anti-HER2 antibody SP3 (Fig. 5). Detailed information regarding the staining protocols are listed in chapter 3.2.11.

The expression pattern for the three human epidermal growth factor receptors showed an inhomogeneous receptor status. The HER1 receptor exhibit only a very light receptor staining (+) (Fig. 5b), whereas HER3 showed an intense (++-+++) (Fig. 5c) and HER2 a very strong (+++) expression level (Fig. 5d). Even the insulin-like growth factor 1 receptor displayed a very intense (+++) overexpression in this xenograft model (Fig. 5a).

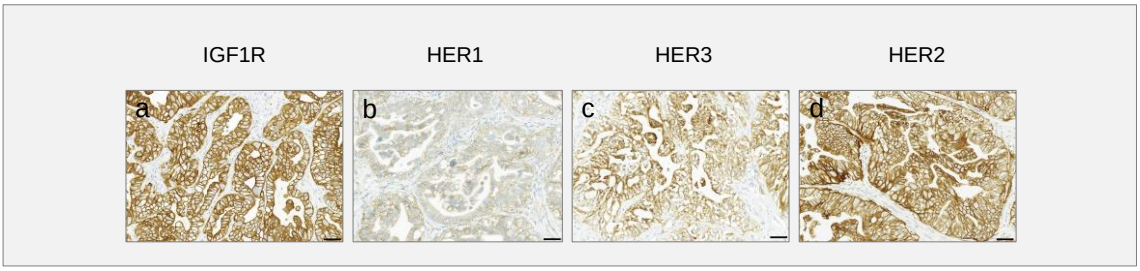

Figure 5: Tumor cell receptor evaluation of Calu-3 xenograft using immunohistochemistry. (a) IGF1R staining with anti-IGF1R antibody (24-30). (b) HER1 staining with anti-HER1 antibody (5B7). (c) HER3 staining with anti-HER3 antibody (H3-IC). (d) HER2 staining with anti-HER2 antibody (SP3). Magnification: x40. Scale bar: 50 µm.

Conclusion

With the IHC staining of the Calu-3 tumor tissue, the tumor cell receptors IGF1R, HER3, and HER2 were prioritized as potential target structures for a preclinical efficacy study due to their high receptor overexpression (++-+++).

4.1.3 Receptor evaluation using fluorescence imaging

In the former section the evaluation of four different tumor cell receptors (HER1, HER2, HER3, and IGF1R) in Calu-3 tumor tissue slices was performed via conventional IHC staining. Those IHC staining results determine only the current receptor status, but since this method using not the therapeutic antibody for target evaluation, it cannot provide any information about the binding properties of the therapeutic agent and deliver no effective response prediction for preclinical efficacy studies.

In the following experiment the expression level of all four tumor receptors (HER1, HER2, HER3, and IGF1R) was determined with fluorescence *in vivo* and *ex vivo* imaging. In a first experiment the receptor evaluation of the different tumor targets was performed using various therapeutic antibodies labeled with the same fluorochrome (Cy5). The IgE specific antibody Omalizumab-Cy5 was used as a negative control. A second experiment determine the expression level of the four tumor cell receptors by using a therapeutic antibody mixture labeled with different fluorochromes (Alexa-488, -555, -647, and -750).

Receptor evaluation with fluorescent labeled antibodies

After intravenous application of the Cy5 labeled therapeutic antibodies (2 mg/kg) in separate Calu-3 bearing mice (n = 5 mice/group) the non-invasive evaluation of the signal intensity via Maestro imaging was performed after 24h. Following this, the binding specificity of the labeled therapeutic antibodies was reviewed by *ex vivo* fluorescence histology (Fig. 6).

Reflecting the *in vivo* imaging results there were no significant differences in signal intensity between anti-IGF1R-Cy5, Cetuximab-Cy5 (anti-HER1), anti-HER3-Cy5 and the negative control Omalizumab-Cy5 (Fig. 6a-d,f). Compared to the negative control, only the Trastuzumab-Cy5 (anti-HER2) signal was significantly increased (Fig. 6e,f). The subsequent *ex vivo* analysis of the different Calu-3 tumors allowed detailed insights in the antibody-receptor-interaction. The *ex vivo* imaging results indicted a strong localization of Omalizumab-Cy5 and anti-IGF1R-Cy5 only in the strom tissue and had no specific antibody binding to the tumor cells. In contrast Cetuximab-Cy5 and anti-HER3-Cy5 were located both in the stroma tissue as well as slightly on the tumor cells, whereas anti-HER3-Cy5 was internalized and Cetuximab-Cy5 was visulaized on the tumor cell surface (Fig. 6c,d). Only Trastuzumab-Cy5 possess a very high binding affinity to the overexpressed HER2 receptors (Fig. 6e).

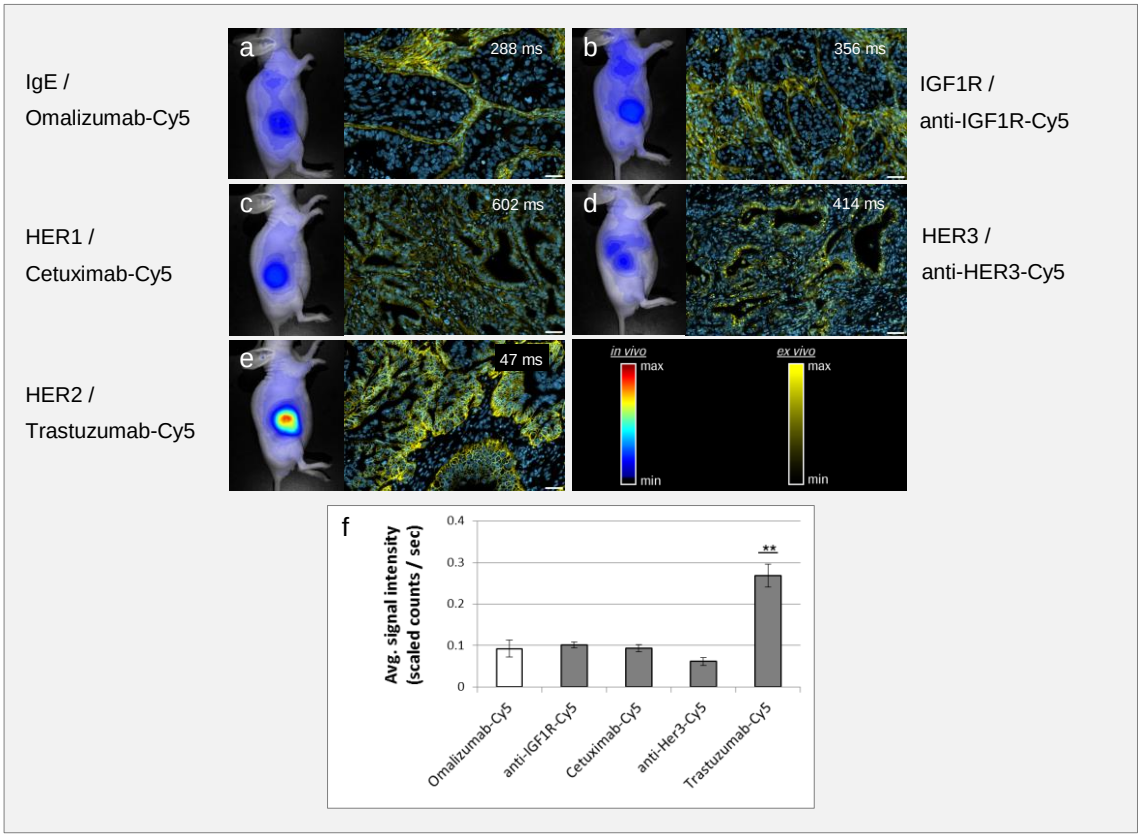

Figure 6: Tumor cell receptor evaluation of Calu-3 xenograft using single fluorescent labeled therapeutic antibodies. (a) *In vivo* and *ex vivo* imaging of IgG specific Omalizumab-Cy5. (b) *In vivo* and *ex vivo* imaging of anti-IGF1R-Cy5 antibody. (c) *In vivo* and *ex vivo* imaging of HER1 specific Cetuximab-Cy5. (d) *In vivo* and *ex vivo* imaging of anti-HER3-Cy5 antibody. (e) *In vivo* and *ex vivo* imaging of HER2 specific Trastuzumab-Cy5. (f) Diagram with the *in vivo* imaging results. Animals per group: n = 5. Values are given as mean ± s.d.. *P<0.05, ** P<0.01, *** P<0.001, *t*-test. *Ex vivo* magnification: x40. Scale bar: 50 µm. The figure in the picture of the tissue slices represent the corresponding exposure time.

Receptor evaluation with a fluorescent labeled antibody mixture

The *in vivo* and *ex vivo* evaluation of the different tumor cell receptors via fluorescent labeled antibodies was displayed in the previous section. In the next step it should be examined, if the expression pattern of the different receptors could also be evaluated with an antibody mixture.

Therefore, the various tumor cell targeting antibodies were labeled with fluorochromes of different wavelengths (Alexa-488, -555, -647, and -750) and intravenously applied as an antibody mixture solution to the experimental animal (2 mg/kg per antibody). After an incubation time of 24h, the Calu-3 tumor was explanted and measured with the Maestro imaging system. Due to the use of fluorochromes of the visible spectral wavelength range (Alexa-488 and Alexa-555), *in vivo* measurements could not be conducted. Within this spectral range the tissue and skin of the animal cause very high absorption and scattering of the excitation and emission light, therefore reducing depth penetration to a minimum. During the following *ex vivo* histology the binding specificity of the different therapeutic antibodies was examined (Fig. 7). The signal intensities of the individual fluorochromes could not be compared to each other, because of their different extinction coefficient and the nonlinear energy content of the illumination light.

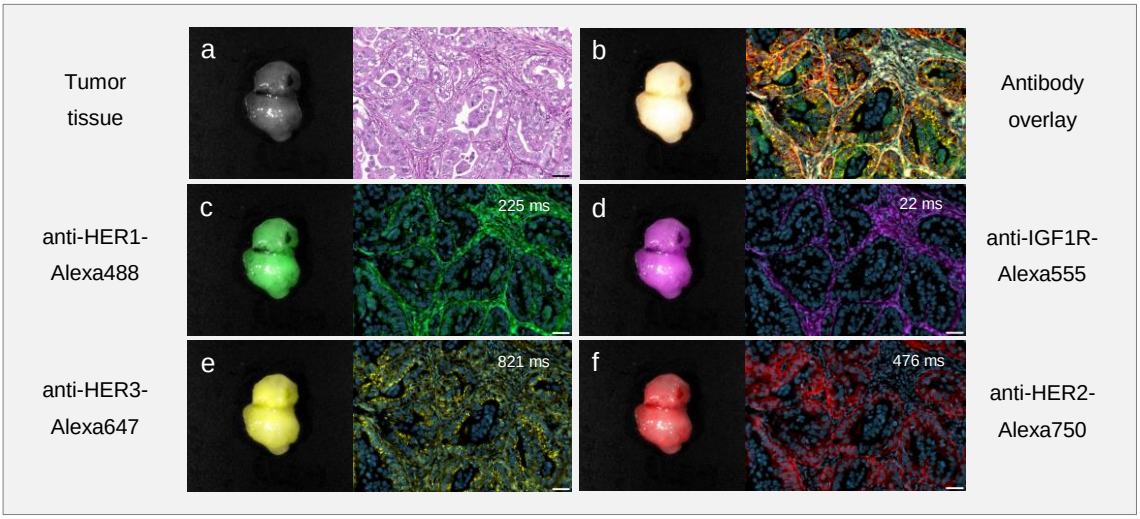

Figure 7: Tumor cell receptor evaluation of Calu-3 xenograft using fluorescent labeled antibody mixture. (a) Monochrome picture of the explanted Calu-3 tumor and a histological tissue slice stained with H&E. (b) *Ex vivo* fluorescence imaging of the fluorescent labeled therapeutic antibodies. The different single mab channels (c-f) were overlaid. (c) *Ex vivo* fluorescence imaging of Cetuxuimab-Alexa488 binding to the HER1 receptor (green). (d) *Ex vivo* fluorescence imaging of anti-IGF1R-Alexa555 mab binding (magenta). (e) *Ex vivo* fluorescence imaging of anti-HER3-Alexa647 mab binding (yellow). (f) *Ex vivo* fluorescence imaging of Trastuzumab-Alexa750 binding to the HER2 receptor (red). Magnification of the tissue slice: x40. Scale bar: 50 µm. The figure in the picture of the tissue slices represent the corresponding exposure time.

Spectral unmixing of the tumor sample measured in Maestro imaging system, clearly indicated the presence of all applied therapeutic antibodies in Calu-3 tumor tissue (Fig. 7a-f). In the following *ex vivo* tumor tissue analysis, the binding affinity and specificity between the labeled therapeutic antibody and its respective receptor was verified. Here the anti-IGF1R-Alexa555 antibody was localized only in the stroma tissue, whereas the remaining three antibodies also connected with the tumor cell. Cetuximab-Alexa488 (anti-HER1) and anti-HER3-Alexa647 showed a rather weak binding behavior, whereas Cetuximab could be found on the surface of the tumor cells and the anti-HER3 mab was located intracellular. In contrast Trastuzumab-Alexa750 showed a very strong extracellular binding to the HER2 receptor.

Conclusion

The receptor evaluation of Calu-3 tumor tissue performed with fluorescence imaging exclusively prioritized the HER2 receptor as the most suitable target structure for a preclinical efficacy study. All further tumor cell receptors, including HER1, HER3, and IGF1R, are not sufficiently overexpressed in Calu-3 tumor tissue and/or the labeled therapeutic antibodies possess only an inadequate binding affinity to the target structure. Those three therapeutic antibodies formats will not generate a sufficient treatment effect in the Calu-3 xenograft model.

4.1.4 Comparison of the histological results with preclinical efficacy data

The results of the receptor evaluation of the Calu-3 tumor tissue, gained from IHC (4.1.2) and fluorescence imaging (4.1.3) were verified in a preclinical efficacy study. Therefore, female SHO mice bearing an s.c. Calu-3 tumor were split into one control and four treatment groups with 8 animals each. After reaching a tumor volume of approx. 100 mm^3, the several therapeutic antibodies were injected once weekly (20 mg/kg, i.v.), whereas the antibody

Omalizumab was used as a negative control. The development of the tumor volume was monitored over the time by caliper measurement. After the termination of the efficacy study, histological examination of the tumor cell proliferation rate was conducted via Ki67 staining (Fig. 8).

The treatment of the Calu-3 tumors with different therapeutic antibody formats lead to different tumor growth kinetics (Fig. 8a). In comparison to the Omalizumab treated control group, Trastuzumab achieved the highest therapeutic efficacy with constant tumor growth inhibition for the whole treatment period. Tumors treated with Cetuximab and anti-HER3 showed a constant tumor growth over the time, but still significantly decreased their tumor volume compared to the control group. Only the anti-IGF1R treatment was incapable to develop any therapeutic treatment effect in this tumor xenograft model. The growth curve of anti-IGF1R treated and the control group was nearly coincident. The subsequent Ki67 staining of tissue slices taken from the control and treatment groups, confirmed the therapeutic treatment results achieved via tumor volume measurement. Thus the proliferation rate between the control (Fig. 8b) and the anti-IGF1R treated group (Fig. 8c) were almost identical. The treatment with Cetuximab and anti-HER3 decreased the proliferation rate by approx. 50% (Fig. 8d,e), whereas Trastuzumab nearly stopped the division rate of the tumor cell completely (Fig. 8f).

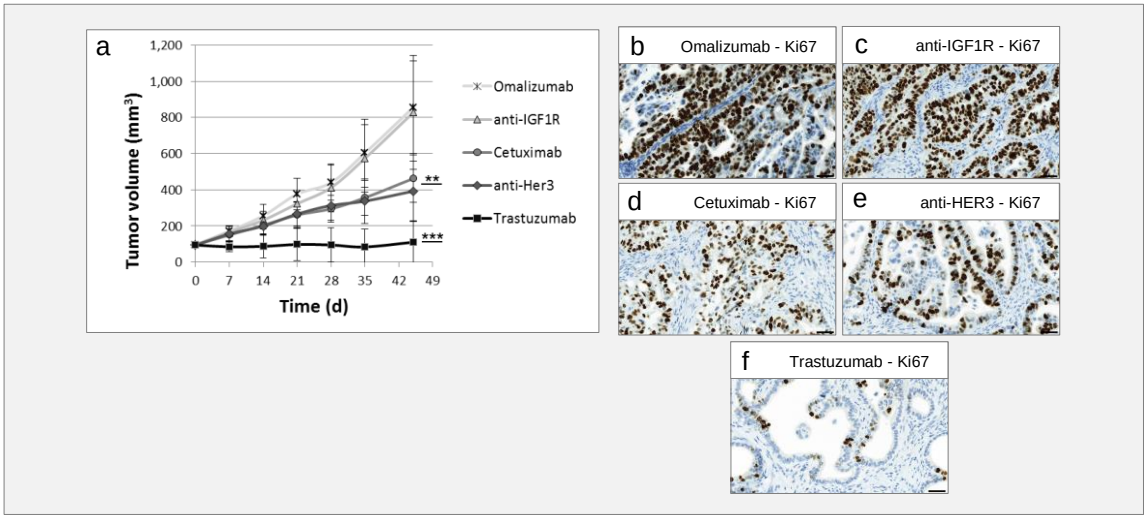

Figure 8: Preclinical efficacy study of different therapeutic antibodies in Calu-3 xenograft. (a) Tumor growth kinetics of the Calu-3 xenograft model treated with anti-IGF1R mab, anti-HER3 mab, Cetuximab (anti-HER1), and Trastuzumab (anti-HER2). The antibody Omalizumab was used as a negative control. Animals per control group: n = 8. Animals per group: n = 8. Values are given as mean ± s.d.. *P<0.05, ** P<0.01, *** P<0.001, t-test. (b-f) Tissue slices of the control and treatment groups were stained for Ki67 to monitor the tumor cell proliferation rate. Magnification: x40. Scale bar: 50 µm.

Conclusion

The conducted preclinical efficacy study in the Calu-3 xenograft model showed a complete tumor growth inhibition under Trastuzumab treatment. Cetuximab and anti-HER3 therapy reduced the tumor cells proliferation rate and therefore slowed down the tumor growth. Only the anti-IGF1R antibody had no influence on the proliferation rate and tumor growth at all.

4.2 Epitope mapping and evaluation of binding specificity

Different *in vitro* methods, such as ELISA, FACS or surface plasmon resonance, are used in antibody discovery and development, in order to evaluate the binding site and the specificity of new antibody formats to the relevant tumor target. Most of the time, the gained *in vitro* results cannot be transferred to preclinical xenograft models, because the complex *in vivo* interaction and correlation between the different molecules and proteins expressed and the therapeutic agents cannot be considered within this rather artificial *in vitro* models. This is the reason why *in vivo* studies are able to render profound insights regarding binding site specificity and affinity of new antibody formats.

In the following sections it was examined if the combination of *in vivo* and *ex vivo* fluorescence imaging is able to help answering such important questions. A proof of concept, regarding binding specificity and epitope mapping, was conducted with the two HER2 specific antibodies Trastuzumab und Pertuzumab in the Calu-3 xenograft model. In a further study, the binding site and specificity of a new bispecific antibody format [225, 226], which is directed against two different epitopes of the HER2 receptor, was evaluated. The results gained from these two imaging studies, were each verified within a preclinical efficacy studies.

4.2.1 Epitope mapping and binding specificity of two anti-HER2 antibodies

The HER2 specific antibodies Trastuzumab und Pertuzumab, which was used in the following experiments, have already proven their specificity for the HER2 receptor in preclinical and clinical studies and made their way into clinical practice. Both antibodies possess a high binding affinity for two different epitopes of the extracellular HER2 domain [227]. Because of the comprehensive knowledge of the binding characteristics and the existing clinical relevance, both antibodies seemed to be the most suitable candidates for a preclinical proof of concept study to determine the binding sites and receptor affinity via *in vivo* und *ex vivo* fluorescence imaging.

Binding specificity of two fluorescent labeled anti-HER2 antibodies

To determine the binding specificity of Trastuzumab-Cy5 and Pertuzumab-Cy5, female SHO mice bearing an s.c. Calu-3 tumor (n = 3 mice/group, TV ± 150 mm^3) were split in two experimental groups. One group was injected with Trastuzumab-Cy5 (2 mg/kg, i.v.) and the other received Pertuzumab-Cy5 (2 mg/kg, i.v.). After 24h of incubation, the fluorescence signal intensity of both labeled antibodies was measured via FRI. Afterwards, the binding specificity of the fluorescent labeled antibodies to the relevant tumor target was determined by *ex vivo* fluorescence histology (Fig. 9).

Both fluorescent labeled antibodies showed rather equal signals intensities in the tumor area during *in vivo* imaging. Even the following *ex vivo* analysis demonstrated identical binding pattern and signal intensities (Fig. 9a-c).

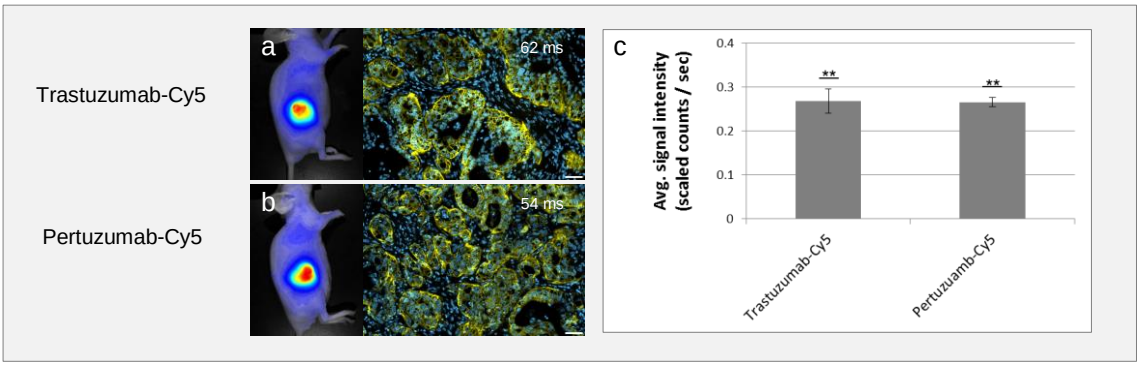

Figure 9: Binding specificity of two fluorescent labeled anti-HER2 antibodies in Calu-3 xenografts. (a) *In vivo* and *ex vivo* fluorescence imaging of the binding specificity of Trastuzumab-Cy5 (anti-HER2). (b) *In vivo* and *ex vivo* fluorescence imaging of the binding specificity of Pertuzumab-Cy5 (anti-HER2). (c) Diagram with the *in vivo* imaging results. Both plots were compared to the *in vivo* signal intensity value of the control antibody Omalizumab-Cy5 (Fig. 6; 0.1 scaled counts/sec). Animals per group: n = 3. Values are given as mean ± s.d.. *P<0.05, ** P<0.01, *** P<0.001, *t*-test. *Ex vivo* magnification: x40. Scale bar: 50 µm. The figure in the picture of the tissue slices represent the corresponding exposure time.

Conclusion

The results gained from this experiment showed the same binding specificities and receptor affinities for Trastuzumab-Cy5 and Pertuzumab-Cy5 both with *in vivo* imaging and *ex vivo* analysis. This begs the question if both therapeutic antibodies bind to the same epitope of the HER2 receptor or if they use different binding sites.

Epitope evaluation of two fluorescent labeled anti-HER2 antibodies

After the same binding specificity and receptor affinity for Trastuzumab-Cy5 and Pertuzumab-Cy5 could be proved via fluorescence imaging in the prior section, the following experiment was used for epitope evaluation of both antibody formats. Therefore, eight experimental groups with female SHO mice bearing s.c. Calu-3 tumors (n = 3 mice/group, TV ± 150mm^3) were first treated with Trastuzumab (10 mg/kg, i.v.), Pertuzumab (10 mg/kg, i.v.) and the combination of both antibodies. Two groups remained untreated and were used as a positive control. After an incubation period of 24h fluorescent labeled Trastuzumab-Cy5 and Pertuzumab-Cy5 was injected i.v. in four groups each. *In vivo* imaging of the animals was conducted after another 24h, followed by the *ex vivo* histological analysis of all tumors (Fig. 10).

In the untreated control groups, the high binding specificity of Trastuzumab-Cy5 and Pertuzumab-Cy5 against the HER2 receptor was clearly visible (Fig. 10a,b). The pre-treatment with Trastuzumab lead to a very intense HER2 binding of Pertuzumab-Cy5 in the respective experimental group, whereas the specific binding of Trastuzumab-Cy5 with the HER2 receptor did not exist at all. The pre-treatment with Pertuzumab, however, showed an inverted binding behavior of Trastuzmab-Cy5 and Pertuzumab-Cy5 (Fig. 10e,f). Prior incubation with both therapeutic antibodies inhibited the following HER2 receptor binding of both fluorescent labeled antibodies (Fig. 10g,h).

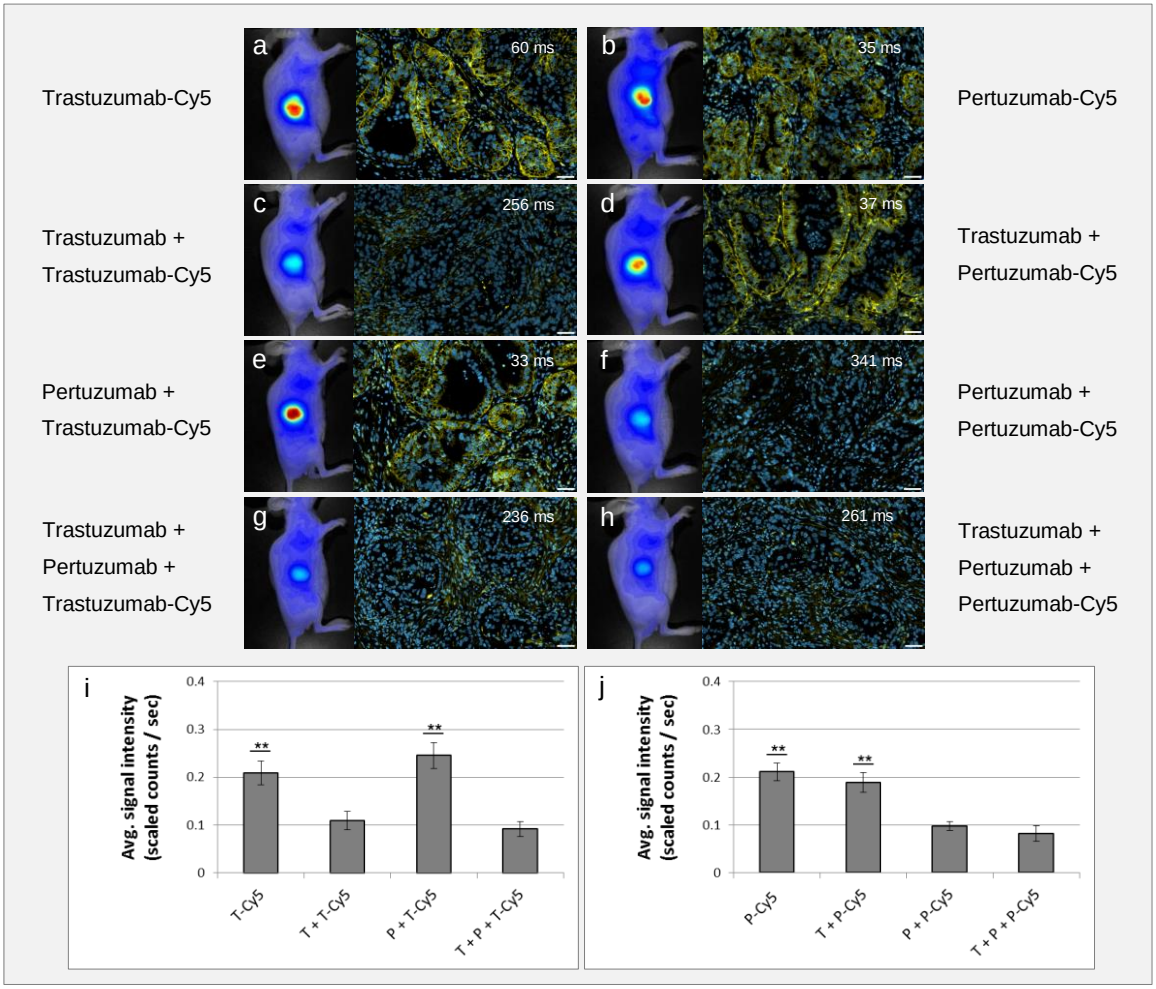

Figure 10: Binding site evaluation of two single fluorescent labeled anti-HER2 antibodies in Calu-3 xenografts. (a) *In vivo* and *ex vivo* imaging of the binding specificity of Trastuzumab-Cy5. (b) Imaging of the binding specificity of Pertuzumab-Cy5. (c) Imaging of the binding specificity of Trastuzumab-Cy5 pretreated with Trastuzumab. (d) Imaging of the binding specificity of Pertuzumab-Cy5 pretreated with Trastuzumab. (e) Imaging of the binding specificity of Trastuzumab-Cy5 pretreated with Pertuzumab. (f) Imaging of the binding specificity of Pertuzumab-Cy5 pretreated with Pertuzumab. (g) Imaging of the binding specificity of Trastuzumab-Cy5 pretreated with Trastuzumab and Pertuzumab. (h) Imaging of the binding specificity of Pertuzumab-Cy5 pretreated with Trastuzumab and Pertuzumab. (i) Diagram with the *in vivo* imaging results of Trastuzumab-Cy5. (j) Diagram with the *in vivo* imaging results of Pertuzumab-Cy5. All plots were compared to the *in vivo* signal intensity value of the control antibody Omalizumab-Cy5 (Fig. 6; 0.1 scaled counts / sec). T = Trastuzumab, P = Pertuzumab. Animals per group: n = 3. Values are given as mean ± s.d.. **P*<0.05, ** *P*<0.01, *** *P*<0.001, *t*-test. *Ex vivo* magnification: x40. Scale bar: 50 µm. The figure in the picture of the tissue slices represent the corresponding exposure time.

Conclusion

In vivo and *ex vivo* fluorescence imaging could show a distinct difference between the binding behavior of Trastuzumab-Cy5 and Pertuzumab-Cy5. Both antibody formats recognize different epitopes of the extra cellular HER2 receptor domain

Epitope evaluation of two fluorescent labeled anti-HER2 antibodies (mixture)

The following experiment should verify the possibility of gaining the prior results, referring to the HER2 epitope evaluation, also through an antibody mixture of Trastuzumab-Alexa647 and Pertuzumab-Alexa750. This imaging experiment reveals possible interactions between the two

therapeutic antibodies and is also able to examine their influence on the binding behavior. Further this experimental set-up reduces the number of mice, because both antibodies are tested in the same animal. Therefore, four groups of female SHO mice bearing s.c. Calu-3 tumors were formed (n = 3 mice/group, TV ± 150mm^3) and treated with Trastuzumab (10 mg/kg, i.v.), Pertuzumab (10 mg/kg, i.v.) and the combination of both antibodies. Two groups remained untreated and were used as control groups. After an incubation period of 24 hours, the mixture of fluorescent labeled Trastuzumab-Alexa647 and Pertuzumab-Alexa750 was intravenously applied to the different groups. *In vivo* imaging of the mice was conducted after another 24 hours, followed by the *ex vivo* analysis of the experimental animals (Fig. 11).

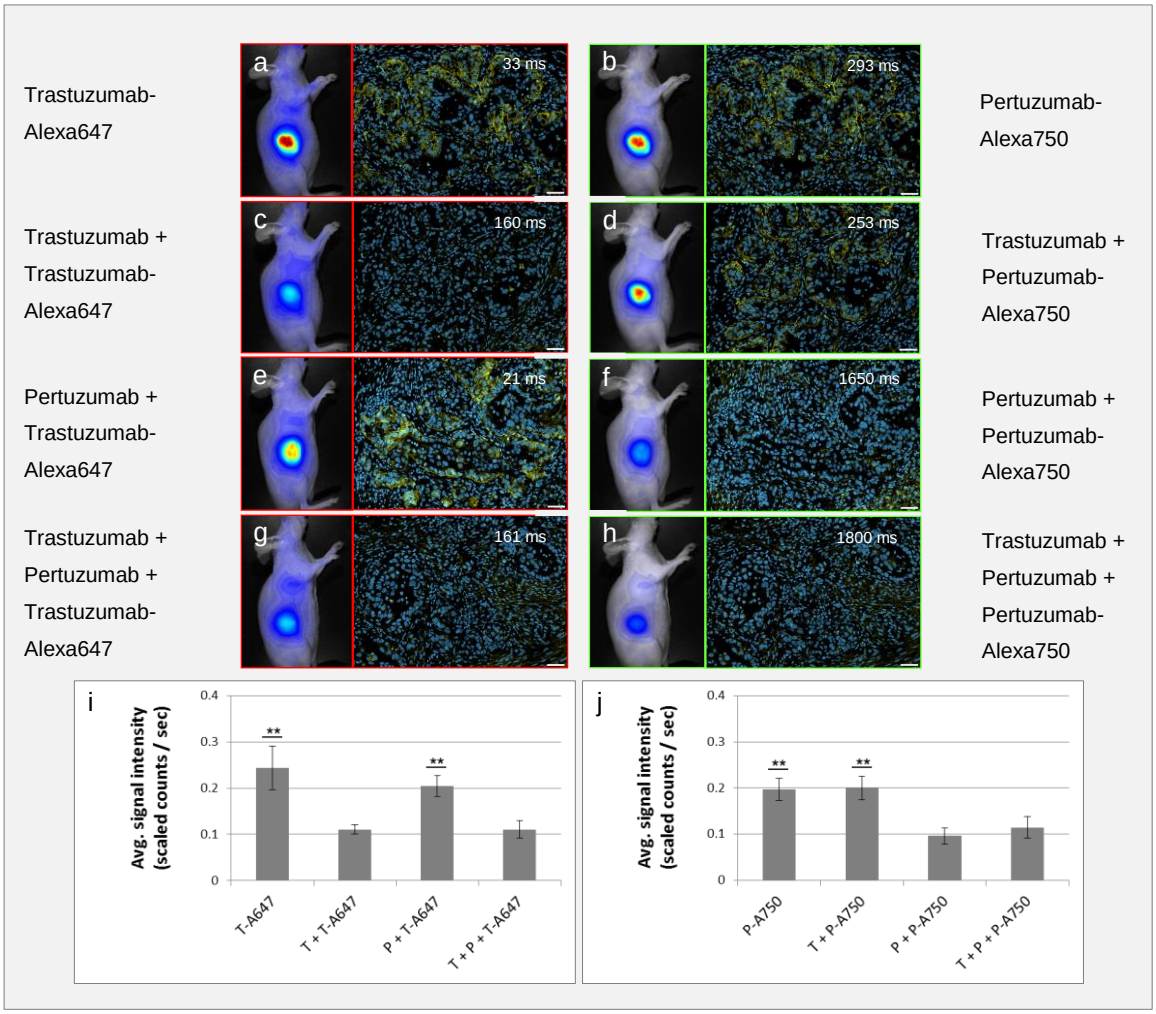

Figure 11: Simultaneous binding site evaluation with a mixture of two fluorescent labeled anti-HER2 antibodies in Calu-3 xenografts. (a) *In vivo* and *ex vivo* imaging of the binding specificity of T-Alexa647. (b) *In vivo* and *ex vivo* imaging of the binding specificity of P-Alexa750. (c) Imaging of the binding specificity of T-Alexa647 pretreated with Trastuzumab. (d) Imaging of the binding specificity of P-Alexa750 pretreated with Trastuzumab. (e) Imaging of the binding specificity of T-Alexa647 pretreated with Pertuzumab. (f) Imaging of the binding specificity of P-Alexa750 pretreated with Pertuzumab. (g) Imaging of the binding specificity of T-Alexa647 pretreated with Trastuzumab and Pertuzumab. (h) Imaging of the binding specificity of P-Alexa750 pretreated with Trastuzumab and Pertuzumab. (i) Diagram with the *in vivo* imaging results of T-Alexa647. (j) Diagram with the *in vivo* imaging results of P-Alexa750. All plots were compared to the *in vivo* signal intensity value of the control antibody Omalizumab-Cy5 (Fig. 6; 0.1 scaled counts / sec). T = Trastuzumab, P = Pertuzumab. Animals per group: n = 3. Values are given as mean ± s.d.. *P<0.05, ** P<0.01, *** P<0.001, t-test. *Ex vivo* magnification: x40. Scale bar: 50 µm. The figure in the picture of the tissue slices represent the corresponding exposure time.

The simultaneous application of the antibody mixture in the untreated experimental animals showed an identical binding affinity and specificity to the HER2 overexpressed Calu-3 tumor cells for Trastuzumab-Alexa647, as well as for Pertuzumab-Alexa750. (Fig. 11a,b). As the previous experiment already showed, the pre-treatment with Trastuzumab and Pertuzumab prevented the binding of the identical fluorescent labeled antibody format, whereas the contrary fluorescence antibody displayed a specific binding to the target (Fig. 11c-f). During the combined pre-incubation of both antibody formats, all free epitopes were covered and no binding of fluorescent labeled antibodies occurred (Fig. 11g,h).

Conclusion

It is also possible to determine the respective binding epitopes via *in vivo* and *ex vivo* imaging by simultaneous application of different fluorescent labeled antibodies, which are directed against the same tumor cell receptor.

Comparing the imaging results with preclinical efficacy data

The information gained in the previous sections by using *in vivo* and *ex vivo* fluorescence imaging methods, regarding the high binding affinity and specificity of Trastuzumab and Pertuzumab against the HER2 receptor in Calu-3 xenograft, was evaluated in the following preclinical study. For this purpose, female SHO mice bearing s.c. Calu-3 tumors were divided in one control and two treatment groups, each with 8 animals per group. After reaching a tumor volume of approx. 100 mm^3, the animals received a once weekly application (20 mg/kg, i.v.) of Trastuzumab, Pertuzumab and Omalizumab, whereas the latter antibody was used as negative control. The development of the tumor volume was monitored over the time by caliper measurement. After completion of the efficacy study, all tumors were explanted and the tumor cell proliferation rate was examined via histological Ki67 staining (Fig. 12).

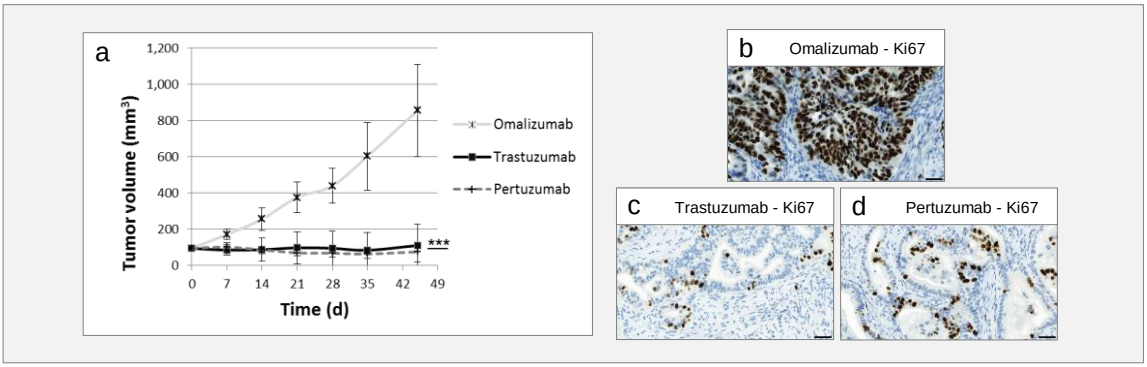

Figure 12: Preclinical efficacy study of two anti-HER2 specific antibodies in Calu-3 xenograft. (a) Tumor growth kinetics of the Calu-3 xenograft model treated with Trastuzumab and Pertuzumab. The antibody Omalizumab was used as a negative control. (b-d) Tissue slices of the control and treatment groups were stained for Ki67 to monitor the tumor cell proliferation rate. Animals per group: n = 8. Values are given as mean ± s.d.. *P<0.05, ** P<0.01, *** P<0.001, t-test. *Ex vivo* magnification: x40. Scale bar: 50 µm.

The previously reported high binding affinity and specificity of labeled Trastuzumab and Pertuzumab, lead in the conducted preclinical efficacy study to a strong therapeutic treatment effect. In comparison to the control antibody Omalizumab, both anti-HER2 antibody formats induced complete tumor growth stagnation in Calu-3 xenograft over the whole treatment period (Fig. 12a). The following histological Ki67 tissue analysis of the sliced tumor can be attributed to the strong reduction of the tumor cell proliferation rate (Fig. 12b-d).

Conclusion

The conducted preclinical efficacy study in the Calu-3 xenograft model show up that the treatment with both, Trastuzumab and Pertuzumab, causes a complete tumor growth regression.

4.2.2 Binding site evaluation of an anti-HER2 bispecific antibody

After the successful binding site evaluation of Trastuzumab and Pertuzumab in the prior proof-of-concept study applying *in vivo* and *ex vivo* fluorescence imaging, this procedure was also used in the following experiment to determine epitope evaluation and binding affinity and specificity of a new anti-HER2 bispecific antibody format (also named "Crossmab"). This heterodimeric antibody combines the binding sites of Trastuzumab and Pertuzumab in a conventional IgG format and therefore should provide the same target specificity and therapeutic treatment efficacy as the combination of both single antibody formats.

Binding specificity of the anti-HER2 Crossmab antibody

In the following experiment the binding affinity and specificity of the new anti-HER2 Crossmab format was compared to Trastuzumab and Pertuzumab. Therefore, female SHO mice bearing s.c. Calu-3 tumors (n = 3 mice/group, TV ± 150 mm^3) were divided in four treatment groups. One group received the control antibody Omalizumab-Cy5 and the other groups were injected with Cy5 labeled HER2 specific antibodies (2 mg/kg, i.v.). After 24 hours, the signal intensities of the labeled antibodies were measured in the tumor area via FRI. Afterwards, the antibody binding specificity was measured via ex *vivo* fluorescence imaging (Fig. 13).

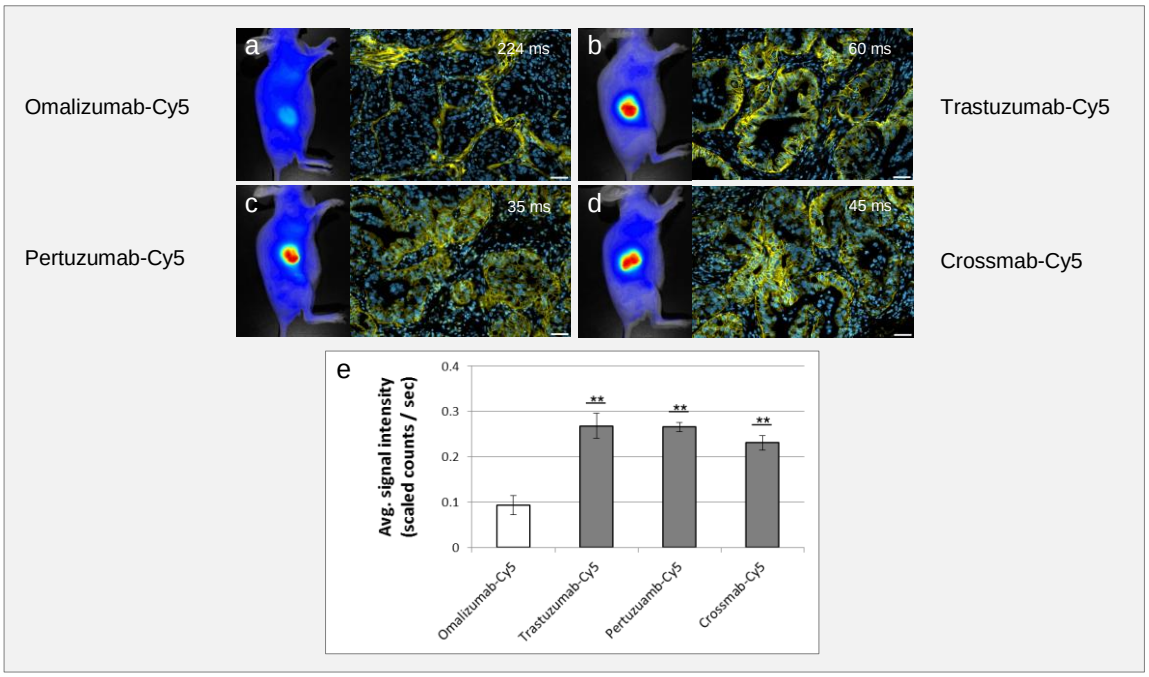

Figure 13: Binding specificity of three fluorescent labeled anti-HER2 antibodies in Calu-3 xenograft. (a) *In vivo* and *ex vivo* imaging of the binding specificity of control antibody Omalizumab-Cy5. (b) *In vivo* and *ex vivo* imaging of the binding specificity of Trastuzumab-Cy5. (c) *In vivo* and *ex vivo* imaging of the binding specificity of Pertuzumab-Cy5. (d) *In vivo* and *ex vivo* imaging of the binding specificity of Crossmab-Cy5. (e) Diagram with the *in vivo* imaging results. Grey plots were compared to the *in vivo* signal intensity value of the control antibody Omalizumab-Cy5. Animals per group: n = 3. Values are given as mean ± s.d.. *P<0.05, ** P<0.01, *t*-test. *Ex vivo* magnification: x40. Scale bar: 50 µm. The figure in the picture of the tissue slices represent the corresponding exposure time.

Compared to the Omalizumab-Cy5 treated control group, all three labeled anti-HER2 specific antibody formats showed a strong and mainly equal *in vivo* fluorescence signal in the tumor area (Fig. 13a-e). During the histological tissue slide analysis, no differences, referring to affinity and binding behavior, could be determined between the three anti-HER2 antibodies. The control antibody Omalizumab-CY5 could only be localized in murine stroma tissue.

Conclusion

The anti-HER2 Crossmab showed a specific binding to the over expressed HER2 receptor in the Calu-3 xenograft. No significant difference in the signal intensity between the classic IgG format of Trastuzumab/Pertuzumab and the bispecific antibody was visible. This raises the question of whether the two Crossmab receptor arms possess the same binding specificity to their antigen or if only one part of the antibody interact with the relevant target.

Epitope evaluation of anti-HER2 Crossmab antibody

In the following imaging experiment, a binding site evaluation of the anti-HER2 Crossmab was conducted. Therefore, five experimental groups with female SHO mice bearing s.c. Calu-3 tumors (n = 3 mice/group, TV ± 150 mm^3) were created and once pretreated with Trastuzumab (10 mg/kg, i.v.), Pertuzumab (10 mg/kg, i.v.), the combination of the previous anti-HER2 antibodies (10 mg/kg each, i.v.), and the Crossmab antibody (10 mg/kg, i.v.) as shown in Figure 14. One group remained untreated and served as a negative control. After 24 hours of incubation, fluorescent labeled Crossmab-Cy5 (2 mg/kg, i.v.) was applied. *In vivo* imaging of the experimental animals was conducted after another 24 hours followed by tumor explanation and histological *ex vivo* analysis.

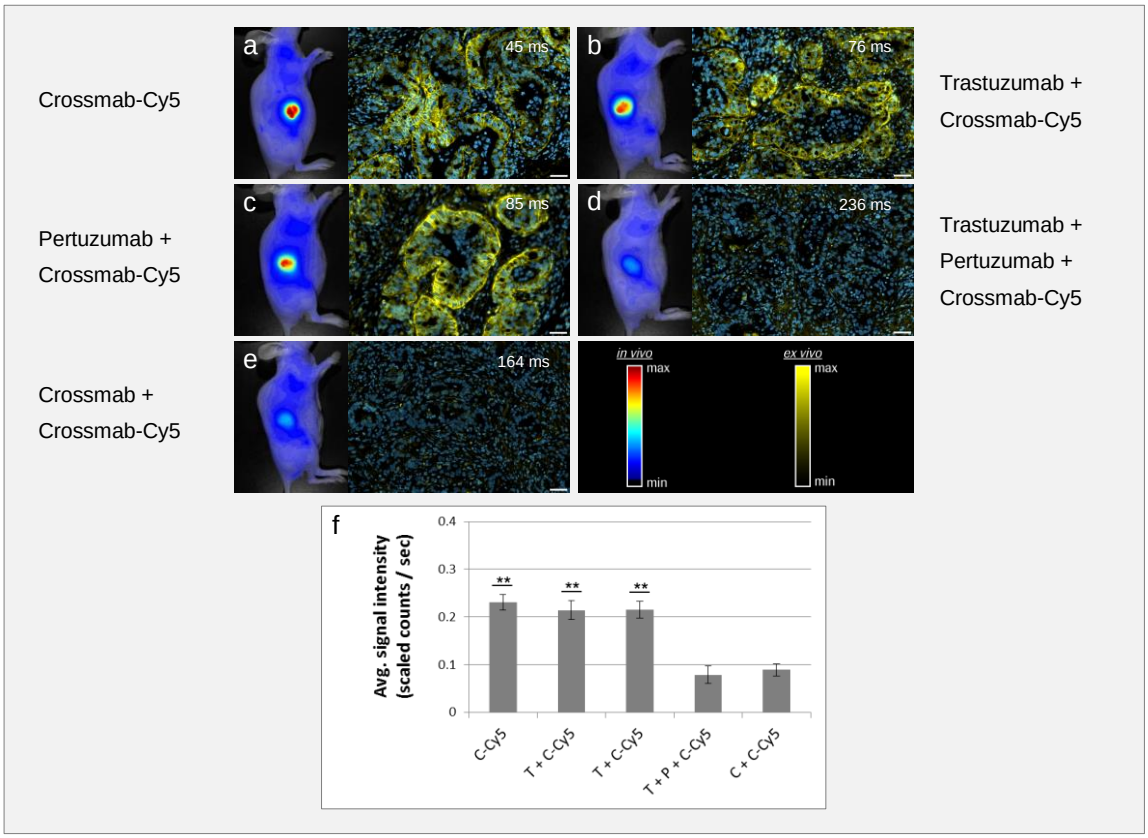

Figure 14: Binding specificity of anti-HER2 "CrossMab" antibody in Calu-3 xenograft. (a) *In vivo* and *ex vivo* imaging of the binding specificity of Crossmab-Cy5. (b) *In vivo* and *ex vivo* imaging of the binding specificity of Crossmab-Cy5

pretreated with Trastuzumab. (c) *In vivo* and *ex vivo* imaging of the binding specificity of Crossmab-Cy5 pretreated with Pertuzumab. (d) *In vivo* and *ex vivo* imaging of the binding specificity of Crossmab-Cy5 pretreated with the combination of Trastuzumab and Pertuzumab. (e) *In vivo* and *ex vivo* imaging of the binding specificity of Crossmab-Cy5 pretreated with the Crossmab. (f) Diagram with the *in vivo* imaging results. All plots were compared to the *in vivo* signal intensity value of the control antibody Omalizumab-Cy5 (Fig. 13, page 56). T = Trastuzumab, P = Pertuzumab, C = Crossmab. Animals per group: n = 3. Values are given as mean ± s.d.. **P*<0.05*, ** P*<0.01, *** *P*<0.001, *t*-test. *Ex vivo* magnification: x40. Scale bar: 50 µm.

The *in vivo* signal intensity in the control group and the resultant *ex vivo* binding affinity and specificities of Crossmab-Cy5 in the histological tissue slice (Fig. 14a), confirmed the imaging results gained in the previous section (Fig. 13d,e). Pre-treatment with Trastuzumab and Pertuzumab could not prevent the binding of Crossmab-Cy5 in the respective experimental groups (Fig. 14 b,c), whereas pre-incubation with Crossmab and the combination of Trastuzumab and Pertuzumab disable entire epitope binding of the labeled bispecific antibody (Fig. 14 d,e).

Conclusion

The new bispecific anti-HER2 Crossmab format possesses an outstanding binding affinity and specificity against the overexpressed HER2 receptor in Calu-3 xenograft model. Both arms of the bispecific antibody provide their full functionality and specificity towards the given HER2 antigen. Eventually it has to be examined, if the new antibody format can induce the same therapeutic treatment efficacy in the Calu-3 xenograft as the combination of Trastuzumab and Pertuzumab.

Comparing the imaging results with preclinical efficacy data

In the last two sections (4.2.2), the binding specificity and epitope evaluation for a new anti-HER2 bispecific Crossmab format was carried out by means of *in vivo* and *ex vivo* fluorescence imaging. The results gained from those experiments showed no obvious differences between Trastuzumab, Pertuzumab, and the new Crossmab format, regarding epitope detection and receptor specificity. The following preclinical experiment examined the therapeutic efficacy of the bispecific anti-HER2 format in comparison to Trastuzumab/Pertuzumab combination therapy. Therefore, female SHO mice bearing s.c. Calu-3 tumors were split into one control and two treatment groups, each with 10 animals per group. After reaching the tumor volume of approx. 100 mm^3, the different therapeutic antibodies were applied once weekly, (Omalizumab and Crossmab: 20 mg/kg, i.v.; Trastuzumab + Pertuzumab: 10 mg/kg each, i.v.), using the IgE specific antibody Omalizumab as a negative control. The tumor volume of the animals was monitored over the time by caliper measurement. After completion of the efficacy study, all tumors were explanted and the determination of the tumor cell proliferation rate was conducted via IHC staining of the Ki67 marker (Fig. 15).

In comparison to the control group, both treatment strategies, the combination of Trastuzumab and Pertuzumab as well as the treatment with the new anti-HER2 Crossmab format, achieved a strong and significant therapeutic effect in HER2 overexpressed Calu-3 xenograft (Fig. 15a). After a treatment period of seven weeks, no significant differences of the tumor volume between the two treatment strategies were visible. Furthermore, both treatment groups showed a slide increase of the tumor volume at the end of the experiment

(day 49). This slowly developing treatment resistance against both therapies could also be confirmed in the histological analysis of the Ki67 tissue staining (Fig. 15 b-d).

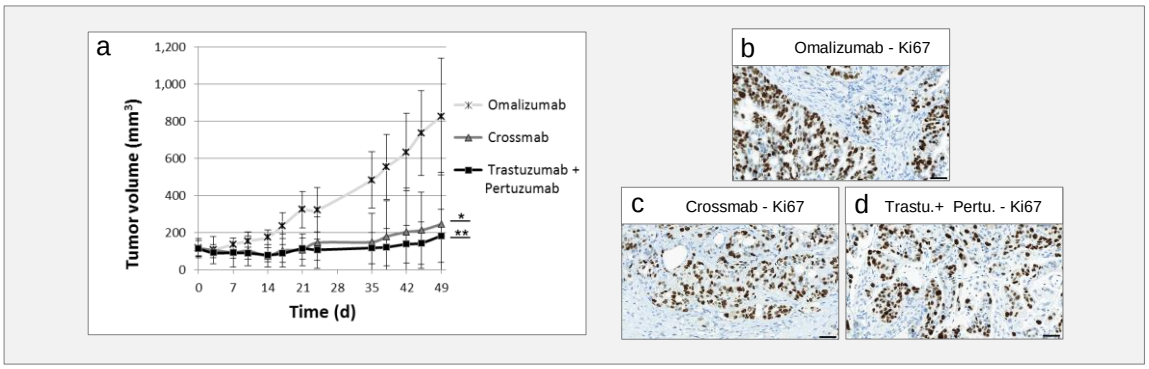

Figure 15: Preclinical efficacy study of anti-HER2 bispecific heterodimeric IgG antibody in correlation with Trastuzumab and Pertuzumab combination therapy. (a) Tumor growth kinetics of the Calu-3 xenograft model treated with Crossmab and the combination of Trastuzumab and Pertuzumab. The IgE specific antibody Omalizumab was used as a negative control. (b-d) Tissue slices of the control and treatment groups were stained for Ki67 to monitor the tumor cell proliferation rate. Animals per group: n = 10. Values are given as mean ± s.d.. *P<0.05, ** P<0.01, *** P<0.001, t-test. *Ex vivo* magnification: x40. Scale bar: 50 µm.

Conclusion

Compared to the combination therapy of Trastuzumab and Pertuzumab, the new anti-HER2 bispecific antibody showed nearly the same therapeutic efficacy in the NSCLC Calu-3 xenograft model. Hence, it could be proved the both Crossmab arms possess a high affinity and specificity to the different Her2 receptor epitopes.

4.3 Selection of the most suitable xenograft model

The use of fluorescent labeled therapeutic antibodies for the evaluation of the tumor cell receptor status and the binding specificity between antibodies and their respective receptor epitope could be shown on various examples in the prior sections. The following experiment verifies if this fundamental interaction mechanism between antibody and antigen can be used by fluorescence imaging to select a suitable xenograft model for preclinical efficacy studies. This point is a very important aspect in preclinical drug development, because only a convenient *in vivo* model, were the target of interest is strongly overexpressed possess the ability to reveal treatment effects of new therapeutic agents in a clear and sufficient way. The direct *in vivo* assessment of target expression using fluorescent labeled antibodies (also termed as "*in vivo* fluorescence histology") can help to overcome major problems of conventional IHC, such as inefficient antigen retrieval and the difficult selection of an appropriate non-therapeutic detection antibody; by searching the relevant tumor target with the associated therapeutic agent in the "natural" environment.

Evaluation of xenograft selection using fluorescence imaging

In the following experiment, the HER2 expression level of two different NSCLC xenograft models was determined by *in vivo* and *ex vivo* fluorescence imaging. Therefore, a control and treatment group of Calu-1 and Calu-3 bearing female SHO mice was prepared (n = 3 mice/group, TV ± 100 mm^3). The control groups of both xenograft models received

Omalizumab-Cy5 as a negative control, whereas the treatment groups were injected with Trastuzumab-Cy5 (2 mg/kg, i.v.). After an incubation period of 24 hours, *in vivo* fluorescence imaging of the animals was conducted, followed by tumor explanation and *ex vivo* histological analysis of all tumors (Fig. 16).

Comparing the binding affinity and specificity of Omalizumab-Cy5 (control group) and Trastuzumab-Cy5 (treatment group) in the Calu-1 xenograft model, no clear differences between both antibodies could be found by *in vivo* and *ex vivo* imaging (Fig. 16a,c,e). The therapeutic antibody Trastuzumab-Cy5 showed no specific binding to the tumor cells and is only located in the murine stroma tissue. On the other hand, Omalizumab-Cy5 (control group) and Trastuzumab-Cy5 (treatment group) binding in the Calu-3 xenograft model provided a different outcome. As already shown in prior sections, the control antibody Omalizumab-Cy5 is mainly localized in the murine stroma tissue, whereas Trastuzumab-Cy5 yields a strong and highly specific binding to the HER2 receptors (Fig. 16b,d,e).

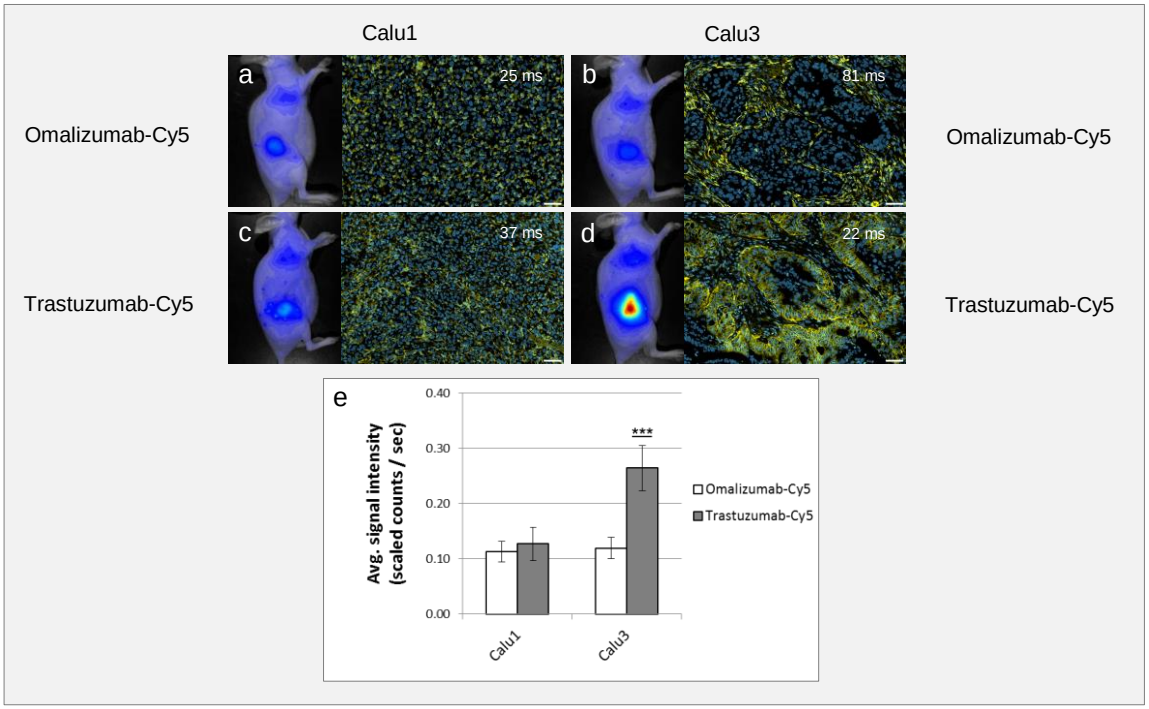

Figure 16: The use of fluorescence imaging to identify the most suitable xenograft. (a) *In vivo* and *ex vivo* binding specificity of the control antibody Omalizumab-Cy5 in Calu-1 xenograft. (b) *In vivo* and *ex vivo* binding specificity of the control antibody Omalizumab-Cy5 in Calu-3 xenograft. (c) *In vivo* and *ex vivo* binding specificity of Trastuzumab-Cy5 in Calu-1 xenograft model. (d) *In vivo* and *ex vivo* binding specificity of Trastuzumab-Cy5 in Calu-3 xenograft model. (e) Diagram with the *in vivo* imaging results. Animals per group: n = 3. Values are given as mean ± s.d.. **P*<0.05, ** *P*<0.01, *** *P*<0.001, *t*-test. *Ex vivo* magnification: x40. Scale bar: 50 µm. The figure in the picture of the tissue slices represent the corresponding exposure time.

Conclusion

The combination of *in* vivo and *ex vivo* fluorescence imaging using labeled therapeutic antibodies, provide the possibility for a distinct *in vivo* classification of the relevant tumor cell receptor status and therefore enable the selection of the most suitable xenograft model for a subsequent preclinical efficacy study.

Comparing the imaging results with preclinical efficacy data

The results gained from the previous imaging experiment were verified in the following preclinical study. Therefore, female SHO mice with s.c. bearing Calu-1 and Calu-3 tumors were created and each xenograft was split into one control and treatment group (n = 10 mice/group). After reaching a tumor volume of approx. 100 mm^3, the therapeutic antibodies Trastuzumab and Omalizumab were applied once weekly (20 mg/kg, i.v.), whereas the IgE specific antibody Omalizumab served as a negative control. The tumor volume of all animals was monitored over the time by caliper measurement. After completion of the efficacy study, all tumors were explanted and histological examination of the tumor cell proliferation rate was conducted by Ki67 tissue staining (Fig. 17).

The preclinical efficacy study with Omalizumab and Trastuzumab in the Calu-1 xenograft model, showed no therapeutic treatment effects (Fig. 17a). Tumor growth kinetics of both agents had only minor changes, which was also reflected by identical tumor cell proliferation rates in the Ki67 stained tissue slices (Fig. 17 c,d). However, in the Calu-3 xenograft model, the treatment with Trastuzumab lead to a significant tumor growth inhibition compared to the control antibody (Fig. 17b). The subsequent histological tissue analysis showed a strong decrease of the tumor cell proliferation rate in the Trastuzumab treated tumors (Fig. 17e, f).

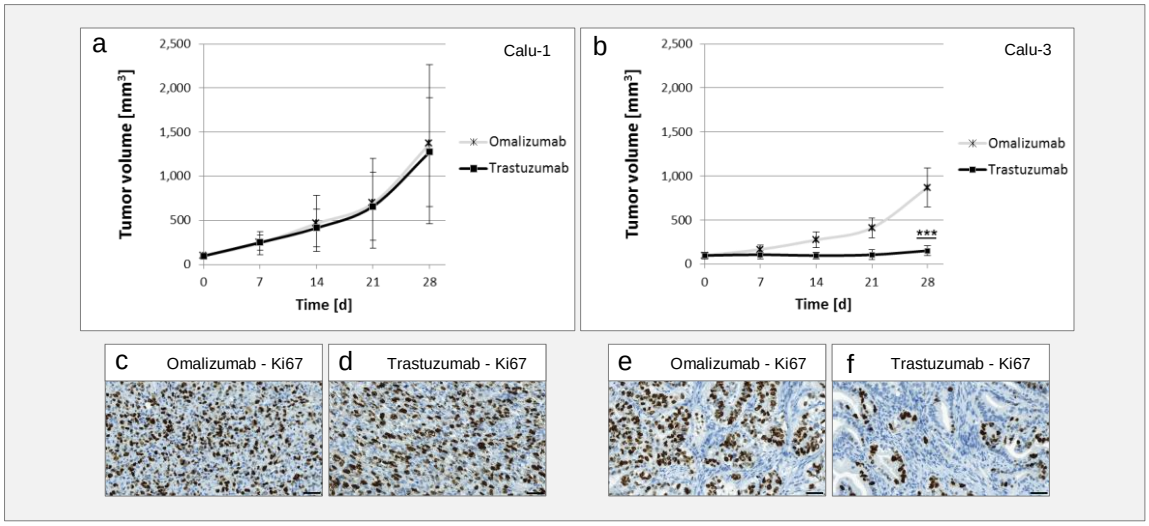

Figure 17: Preclinical efficacy study of Omalizumab and Trastuzumab in Calu-1 and Calu-3 xenograft. (a) The diagram showing the tumor growth kinetics of Omalizumab (control) and Trastuzumab treated Calu-1 tumors. (b) The diagram showing the tumor growth kinetics of Omalizumab (control) and Trastuzumab treated Calu-3 tumors. (c, d) Single Calu-1 tissue slice of the control and treatment group was stained with Ki67 to monitor the tumor cell proliferation rate. (e, f) Single Calu-3 tissue slice of the control and treatment group was stained with Ki67 to monitor the tumor cell proliferation rate. Animals per group: n = 10. Values are given as mean ± s.d.. *P<0.05, ** P<0.01, *** P<0.001, t-test. *Ex vivo* magnification: x40. Scale bar: 50 µm.

Conclusion

The gained results from the xenograft prioritization, created on the basis of fluorescence imaging, could be verified in the subsequent preclinical efficacy study. As predicted by the fluorescence imaging results, Trastuzumab developed no therapeutic effect in the Calu-1 xenograft model, whereas the tumor growth inhibition in the Calu-3 xenograft was clearly evident. Therefore, *in vivo* and *ex vivo* fluorescence imaging is a powerful technique for the prioritization and selection of the most suitable xenograft model.

4.4 Identification of the optimal treatment dosage

The identification of the optimal treatment dosage is a very important parameter for carrying out a preclinical efficacy study. The perfect treatment dosage should develop the highest possible therapeutic treatment effect and cause no or, if so, only a very low side-effect in the experimental animal. For the conventional determination the optimal treatment dosage, different concentrations of the therapeutic agent are tested in several treatment groups and the most effective dosage will be selected for further preclinical studies. In the following section it was verified, if the optimal treatment dosage can be determined by *in vivo* and *ex vivo* fluorescence imaging. Furthermore, the obtained imaging results were also correlated to the preclinical treatment response.

Evaluation of the optimal treatment dosage using fluorescence imaging

To determine the optimal treatment dosage, two control and four treatment groups of female SHO mice bearing s.c. Calu-3 tumors were created (n = 10 mice/group, s.c., TV ± 100 mm^3). The several treatment groups were pretreated with different concentrations of Trastuzumab (1, 3, 10 and 20 mg/kg; i.v.). After an incubation period of 24 hours, Trastuzumab-Cy5 was applied to one control and all treatment groups (2 mg/kg; i.v.), whereas the same amount of the IgE specific antibody Omalizumab-Cy5 was injected in the second control group and serves as a negative control. *In vivo* imaging of all experimental animals was conducted after another 24 hours, followed by the explanation of two tumors per group. Afterwards, the obtained tumor samples were analyzed by fluorescence microscopy (Fig. 18).

The *in vivo* imaging results of the Trastuzumab-Cy5 treatment groups displayed a constant reduction of the fluorescence intensity in the tumor areas with increased concentration of the pre-treatment dosage (Fig. 18b-g). The fluorescence intensity of Trastuzumab-Cy5 in the 20 mg/kg pre-treated animals was reduced to a minimum (Fig. 18f,g) and thus possess no significant difference to the control group of Omalizumab-Cy5 (Fig. 18a,g). Subsequent *ex vivo* analysis of the fluorescence intensity and binding specificity confirmed the prior *in vivo* results. Compared to the untreated Trastuzumab-Cy5 control group (Fig. 18b), pre-treatment of 1 mg/kg Trastuzumab had no obvious influence on the following binding of Trastuzumab-Cy5 to the HER2 receptor, whereas pre-treatment with 3, 10 and 20 mg/kg reduces successively the fluorescence signal of Trastuzumab-Cy5 to a minimum (Fig. 18d-f). Beside the visible detection of the reduced Trastuzumab-Cy5 binding to the tumor cells, this pre-treatment effect could be also reflected based on the exposure time of the current fluorescence tissue slice (Fig. 18a-f, white numbers).

Conclusion

The performed *in vivo* and *ex vivo* fluorescence imaging study in Calu-3 xenograft was able to determine the optimal treatment dosage for Trastuzumab. A treatment dosage with 1, 3 and 10 mg/kg Trastuzumab would not cover all free HER2 receptors and therefore increases the potential for inefficient treatment efficacy. A sufficient and overall HER2 receptor coverage in Calu-3 tumors (depending on the tumor size), will only be occur with a treatment dosage of 20 mg/kg Trastuzumab.

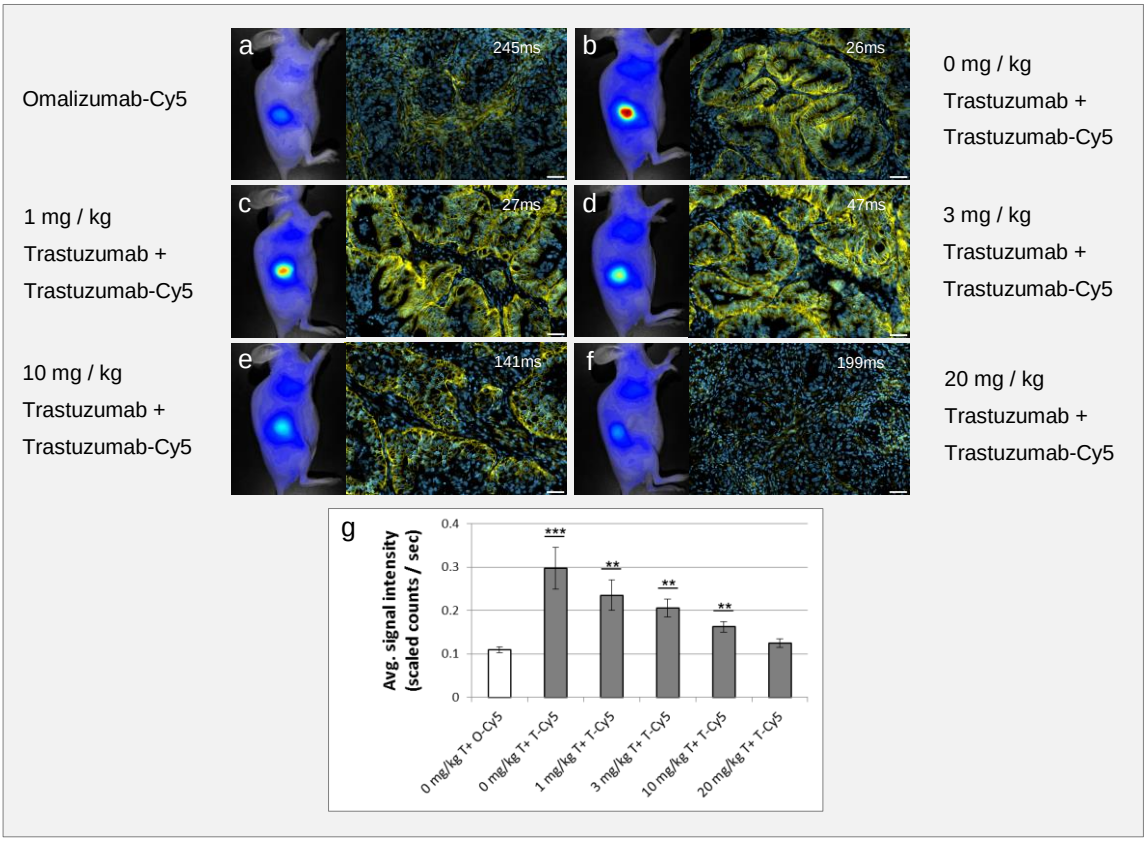

Figure 18: The use of *in vivo* and *ex* vivo fluorescence imaging to determine the optimal treatment dosage. (a) *In vivo* and *ex vivo* imaging was used to visualize the binding specificity of Omalizumab-Cy5 (control). (b) *In vivo* and *ex vivo* imaging was used to visualize the binding specificity of Trastuzumab-Cy5. (c-f) *In vivo* and *ex vivo* imaging was used to visualize the binding specificity of Trastuzumab-Cy5 pretreated with different concentration of Trastuzumab. (g) Diagram of the *in vivo* imaging results. The grey plots were compared to the *in vivo* signal intensity value of the control antibody Omalizumab-Cy5. O = Omalizumab, T = Trastuzumab, P = Pertuzumab. Animals per group: n = 10. Values are given as mean ± s.d.. *P<0.05, ** P<0.01, *** P<0.001, *t*-test. *Ex vivo* magnification: x40. Scale bar: 50 µm. The figure in the picture of the tissue slices represent the corresponding exposure time.

Comparing the imaging results with preclinical treatment response

The optimal Trastuzumab treatment dosage for the Calu-3 xenograft model gained from the previous imaging experiment was verified in the following preclinical study. Therefore, the animals from the prior experiment (n = 8 mice/group) received the same pre-treatment concentration of Trastuzumab, but this time in a once weekly application mode. The control group was treated with 20 mg/kg Omalizumab and the treatment groups were injected with different concentrations of Trastuzumab (0, 1, 3, 10, 20 mg/kg; i.v.). The tumor volume of all animals was monitored over the time by caliper measurement. After completion of the efficacy study, all tumors were explanted and histological examination of the tumor cell proliferation rate was conducted by Ki67 staining (Fig. 19).

In comparison to both control groups, all different Trastuzumab concentration leads to a significant tumor growth inhibition after a treatment period of nine weeks (Fig. 19a). At this final time point, tumors treated with 1, 3, and 10 mg/kg Trastuzumab already showed a constant tumor growth rate, whereas the treatment dosage of 20 mg/kg Trastuzumab still achieved constant tumor growth inhibition. The results from tumor volume measurement were also confirmed by histological tissue staining of Ki67 proliferation marker. Except the

group treated with the highest Trastuzumab dosage (20 mg/kg), all other treatment groups showed no difference in tumor cell proliferation rate compared to the control group (Fig. 19b-g).

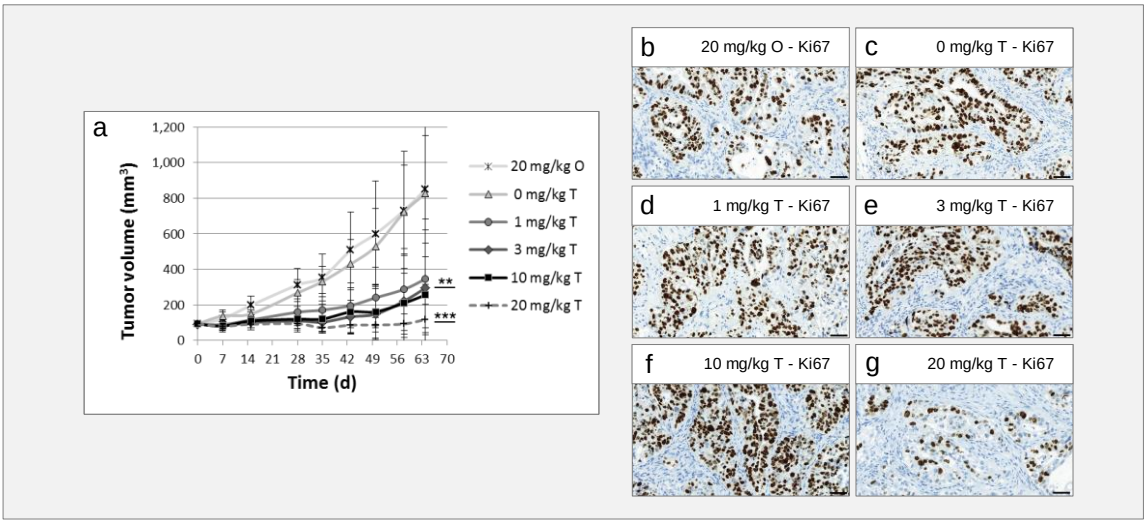

Figure 19: Preclinical efficacy study in a Calu-3 xenograft to determine the optimal treatment dose of Trastuzumab. (a) Tumor growth kinetics of the Omalizumab treated contol group in comparison to Trastuzumab treatment. (b-g) The tissue slices of the control and treatment groups were stained with Ki67 to indentify the tumor cell proliferation rate. Animals per group: n = 8. Values are given as mean ± s.d.. **P*<0.05, ** *P*<0.01, *** *P*<0.001, *t*-test. *Ex vivo* magnification: x40. Scale bar: 50 µm.

Conclusion

The combination of *in vivo* and *ex vivo* fluorescence imaging was able to determine the optimal Trastuzumab concentration for the treatment of Calu-3 xenograft. The predicted antibody dosage of 20 mg / kg achieved the best therapeutic treatment effects during the preclinical efficacy study.

4.5 Identification of the best application time point

Beside the determination of the optimal treatment dosage for a therapeutic antibody, the identification of the optimal application time point is another important aspect for preclinical efficacy studies. The complete coverage of all tumor cell receptors by the therapeutic agent is a pre-requisite for a successful tumor therapy. The penetration behavior of therapeutic antibodies in the tumor tissue depends on different tumor factors as well as on the antibody design. To monitor and understand the complex coherence and interaction of the variety of those factors is very difficult and partly still impossible. The conventional way to receive the optimal application time point for a therapeutic antibody is the preclinical testing of a pre-defined treatment dosage at different application intervals. Since this method is very laborious and time-consuming and, above all, requires a large number of animals, the following experiment will evaluate the possibility of determining this important parameter via fluorescence imaging.

Receptor evaluation with fluorescent labeled antibodies

To determine the optimal application time point for different therapeutic dosages, female SHO mice bearing s.c. Calu-3 tumors were split into five treatment groups (n = 5 mice/group, TV ± 100 mm^3). The groups were treated with different concentrations of Trastuzumab-Cy5 (1, 3, 10, 20 and 30 mg/kg; i.v., once). After an incubation time of 1, 7, 14 and 21 days, the fluorescence intensity in the tumor area was measured via *in vivo* imaging and in addition to that the tumor volume was also collected by caliper measurement.

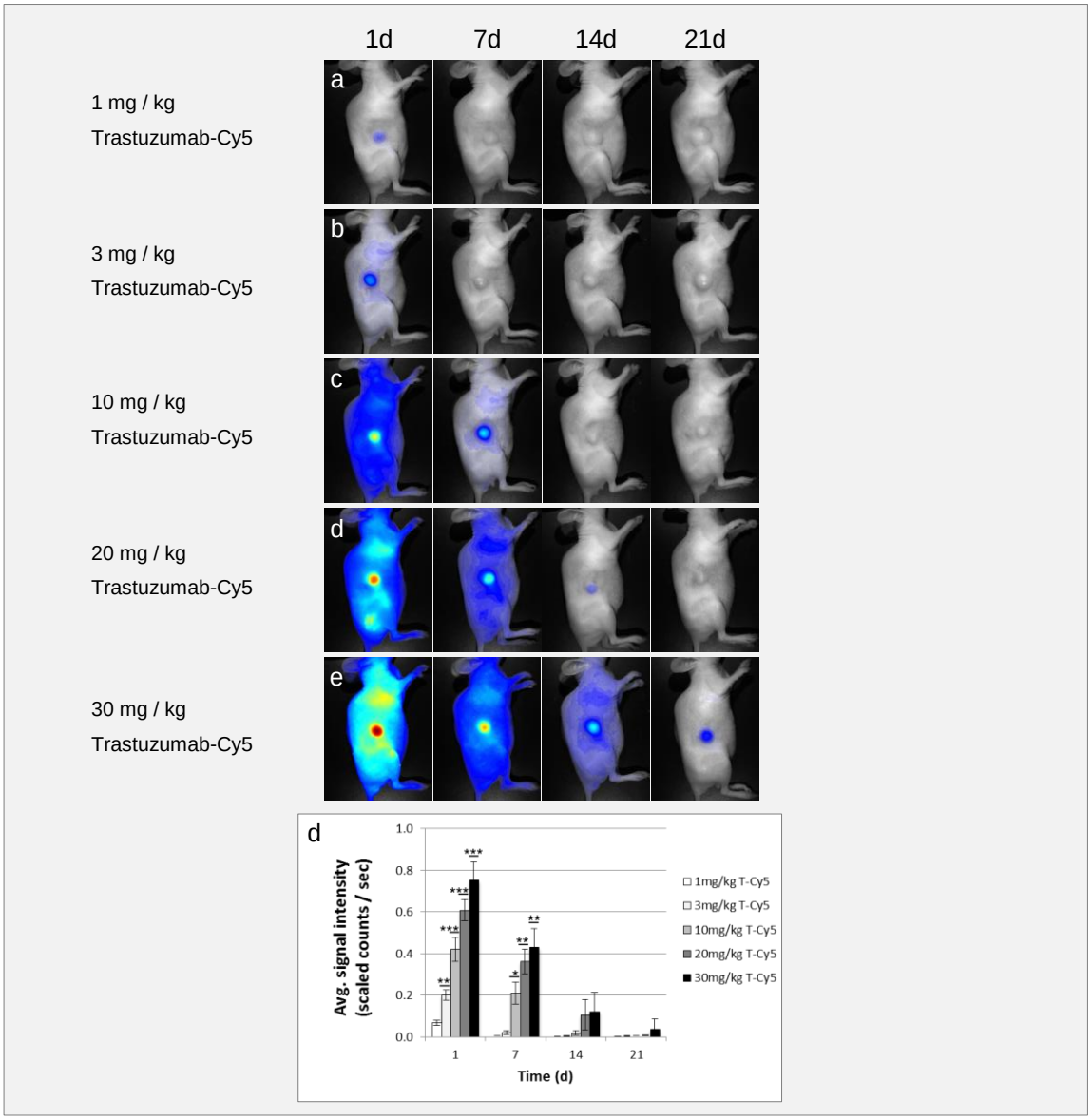

Figure 20: The use of *in* vivo and *ex* vivo fluorescence imaging to determine the optimal application time point. (a) *In vivo* imaging of the PK properties of 1 mg/kg T-Cy5. (b) *In vivo* imaging of the pharmacokinetic properties of 3 mg/kg T-Cy5. (c) *In vivo* imaging of the PK properties of 10 mg/kg T-Cy5. (d) *In vivo* imaging of the PK properties of 20 mg/kg T-Cy5. (e) *In vivo* imaging of the PK properties of 30 mg/kg T-Cy5. (g) Diagram of the *in vivo* imaging results. All plots were compared to the *in vivo* signal intensity value of the control antibody Omalizumab-Cy5 (Fig. 18). T = Trastuzumab. Animals per group: n = 5. Values are given as mean ± s.d.. **P*<0.05, ** *P*<0.01, *** *P*<0.001, *t*-test.

One day after Trastuzumab-Cy5 injection a concentration dependent signal intensity gradient could be detected in the tumor region of the different treatment groups (Fig. 20). At this, 1 mg/kg Trastuzumab-Cy5 showed the slightest and 30 mg/kg Trastuzumab-Cy5 the strongest

signal intensity. After an incubation period of seven days, the concentration in the mice injected with 1 and 3 mg/kg labeled antibody was below the specificity value of the control antibody Omalizumab-Cy5 (value: 0.1 scaled counts/sec, obtained from Fig. 18). Only the animals treated with 10, 20, and 30 mg/kg Trastuzumab-Cy5 showed a sufficient signal in the tumors. Two weeks after starting the therapy, it was only the antibody concentration of 30 mg/kg Trastuzumab-Cy5 that was above the specificity value and after an incubation period of 21 days, no sufficient fluorescence signal could be detected (Fig. 20e). In the following section, the fluorescence intensities were compared to the respective tumor volumes.

Comparing the imaging results with preclinical treatment response

The application time points predicted via fluorescence *in vivo* imaging were compared to the respective tumor growth curve (Fig. 21). After a treatment period of seven days, a significant increase in the tumor volume could be observed with an concentration of 1 and 3 mg/kg Trastuzumab-Cy5, whereas all other treatments (10, 20, 30 mg/kg) reduced the tumor growth rate considerably. The injected antibody concentration of 10 mg/kg Trastuzumab-Cy5 achieved after 21 days a significant growth rate compared to the initial tumor volume. After 28 days, the tumors treated with the 20 mg/kg labeled antibody also reached this significance criteria. Only the single application with 30 mg/kg could keep a relatively constant tumor volume up to this time point, but after that a constant increase in tumor volume could also be detected in this treatment group.

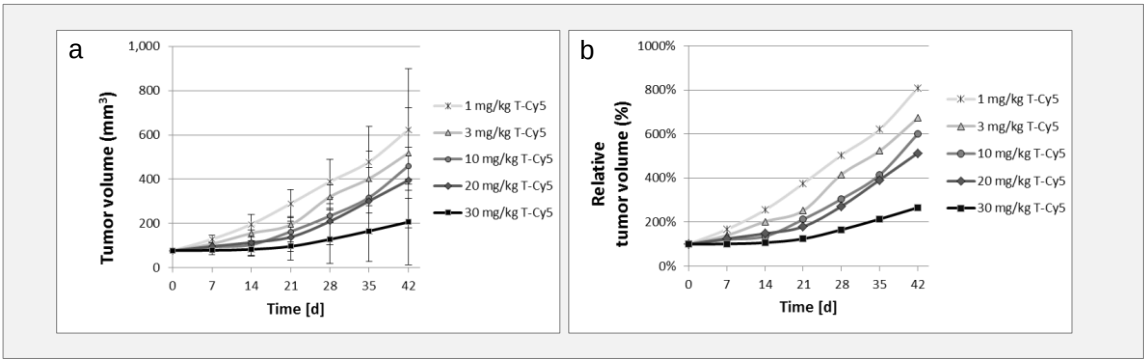

Figure 21: Preclinical efficacy study in a Calu-3 xenograft model to determine the optimal application time point. (a,b) The diagram illustrates the therapeutic treatment effect of different Trastuzumab-Cy5 concentration on tumor growth kinetics. The animals were treated with a single antibody application. Animals per group: n = 5. Values are given as mean ± s.d.

Conclusion

The non-invasive monitoring of fluorescence labeled antibodies, allows a concentration depending pharmacokinetic consideration of Trastuzumab-Cy5 in the subcutaneous Calu-3 tumor area. By monitoring the distribution, penetration, specific target interaction, and clearance of the labeled antibodies in the tumor region, the pharmacokinetic behavior and therefore the optimal application intervals of Trastuzumab-Cy5 could be determine. For the therapeutic dosages of 1-3 mg/kg Trastuzumab-Cy5, a single antibody application is not sufficient to cover all surface receptors in the tumor area. To receive an effective tumor response the treatment dosage must be increased (> 10 mg/kg) or a short daily application interval should be selected to accumulate the antibody concentration in the tumor region. For the treatment with 10–20 mg/kg Trastuzumab-Cy5 an application interval of approx. 7 days

could be predicted. When applying a treatment dosage of 30 mg/kg Trastuzumab-Cy5 a further injection should at least follow after 14 days. These imaging results were compared to the obtained tumor growth curves, and confirmed the gained imaging prognosis. The results clearly indicated that fluorescence *in vivo* imaging was able to produce reliable predictions in this xenograft model regarding the most suitable application time points.

4.6 Non-invasive pharmacokinetic drug measurement

The determination of the pharmacokinetic characteristics of therapeutic molecules represents an important part of the pharmaceutical developing process. Here from, conclusions can be drawn, regarding the distribution of therapeutic substances in the experimental animal model, the accumulation and interaction with corresponding goal structures, and the eventual excretion from the organism. The conventional way for the determination of pharmacokinetic parameters through blood analysis is extremely time-consuming and laborious and requires a large amount of experimental animals. Therefore, the possibility of detecting pharmacokinetic parameters of fluorescent labeled substances non-invasively over the eye will be discussed in the following sections. The eye is the perfect organ for light detection, because evolution specifically designed it for this purpose. Furthermore, the eye offers excellent optical access to the blood vessel system due to strong vascularization of the retina. Fluorescent light can pass the pupil and lens of the eye nearly without any light absorption and scattering and excite fluorescent molecules, circulating in the retina blood vessels. The emitting fluorescent light can leave the eye in the same way and is being detected outside by a sensitive CCD camera. This very simple measuring method offers the possibility for a non-invasive and repeated detection of pharmacokinetic parameters in the same experimental animal.

In the following sections, it was verified if planar reflectance imaging of the animals eye can be used for non-invasive monitoring of fluorescent substances and the determination of PK parameters (e.g. serum peak level - C_{max}, time to reach the maximum peak level - t_{max}, and serum half-life - $t_{1/2}$). The utility of this approach was demonstrated by evaluating three different compounds: i) indocyanine green (ICG) a non-targeting fluorescence dye; ii) OsteoSense750 a fluorescent labeled diphosphonate targeting bone tissue; and iii) Alexa750 labeled Trastuzumab, which targets the Her2 antigen expressed on the surface of tumor cells. These different compounds were tested in tumor free mice and in a human NSCLC xenograft model.

4.6.1 Evaluation of eye imaging with ICG - Feasibility

In order to evaluate the application of eye imaging for PK studies the average signal intensity (SI) of ICG was measured non-invasively over the time through the animal's eye. This compound is already used since 1959 as an indicator substance in different clinical application, such as the monitoring of liver or splanchnic perfusion and angiography in ophthalmology. The well-known pharmacokinetic properties and short half-life of ICG makes it eminently suitable for the evaluation of the new eye imaging method. Therefore, a tumor free SHO mouse (± 25 g) was manually injected i.v. via tail vein catheter with a single dosage of 10 µg ICG/100 µl PBS. Non-invasive fluorescence imaging (Maestro, exposure time: 200 ms, NIR filter) was recorded with a rate of one frame per second over a 6 minutes time period. The ROI was set over the animals' eye to detect the fluorescence intensity of ICG over the time (Fig. 22a and Video 1).

The eye imaging results indicated an immediate increase and followed by a sharp decline for the fluorescence signal intensity of ICG (Fig. 22b-e). The imaging data demonstrated that t_{max} of ICG was reached 10 seconds after i.v. injection and the half-life of the SI was 1.2 minutes (Fig. 22f).

Conclusion

Non-invasive fluorescence eye imaging possesses the ability to reveal the pharmacokinetic behavior of ICG in mice. The resultant serum level and half-life are in accordance to published data [228, 229].

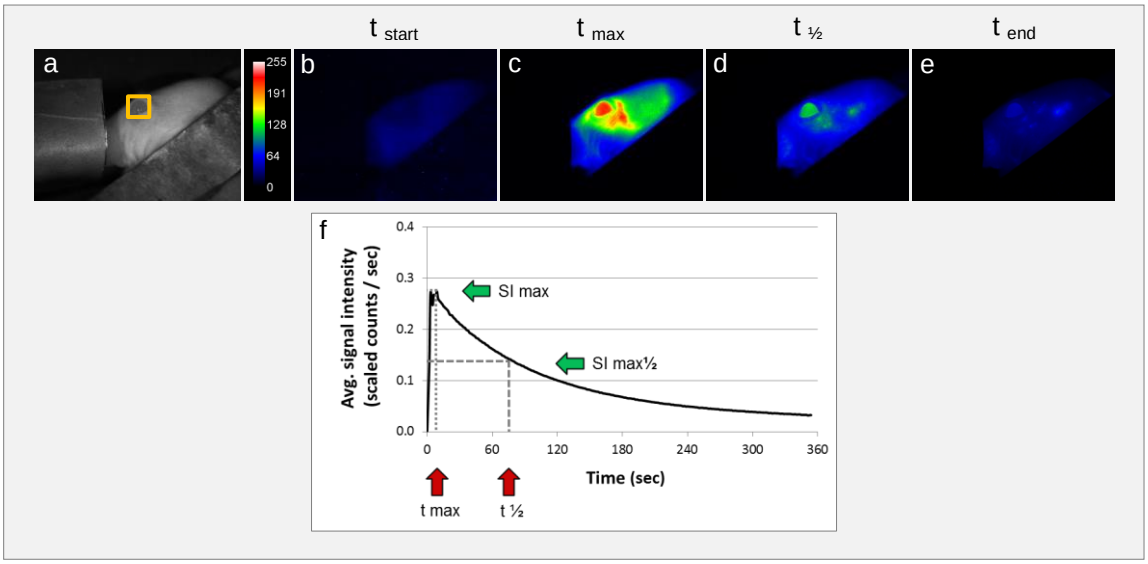

Figure 22: Pharmacokinetic eye imaging of single ICG application. (a) White light picture of the mouse head with the measurement region over the eye (insert yellow box). (b-d) Snap shots of fluorescence images at indicated time points after 10 µg ICG injection. Exposure time: 200 ms. (f) The diagram illustrates the curve shape of the fluorescence intensity in the region of interest. The maximum peak and the half-life of ICG were extracted from the diagram.

4.6.2 Evaluation of eye imaging with ICG - Reproducibility

The reproducibility of this method was assessed by manually administering multiple i.v. injections of 10 µg ICG/100 µl PBS into the same tumor free SHO mouse. After each ICG injection the signal intensity was measured (Maestro, exposure time: 200 ms, NIR filter) up for 6 minutes with a rate of one frame per second. The ROI was set over the animals' eye to detect the fluorescence intensity of ICG over the time (Fig. 23a and Video 2).

The acquired signal intensity of the three ICG applications revealed a nearly identical curve shape and showed only slight value variations (Fig. 23b-f). The t_{max} values for the different applications were almost identical (13, 15 and 15 sec), whereas the values for $t_{1/2}$ increased slightly over the time (1.8, 2.2 and 2.5 min). The increase of the serum half-life may be attributed to the limited clearing capacity of the liver.

Conclusion

The reproducibility of the eye imaging method was clearly demonstrated by measuring the fluorescence intensity of multiple ICG injections into the same animal.

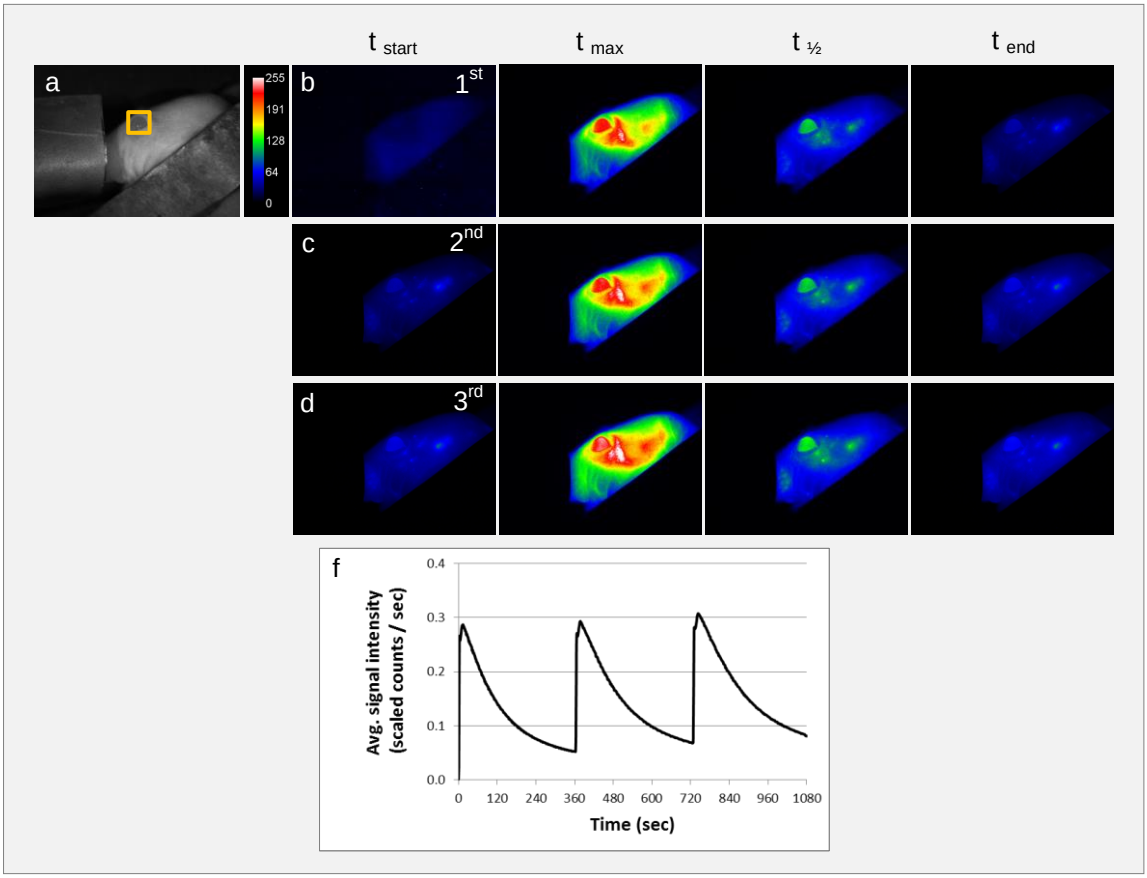

Figure 23: Pharmacokinetic eye imaging of repeated ICG application. (a) White light picture of the mouse head with the measurement region over the eye (insert yellow box). (b-d) Snap shots of fluorescence images at indicated time points after 1st (10 µg ICG), 2nd (10 µg ICG), and 3rd (10 µg ICG) injection. Exposure time: 200 ms. (f) The diagram illustrates the curve shape of the fluorescent intensity in the eye indicating maximum peak level and the half-life of each application.

4.6.3 Evaluation of eye imaging with ICG - Dose Dependency

In the following experiment it was examined if escalating dosages of ICG correlated with higher fluorescence signal intensities. Therefore, escalating ICG dosages of 5, 10 and 15 µg ICG were manually injected via tail vein catheter into the same tumor free SHO mouse (± 25 g). After each ICG injection the fluorescence signal was detected (Maestro, exposure time: 200 ms, NIR filter) up for 6 minutes with a rate of one frame per second. The ROI was set over the animals eye to detect the fluorescence intensity of ICG over the time (Fig. 24a and Video 3).

The results of this experiment demonstrated a linear correlation between the administered ICG dosages and the measured fluorescence peak intensities (Fig. 24b-d). Serum peak levels of the three applications occurred after 3 seconds however the serum half-life was starting to increase after the second ICG application (1.4; 1.3; 1.6 min respectively), which may be attributed to the limited clearing capacity of the liver. (Fig. 24f)

Conclusion

Dose dependency of different ICG concentrations can be detected and distinguished by measuring the fluorescence intensity in the eye of a mouse.

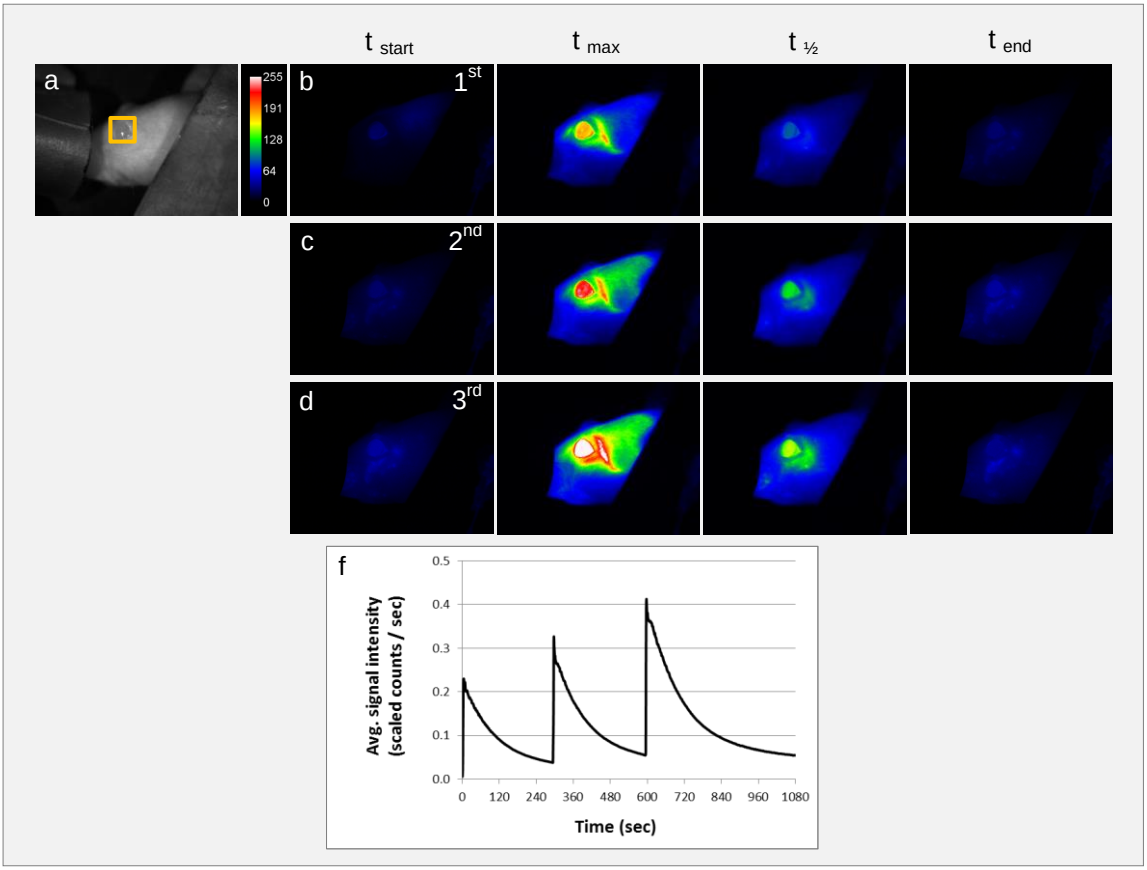

Figure 24: Pharmacokinetic eye imaging of escalating ICG dosages.(a) White light picture of the mouse head with the measurement region over the eye (insert yellow box). (b-d) Snap shots of fluorescence images at indicated time points after 1st (5 µg ICG), 2nd (10 µg ICG), and 3rd (15 µg ICG) injection of ICG. Exposure time: 200 ms. (f) The diagram illustrates the curve shape of the fluorescent intensity in the animals eye indicating maximum peak level and the half-life of each application.

4.6.4 Combination of eye and whole-body imaging with ICG

After the successful evaluation of the eye imaging method in the prior sections, the following experiments examined if PK measurements through the animals eye can be combined with whole-body fluorescence images. The combination of both approaches would facilitate the simultaneous measurement of serum kinetics with biodistribution kinetics. For this experiment a SHO mouse (± 25 g) was injected i.v. with 10 µg ICG/100 µl PBS and fluorescent signals were acquired (exposure time: 200 ms, NIR filter) in the left and right eye and the liver over a time period of 6 minutes with a rate of one frame per second (Fig. 25a and Video 4).

The results indicated an immediate increase and followed by a sharp decline of the fluorescence intensity in both eyes of the animal (left: t_{max} = 9 sec, $t_{1/2}$ = 1.3 min; right: t_{max} = 7 sec, $t_{1/2}$ = 1.2 min). Both curve shapes of the pharmacokinetic serum behaviour of ICG were more or less identical. The compound was quickly cleared out of the blood stream and accumulated in the liver (t_{max} = 186 sec, $t_{1/2}$ > 6 min) (Fig. 25b-c)

Conclusion

The combination of eye and whole-body imaging enables the simultaneous detection of serum kinetics and organ distribution. In terms of ICG, non-invasive fluorescence imaging was able to determine the serum peak level, half-life and accumulation area of the compound as described in the literature [228, 230-232].

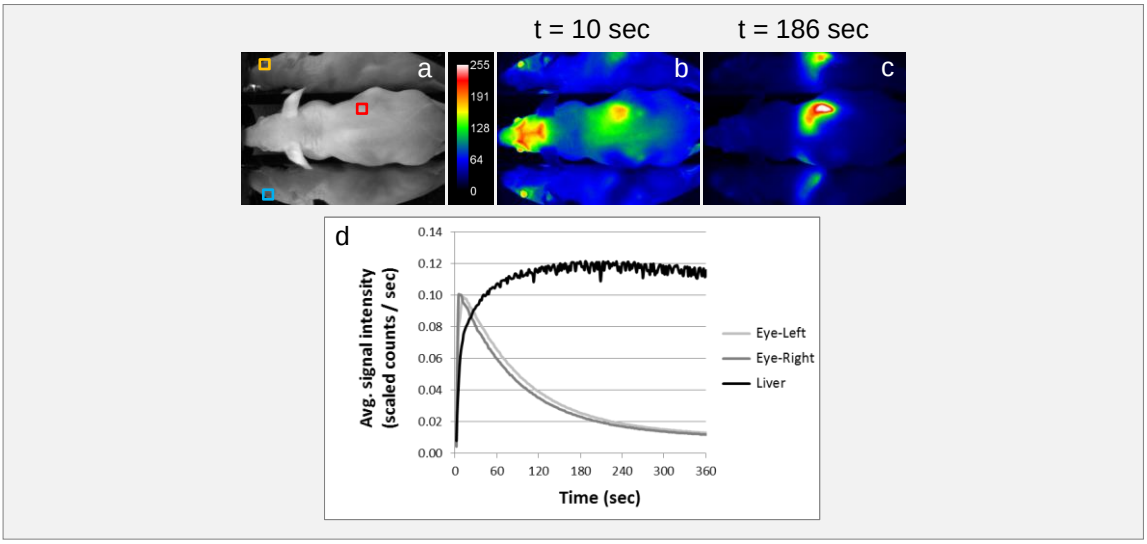

Figure 25: Pharmacokinetic eye and whole body imaging of ICG. (a) White light picture of the mouse with different regions of interest (right eye = yellow, left eye = blue and liver = red box insert). (b,c) The two fluorescence images illustrate exemplarily the signal intensity of ICG at 10 seconds (b) and 186 seconds (c) after compound injection. Exposure time: 200 ms. (d) The diagram illustrates the curve shape of the fluorescent intensity in the different measurement regions. The maximum peak and the half-life were extracted from the diagram.

4.6.5 Combination of eye and whole-body imaging with labeled diphosphonate

The eye imaging method was further evaluated using fluorescent labeled diphosphonate (OsteoSense750). The compound is a bone targeting agent and is mainly used in imaging areas of microcalcification and bone remodeling and enables imaging of bone growth and resorption [233]. The pharmacokinetic properties of the compound are also well-known because it is used in the clinic to treat osteoporosis, bone metastasis, multiple myeloma and other conditions involving fragile, breakable bone. The substance was manually injected via tail vein catheter into tumor free mice with a single dose of 2 nMol/100 µl PBS and the signal intensities were recorded (Maestro, exposure time: 500 ms, deep red filter) every 5 seconds for about 84 minutes. The ROI was set over the animals' eye to detect the fluorescence intensity of over the time (Fig. 26a).

The acquired distribution kinetic of OsteoSense750 demonstrates a transient accumulation in the kidneys and an immediate accumulation in the spine (Fig. 26b-e). Based on optical imaging measurements t_{max} was determined to be 3.8 minutes and serum half-life was 34 minutes (Fig. 26f).

Conclusion

The combination of eye and whole body imaging enabled the simultaneous detection of serum kinetics and organ distribution of OsteoSense750. The measured serum peak level, half-life and area of compound accumulation are in accordance with published data [233-236].

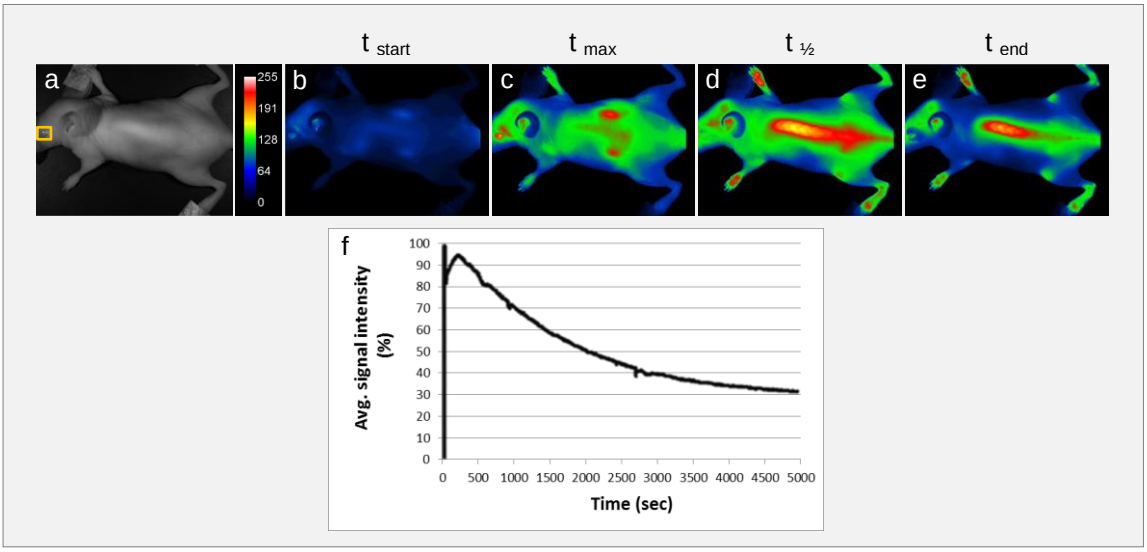

Figure 26: Pharmacokinetic eye and whole body imaging of OsteoSense750. (a) White light picture of the mouse with the measurement region over the eye (insert yellow box). (b-e) Snap shots of fluorescence images at indicated time points demonstrating fluorescence signal in the kidneys (c) and subsequently accumulation in bone tissue (d,e). Exposure time: 200 ms. (f) The diagram illustrates the curve shape of the fluorescence intensity in the eye revealing maximum peak level and serum half-life.

4.6.6 Combination of eye and whole-body imaging with labeled Trastuzumab

Finally, fluorescence eye imaging was examined for its utility to monitor serum levels and compound accumulation in tumor tissue simultaneously. For this purpose, the therapeutic antibody Trastuzumab was selected to determine its pharmacokinetic parameter and analyze the penetration, accumulation and clearance in a HER2 overexpressing xenograft. Thus, Alexa750 labeled Trastuzumab was manually injected as a single dose of 50 µg/100 µl PBS via tail vein catheter in a tumor free (Fig. 27a) and Calu-3 bearing SHO mouse (Fig. 27b). Due to the longer serum half-life of antibodies in mice longer observation periods are required [237]. Mice should not be hold under anesthesia for more than 2 hours and therefore one image per second was only acquired for 15 minutes (Maestro, exposure time: 200 ms, filter: deep red). Thereafter, daily *in vivo* measurements of the animals were performed for the next seven time points (Fig. 27).

Both animals reached nearly identical maximum signal intensities although at slightly different time points (tumor free: t_{max} = 6 sec, tumor bearing: t_{max} = 14 sec) (Fig. 27d). The differences in the maximum signal intensities may arise from the manual compound administration. For the tumor free mouse we determined Trastuzumab-Alexa750 serum half-life at 2.5 days which is similar to conventionally acquired published values [236, 237] (Fig. 27a,d). In contrast, the serum antibody concentration in the tumor bearing mouse was reduced significantly faster and thus, lead to a shorter serum half-life of only 1.2 days (Fig. 27b,d). This effect could be attributed to target mediated blood clearance of labeled Trastuzumab by the HER2 antigens. Specific binding of Trastuzumab-Alexa750 to the HER2 targets reduces circulating antibody and consequently the concentration in the blood is cleared in a much faster way. Accumulation of Trastuzumab-Alexa750 in the tumor region reached its peak level after 1 day and tumor half-life was calculated to be 2.8 days. Tumor tissue collected 24 hours after the application of the

compound was analyzed by fluorescence microscopy. The specific binding of Trastuzumab-Alexa750 to the HER2 expressing Calu-3 tumor cells was demonstrated (Fig. 27c).

Conclusion

The combination of eye and whole body imaging enables the simultaneous detection of serum kinetics and organ distribution. The measured serum level, half-life and area of compound accumulation are in accordance with published data [237-240].

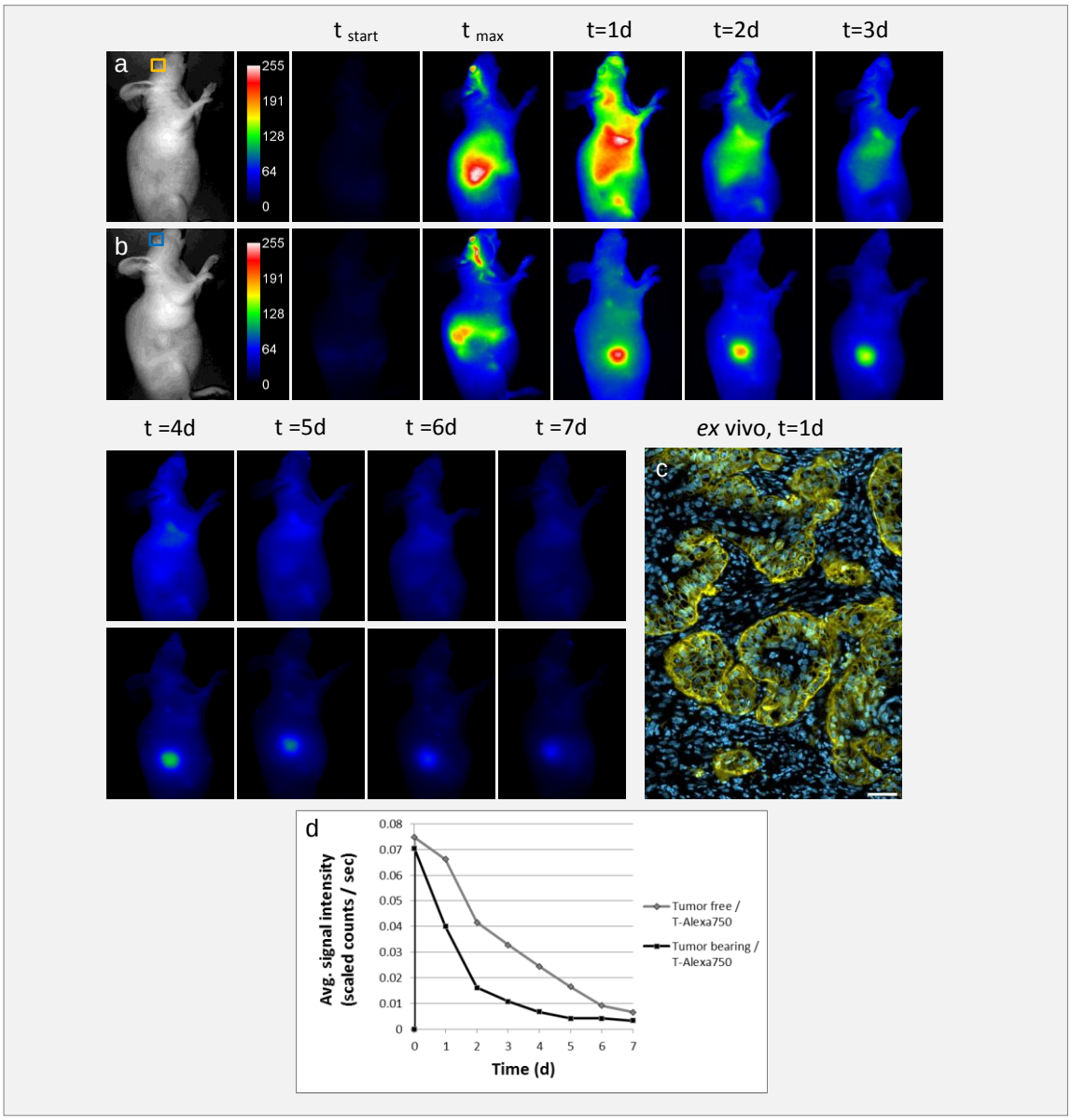

Figure 27: Pharmacokinetic eye and whole body imaging of Trastuzumab-Alexa750 in tumor free and Calu-3 bearing mice. (a) White light and fluorescence picture of a tumor free mouse with the region of interest over the eye (yellow box). Snap shots of fluorescence images at indicated time points demonstrating antibody injection, distribution, accumulation and clearance. (b) White light picture of tumor bearing mouse with the region of interest over the eye (blue box). Snap shots of fluorescence images at indicated time points demonstrating antibody injection, distribution, tumor accumulation and clearance. Exposure time: 200 ms. Filter: deep red. (c) Histological analysis of a single Calu-3 tumor was performed 24h after Trastuzumab-Alexa750 application, to determine binding specificity of the labeled antibody to the tumor cells. Scale bar: 50 µm. (d) The diagram illustrates the curve shape of the fluorescence intensity in the eye of a tumor free and tumor bearing mouse. The maximum peak and the half-life for Trastuzumab-Alexa750 were extracted from the diagram.

4.7 Ultramicroscopy for 3D tissue analysis

Ultramicroscopy is a new *ex vivo* fluorescence imaging method that uses lateral light-sheet illumination for the three-dimensional visualization of cleared specimen at cellular resolution. The detection of the entire specimen opens up a new insight into the visualization and analysis of biological aspects. The current areas of application of this post-mortem technology are the neurological investigation of GFP transfected neurons in mouse brain and spinal cord [179, 180, 191, 192]. The transfer of this promising imaging technique into the field of cancer research and drug development was described only very rarely in single publication until today [185].

In this thesis, ultramicroscopy was transferred into the field of tumor biology to three-dimensionally visualize multiple tumor parameters, such as tumor morphology and vessel architecture; at cellular resolution. Besides the detection of tumor morphology, also the penetration behavior of a fluorescent labeled antibody in the tumor tissue could be visualized in a three-dimensional way. The resultant virtual tumor slices of UM were also validated by conventional immunohistochemistry. In order to analyze the ultramicroscopy tumor data sets, a novel set of algorithms for the segmentation and quantification of multiple tumor parameters was developed.

In the following section, the use of ultramicroscopy for the visualization of different tumor parameter was evaluated and validated. Furthermore, the basic principle of the quantification software will be introduced and explained. This new imaging tool was applied to quantitatively monitor the anti-angiogenic treatment effect of Bevacizumab at different time points in KPL-4 breast cancer xenograft tumors and further observed the influence of vessel normalization on the subsequent penetration of fluorescent labeled Trastuzumab. Beside the visualization and quantification of xenograft tumors, the ultramicroscopy was also used to determine morphological information of other mouse organs.

4.7.1 Visualization of different tumor parameter and drug penetration

In the following section a proof-of-concept study in a breast cancer xenograft model was performed to validate the use of UM for the visualization of multiple tumor parameters and drug penetration. Therefore, a female SCID beige mouse with orthotopic KPL-4 breast cancer xenograft was injected with the HER2 specific antibody Trastuzumab-Alexa750 (2 mg/kg, i.v.) and six hours later Alexa647-labeled Lectin was also administrated (100 µg/mouse, i.v.). After five minutes of incubation the tumor was explanted, dehydrated and placed in an optical clearing solution. Thereafter, the cleared tumor sample was measured three-dimensionally at different wavelengths by UM.

4.7.1.1 Visualization of tumor morphology

For the visualization of tumor morphology the cleared specimen was placed in the imaging chamber of the ultramicroscope and excited the tissue with green laser light (543/22 nm). The different structural compositions and properties of tissue result in varying light absorption. As a consequence, the resulting autofluorescence is rich in contrast, thereby allowing different tissue components to be roughly differentiated (Fig. 28a and Video 5a).

This allowed us to identify vital and necrotic regions in the tumor tissue (Fig. 28b). The necrotic areas had a weaker autofluorescence signal because of lower tissue density and were therefore seen as darker regions. Conventional H&E staining was used to verify these necrotic areas of tissue (Fig. 28e,f). The erythrocytes had very high autofluorescence emission levels, distinguishing them very clearly from the surrounding tissue. This allowed us to visualize their distribution pattern and check for the presents of blood pools (Fig. 28c). Compared to conventional 2D histology where only a few slices are commonly available, UM enables whole tumor morphology analysis (Fig. 28d and Video 6a,7a).

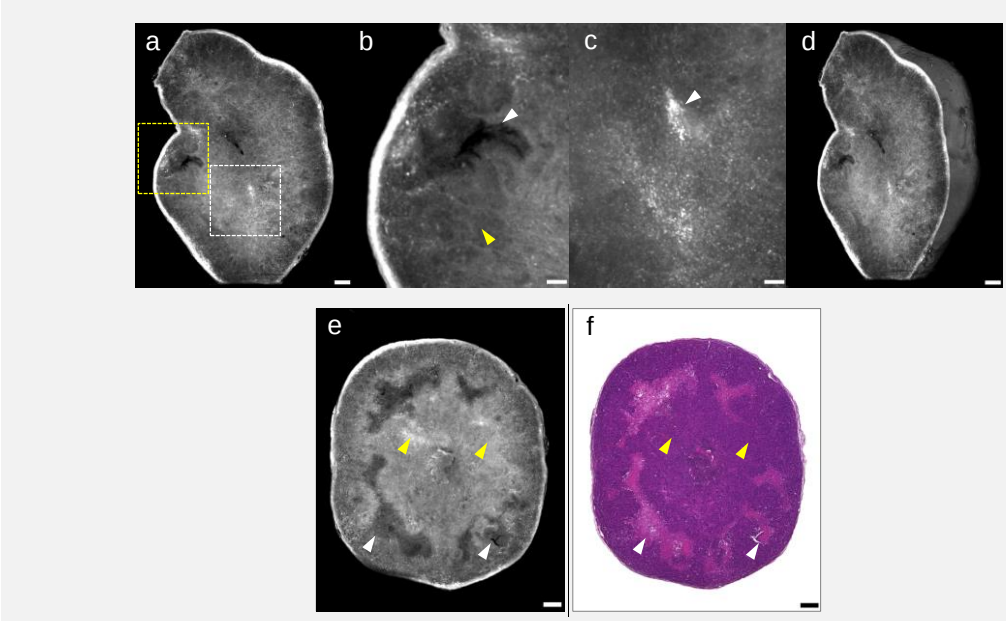

Figure 28: Visualization of tumor morphology by UM. (a) The detection of tissue autofluorescence provides detailed information about tumor morphology. (b) The strong contrast allowed us to differentiate between vital (yellow arrowhead) and necrotic (white arrow head) tumor areas. (c) Erythrocytes have a very high autofluorescence signal in this spectral range (white arrowhead). As a result of this their distribution and accumulation in the tumor tissue was clearly visible. (d) Volume rendering (VR) of the tumor morphology. (e,f) The morphological comparison of the virtual tissue slice from the UM (e) and classical H&E-staining (f) showed an excellent correlation. Both methods clearly differentiated the necrotic tissue areas (white arrowhead) from the solid tissue areas (yellow arrowhead) of the tumor. Single slice: (a-c,e,f) 5 µm diameter. Scale bar: (a,d-f) 250 µm, (b,c) 100 µm.

4.7.1.2 Visualization of tumor vessel architecture

The administrated Lectin-Alexa657 binds specifically to the sugar residues on the vascular endothelial cells and enables the three dimensional visualization of tumor vessel architecture. The high binding specificity and the fluorescent properties of the labeled Lectin resulted in a high signal-to-noise ratio (Fig. 29a and Video 5b). Employing an optimal device configuration we were able to achieve almost isotropic voxel sizes of 5.1 µm.

A maximum intensity projection (MIP) of 30 optical vascular slices clearly showed the chaotic, irregular and dramatically branched vascular structures typical of a tumor [159] (Fig. 29b and Video 6b). The heterogeneous vascular distribution in the tumor was also clearly evident; whereas some areas of the tumor displayed high vascular density (Fig. 29c), vascularization in other parts was only sparse or absent (Fig. 29d). With UM we were able to acquire the whole vascular tree of a tumor at cellular level (Fig. 29e and Video 7b,8). If it is not necessary to capture the entire vasculature of the tumor, local xy-resolutions of up to 0.5 µm can be

achieved. This allowed us to differentiate between regular blood vessels and tumor vessels (Fig. 29f) and even individual vascular endothelial cells could be clearly displayed (Fig. 29g).

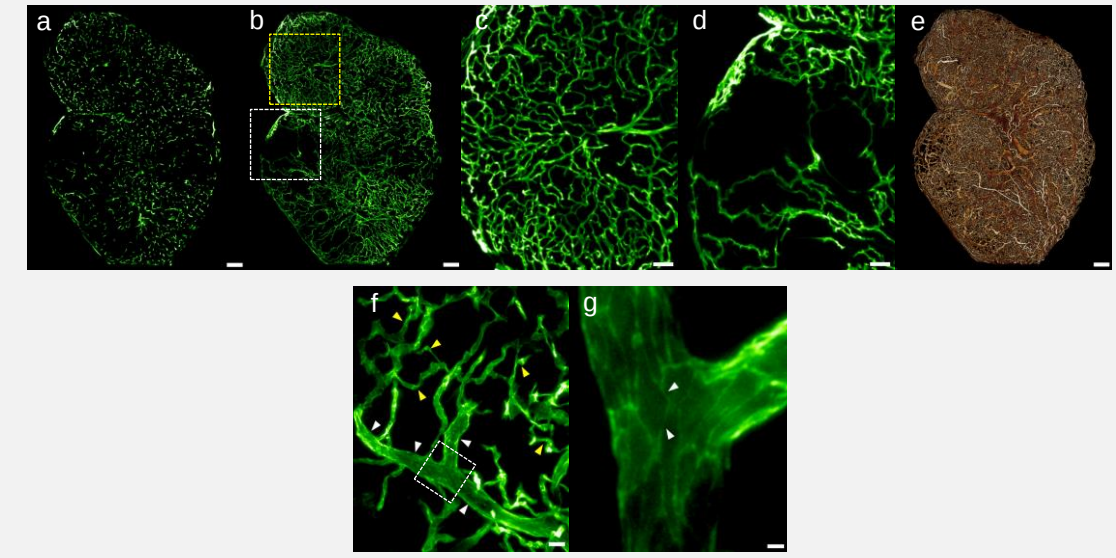

Figure 29: Visualization of tumor vessel architecture by UM. (a) The Lectin-Alexa647 labeled vessels of the KPL-4 tumor were very clearly visible in a single virtual slice with UM. (b) The complex and chaotic structures of the tumor vessels can be seen in a maximum intensity projection. (c,d) We can see in the blow-up image of the MIP from (b) the heterogeneity of the vessels. Some areas of the tumor have very dense vascularization (c), whereas vascularization in other areas is very sparse or absent (d). (e) VR of the vessel architecture. (f) If we concentrate only on smaller sections of the tumor the local xy-resolution can be increased to a value of 0.5 µm. This allowed us to visualize the morphological transition from regular (white arrowhead) to tumor vascular structures (yellow arrowhead). (g) The digital blow-up of the image data from (f) allowed even single epithelial cells on the surface of the vessels to be visualized (white arrowhead). Single slice: (a) 5 µm diameter. MIP: (b-d,f) 30 slices with 5 µm diameter/slice. (f) 5 slices with 5 µm diameter/slice. Scale bar: (a,b,e) 250 µm, (c,d) 100 µm, (e) 25 µm, (f) 5 µm.

4.7.1.3 Visualization of antibody penetration

We used the Alexa750-labeled monoclonal antibody Trastuzumab to visualize antibody penetration into the tumor. Trastuzumab has a high affinity and specificity for the extracellular domain of HER2, which is overexpressed in the KPL-4 xenograft (Fig. 30a and Video 5c). The high quantum efficiency of Alexa750 generated strong fluorescence signals and allowed short exposure times (100-400 ms/slice). The whole tumor was scanned in 10 to 20 minutes depending on its size.

A MIP of 30 optical slices showed the heterogeneous penetration and binding of the antibody after 6 hours of incubation time (Fig. 30b and Video 6c). Some areas of the tumor revealed a very strong and homogeneous Trastuzumab distribution (Fig. 30c), whereas other parts had only very low or no antibody signals (Fig. 30d). Ultramicroscopy opens up the possibility to three-dimensionally visualize drug penetration inside a whole tumor at a cellular level (Fig. 30e and Video 7c).

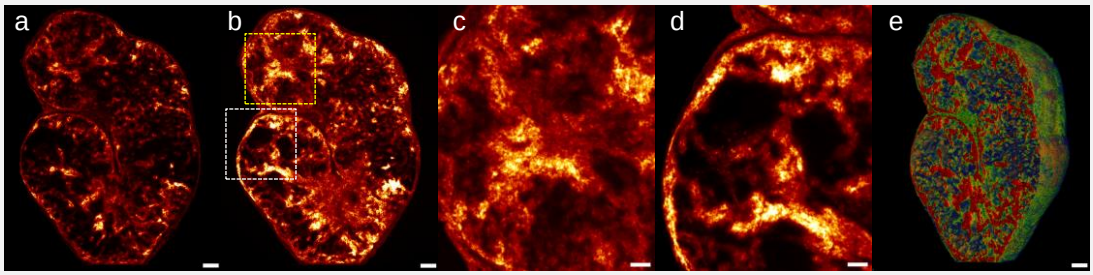

Figure 30: Visualization of therapeutic drug penetration by UM. (a,b) The penetration of Trastuzumab-Alexa750 after an incubation time of six hours was seen in both the virtual single slice (a) and in the maximum intensity projection (b). (c,d) The inhomogeneous penetration and distribution of the antibody in the tumor can be clearly visualized in the blow-up of the MIP from (b). Most parts of the tumor areas were very extensively penetrated (c), although there were also areas that had only a weak or completely absent antibody signal (d). (e) VR of the antibody penetration. Single slice: (a) 5 µm diameter. MIP: (b-d) 30 slices with 5 µm diameter/slice. Scale bar: (a,b,e) 250 µm, (c,d) 100 µm.

4.7.2 Combination of different tumor parameter

Multispectral fluorescence UM allows visualizing the penetration patterns of a labeled drug in relation to the tumor vessels (Fig. 31a and Video 9a). The relationship between the density and morphology of the vessels and the antibody penetration can clearly be seen. Highly vascularized areas of the tumor displayed very strong and homogeneous antibody distribution, whereas areas with low vascular density were only slightly or not at all penetrated (Fig. 31b,c). Morphological abnormalities or changes in the tumor tissue (such as necrosis) could also be correlated to the vascular network (Fig. 31d and Video 9b). Tissue areas with a vascular density below a certain level were apparently no longer supplied with oxygen and/or nutrients, inevitably leading to tissue necrosis (Fig. 31e). Visible accumulation of red blood cells in the tumor tissue gave us an indication of vessel permeability (Fig. 31f). The combination of tissue information with antibody penetration indicated how the drug was penetrating various tissue areas (Fig. 31g and Video 9c). We observed that Trastuzumab-alexa750, as a tumor-associated drug, generally demonstrated no or only very low penetration into necrotic areas of the tissue (Fig. 31h), whereas solid tumor tissue with sufficient vascular density had a strong antibody signal (Fig. 31i).

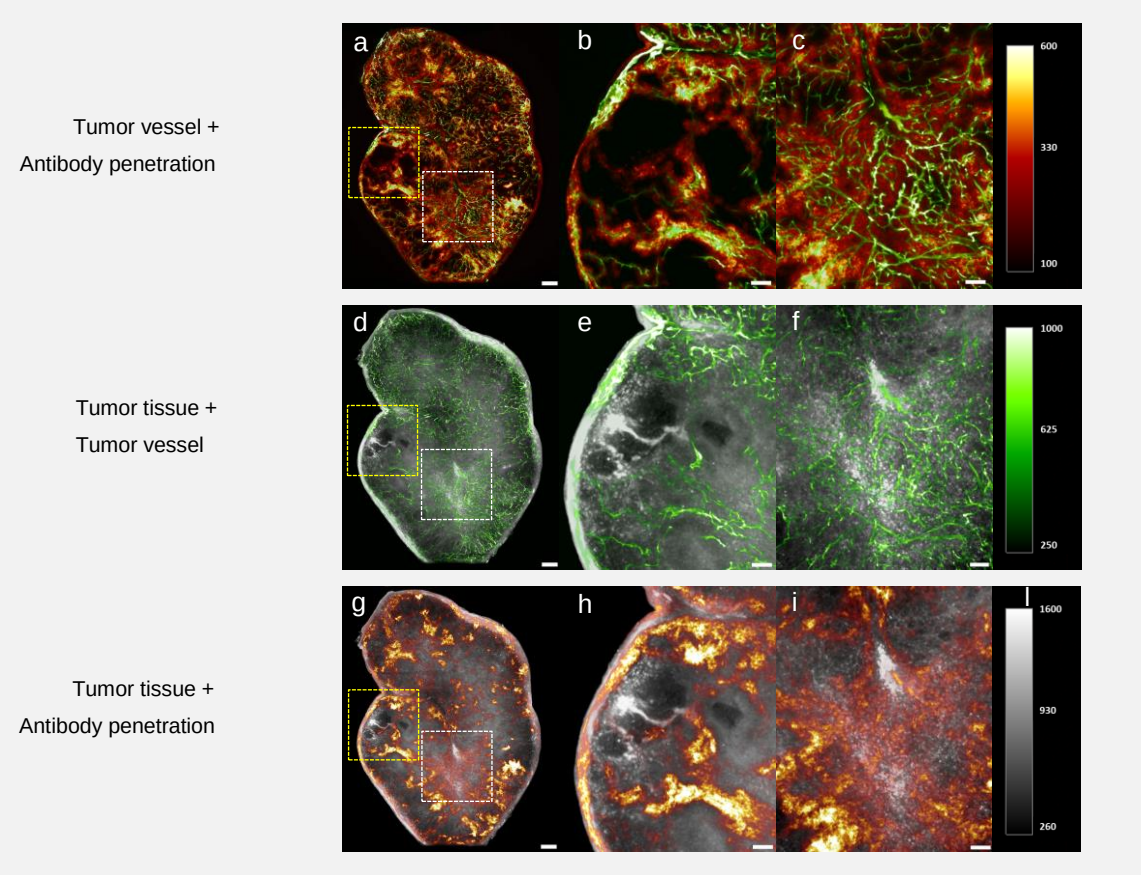

Figure 31: Combination of different tumor parameters. (a) The overlapping of the vascular and antibody channels showed that the differing density of the vessels leads to an uneven distribution of the antibody. In areas with a high vascular density there was strong and homogeneous antibody penetration (c), whereas tumor areas with low vascular density (b) showed only very slight or absent antibody signals. (d) The combination of the tissue and vascular information clearly showed the correlation between vascular density and the development of necrosis. (e) Areas with low or absent vascular connections developed necrosis, while those with a high vascular density had a solid tissue structure (f). In the latter, erythrocytes were also more prevalent. (g) The overlapping of the tissue and antibody channel showed the penetration of the antibody in the different areas of tissue. (h) Necrotic areas of the tumor were hardly penetrated by Trastuzumab at all. (i) Solid tumor tissue, on the other hand, demonstrated very strong and homogeneous antibody distribution. MIP: (a-i) 30 slices with 5 µm diameter/slice. Scale bar: (a,b,d,e,g,h) 250 µm, (c,f,i) 100 µm.

4.7.3 Validation of ultramicroscopy with immunohistochemistry

As UM was being used for the first time for multispectral tumor analysis, the virtual slices were validated using conventional histology (Fig. 32a). Therefore, the cleared KPL-4 tumor was cut after UM measurement into a series of tissue slices and different targets were then immunohistochemically stained. A direct comparison between the virtual and conventionally prepared tumor slices showed an excellent correlation. Both the tissue morphology and the vascular architecture of the tumor, and the penetration and binding of the therapeutic antibody were shown to be identically rendered with UM and classical histology (Fig. 32b-j).

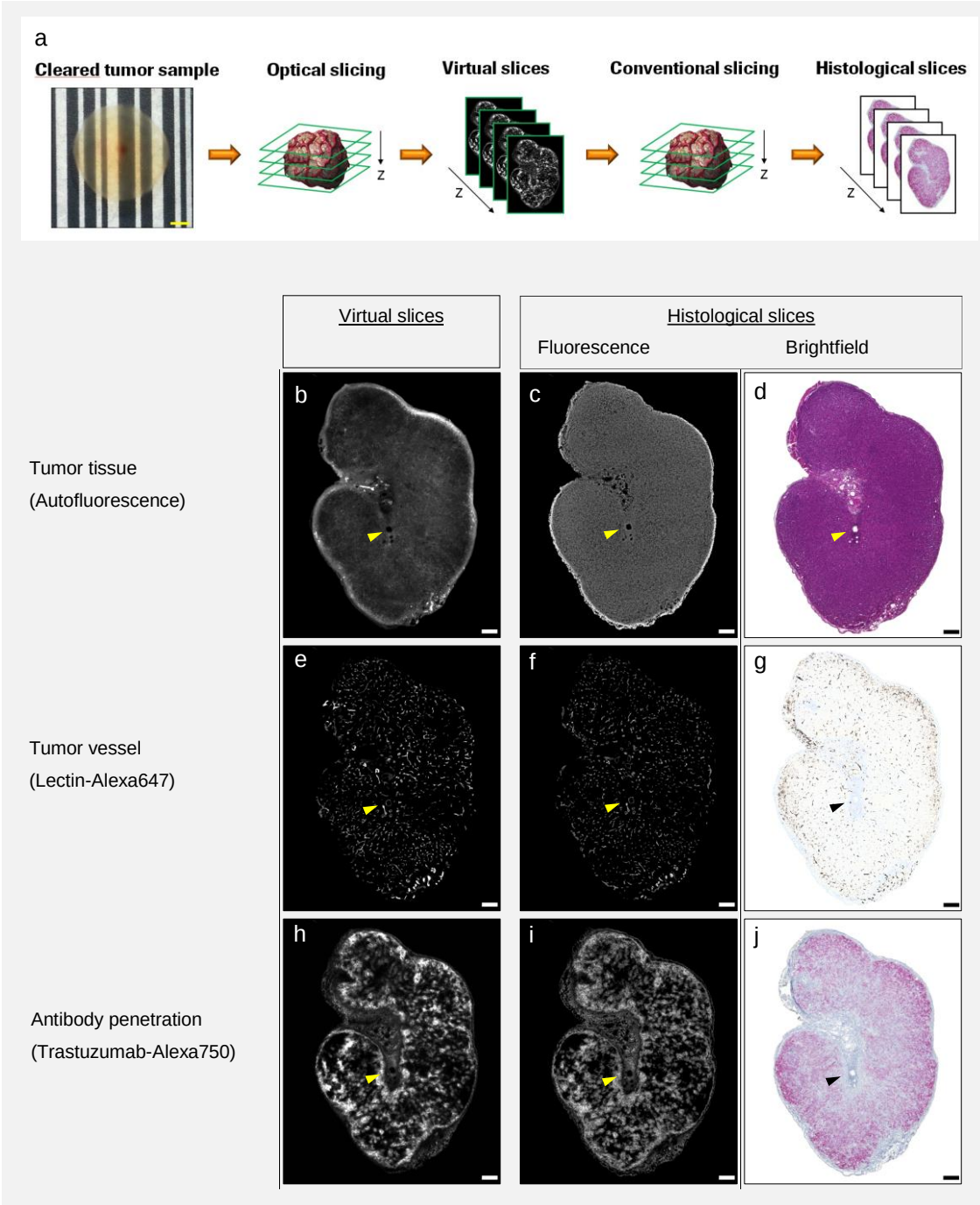

Figure 32: Validation of ultramicroscopy with immunohistochemistry. (a) The cleared sample of a KPL-4 tumor showed excellent tissue transparency, with the absorption and scattering of emission and fluorescent light reduced to a minimum. We measured the cleared sample optically in a three-dimensional process using UM and validated the resulting virtual tissue slices using conventional histology. We then cut the tumor into a series of tissue slices and immunohistochemically stained different targets and examined the structural similarities between the virtual and histological slices. Scale bar: 500 µm. (b) The virtual tissue information from the UM correlated perfectly with classical histology. The conventional DAPI (c) and H&E (d) stained serial tissue slices had a morphological tissue structure identical to that of the virtual tissue slice (b). (e) We were also able to demonstrate these structural similarities for the two-dimensional vascular architecture. Both the conventional fluorescence slice of the vessels (f) and the tissue slice stained with anti-CD34-DAB (g) were homologous in their vascular structure to the virtual single slice from the UM (e). (h) The penetration and binding pattern of trastuzumab-alexa750 is also virtually identical. The distribution pattern of the virtual (h) and the conventional fluorescence slice (i) is almost identical. The immunohistochemical staining of the extracellular HER2-receptors (j) also demonstrated the same distribution pattern as virtual UM. Single slices: 5 µm diameter. Scale bar: 250 µm.

4.7.4 Development of quantification software

The prior evaluation study demonstrated in a very impressive way the great potential of ultramicroscopy for three-dimension visualization of multiple tumor parameters and further showed the perfect correlation between the virtual UM slices and conventional histology. To quantify those 3D tumor data, a novel set of custom-developed image analysis algorithms were developed and implemented into a quantification software. The analysis of the UM raw data was performed fully automatically without any manual user interference. The first step was a segmentation of the tumor sample from the background using automatic thresholding techniques on the autofluorescence channel (Fig. 33a,b). The software then generated a binary image of the vessels inside the tissue region. Vessel-free areas inside the tumor with a minimum distance to the surrounding vasculature were classified as necrotic tissue (Fig. 34). This parameter was determined based on the results of conventional histology and enabled the three-dimensional quantification of tumor necrosis (Fig. 33c,d). The next step was the skeletonization of the binary vascular tree using an iterative 3D-thinning algorithm [241].

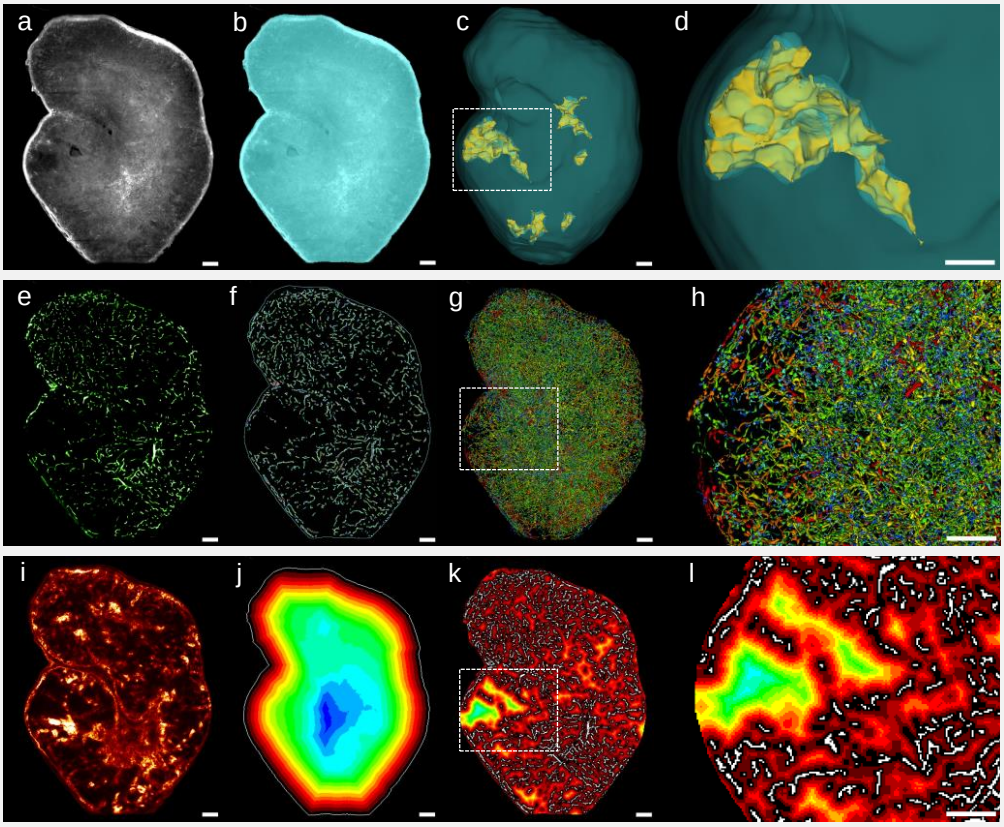

Figure 33: Quantification of ultramicroscopy data sets. (a) The raw data from the tissue channel was used to determine the total tumor volume (b) Segmentation between tissue and background (c,d) Three-dimensional visualization of the tumor volume (blue) and its necrotic areas (yellow). (e) The virtual tissue slices formed the basis of the vascular analysis. (f) Three-dimensional segmentation of the binary vascular tree. (g,h) Growth of the skeletal segments and quantification of the different segments and branching points. The different diameters of the vascular segments are represented by different colors. (i) The information from the antibody channel is used to determine the total signal and penetration of trastuzumab-alexa750. (j) We used the color-coded segmented 3D distance map shown here to calculate the penetration of the antibody from the tumor margin to its center. (k,l) We used another color-coded 3D distance map to calculate the penetration of the antibody from the tumor vessels into the surrounding tissue. Single slice: (a,b,e,f,i,j,k,l) 5 µm diameter. Scale bar: 250 µm.

Afterwards, a 3D-kernel found the branch points and segments (Fig. 33e,f). The individual skeleton segments were then extended back to the full vessel diameter using a pixel based object growing algorithm which ensured that the enlarged segments were connected to each other only by their branch points. Multiple single segment parameters and aggregate vessel statistics were then calculated for the whole tumor. This allowed the color-coded three-dimensional visualization of different vessel features, for example segment diameter (Fig. 33g,h).

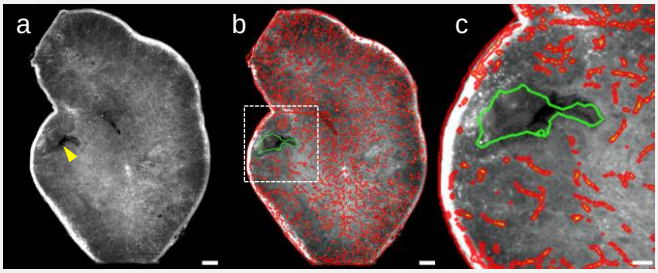

Figure 34: Detection of necrotic areas. (a,b) A binary image of the segmented vessels (b, red) was overlaid on the tissue channel from the UM (a). We classified tumor areas with no vessels and a minimum distance of 200 µm to the surrounding vasculature as necrotic (b, green). We then used a growing strategy to extent those areas up to a minimum vascular distance of 125 µm (b,c). Scale bar: (a,b) 250 µm, (c) 100 µm.

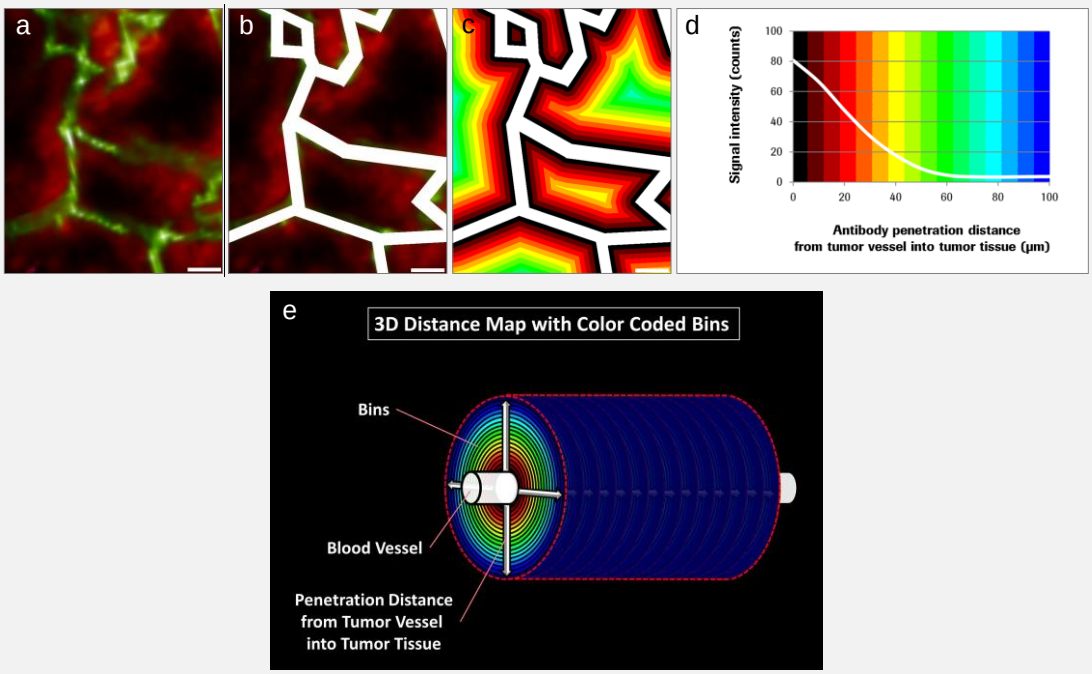

Figure 35: Quantification of drug penetration. (**a**) We combined the UM information from the vessel (green) and the antibody channel (red) to determine the antibody penetration from the tumor vessels into the surrounding tissue. After detection of the vessels (**b**) we created a distance map and divided it into individual bins (**c**). Here they are displayed color-coded to allow easy visual differentiation (color map form black to blue). (**d**) We then calculated the antibody signal in the various bins. The resulting signal intensity gradient reflects antibody penetration from the tumor vessels into the surrounding tumor tissue (**e**). The analysis of antibody penetration from the margin of the tumor to its center follows the same principles. MIP: (**a-c**) 30 slices with 5 µm diameter/slice. Scale bar: 50 µm.

To determine the penetration behavior of a fluorescence-labeled substance (e.g. Trastuzumab-alexa750) into the tumor tissue the software initially subtracted the computed background signal from the raw data. It then calculated the accumulated antibody signal and the average signal intensity of trastuzumab-alexa750 in the entire tumor area (Fig. 33i). Furthermore, the software analyzed the distribution pattern of the fluorescence signals within the sample. For this, it calculated three-dimensional distance maps to the tumor border and the nearest vessel and then segmented these into different color-coded bins (Fig. 33j-l).Thereafter, the antibody signal intensities were quantified in every bin, resulting in penetration gradients of the antibody (Fig. 35). This process allowed the analyze of the antibody penetration behavior from the tumor margins to its center (Fig. 33j) and the penetration behavior of the therapeutic drug from the vessels into the surrounding tumor tissue (Fig. 33k,l). Further information regarding the quantification software and hardware components are available in section 3.2.10.2.

4.7.5 Imaging of anti-angiogenic treatment effect and drug penetration

4.7.5.1 Monitoring of anti-angiogenic treatment response

To reveal the therapeutic effect of an anti-angiogenic compound by means of UM, we conducted a preclinical study on KPL-4 tumor bearing mice. The treatment group received a single dose of the monoclonal antibody Bevacizumab, which binds specifically to the human vascular endothelial growth factor (hVEGF). Control mice with the same tumor preparation were treated with an adequate amount of phosphate buffered saline (PBS). After 1, 3 and 7 days we selected 5 animals from both groups and injected Trastuzumab-Alexa750. Six hours later, Lectin-Alexa647 was applied to tag the tumor vessels. Subsequently, we scanned the explanted and cleared tumor samples using multispectral fluorescence UM.

The tumor vessels in the control group showed a chaotic and inhomogeneous vascular distribution throughout. Large sections of the tumor periphery appeared to be highly vascular, whereas some areas of the tumor had only isolated vessels, and others were completely devoid of vascularization (Fig. 36a). We observed a therapeutic effect of Bevacizumab on the tumor vessels after only one day of treatment [159] (Fig. 36b). At this point the therapy led to a significant reduction of the vessel volume (P = 0.01), number of vessel segments (P = 0.01), and branching points (P = 0.01) in the tumor periphery, whereas these parameters remained virtually unchanged in the center of the tumor (Fig. 36d-f).

The treatment also normalized and homogenized the vessel architecture [242] (Fig. 36b). This reduction and normalization effect became more pronounced as the length of treatment increased (Fig. 36d-f). We observed the main therapeutic effect on vascular segments with a diameter between 10 and 30 µm. Smaller vessels were not significantly affected by the therapy (Fig. 37). The normalized vessel network obviously allowed an improved blood supply to the tumor, reduced the interstitial fluid pressure (IFP) [243], and therefore provided a more constant supply of oxygen and nutrients [159]. This effect led to an evenly distributed proliferation of the tumor cells and after seven days the necrotic tissue areas were reduced by an average of 69% (Fig. 36c, Fig. 38). Even after seven days of treatment, we observed no significant reduction in the tumor volume (Fig. 36c).

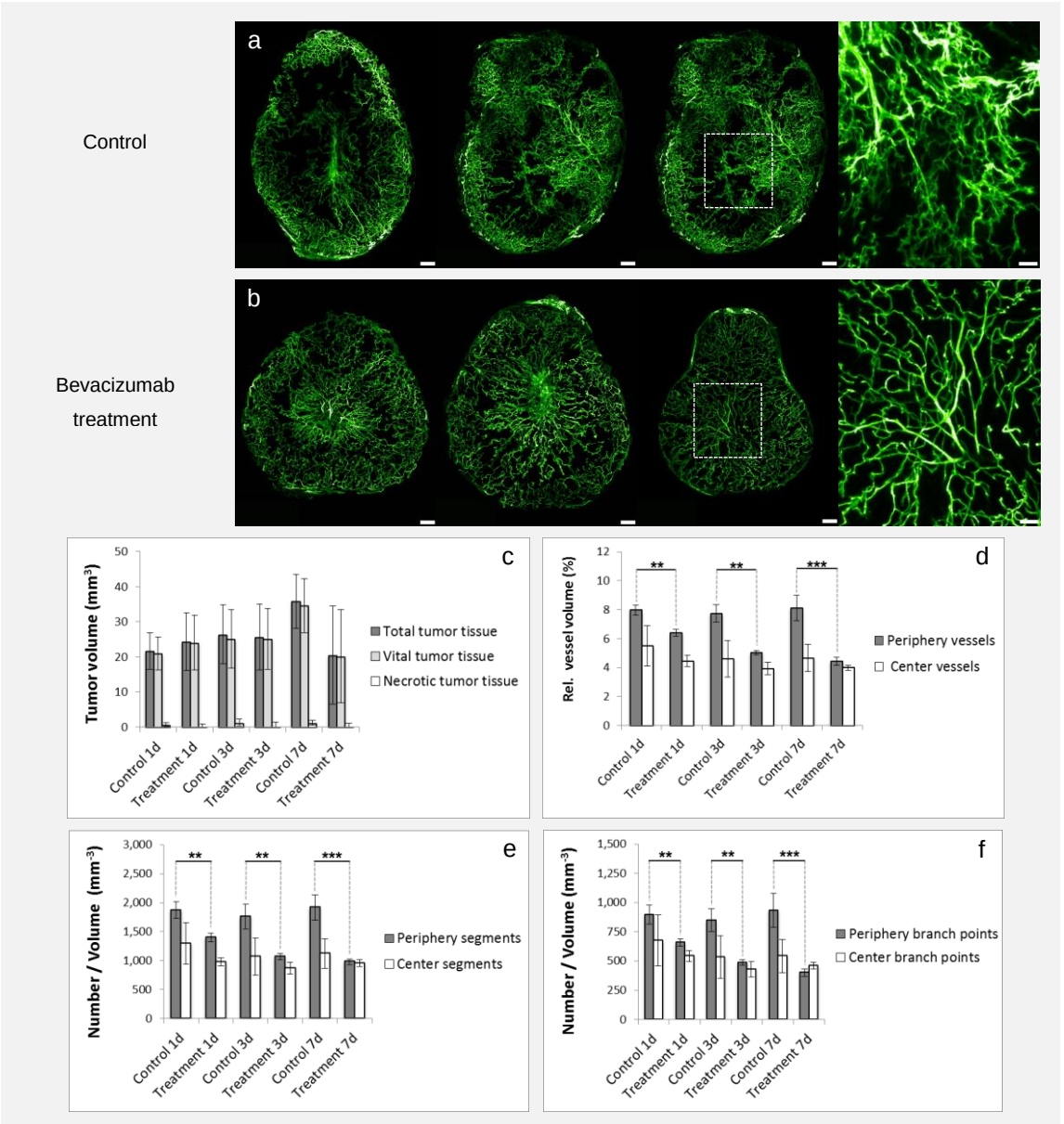

Figure 36: Monitoring of anti-angiogenic treatment response. (a,b) We visualized the vascular development of KPL-4 tumors in the control group for a period of seven days using UM. Treatment with Bevacizumab reduced and normalized the vessels in the tumor; the effect was proportional to the length of treatment (day 1, 3 and 7; n=5 mice/day). MIP: 60 slices with 5 µm diameter/slice. Scale bar: 250 µm, 100 µm (blow-up). (c) Quantification results of the total, vital, and necrotic tumor tissue volume for the control and treatment group at different time points. Even after seven days of treatment there was no significant reduction in tumor volume. (d-f) The quantification of the preclinical treatment study showed a reduction in vascular volume (d), vascular segments (e) and branching points (f) in the tumor periphery, whereas these parameters remained virtually unchanged in the core of the tumor [% = (tumor vessel vol./total tumor tissue vol.)*100]. Control group: day 1, 3 and 7; n=5 mice/day. Treatment group: day 1, 3 and 7; n=5 mice/day. All values are given as mean ± s.d.. **P* < 0.05, ***P* < 0.01, ****P* < 0.001, *t*-test.

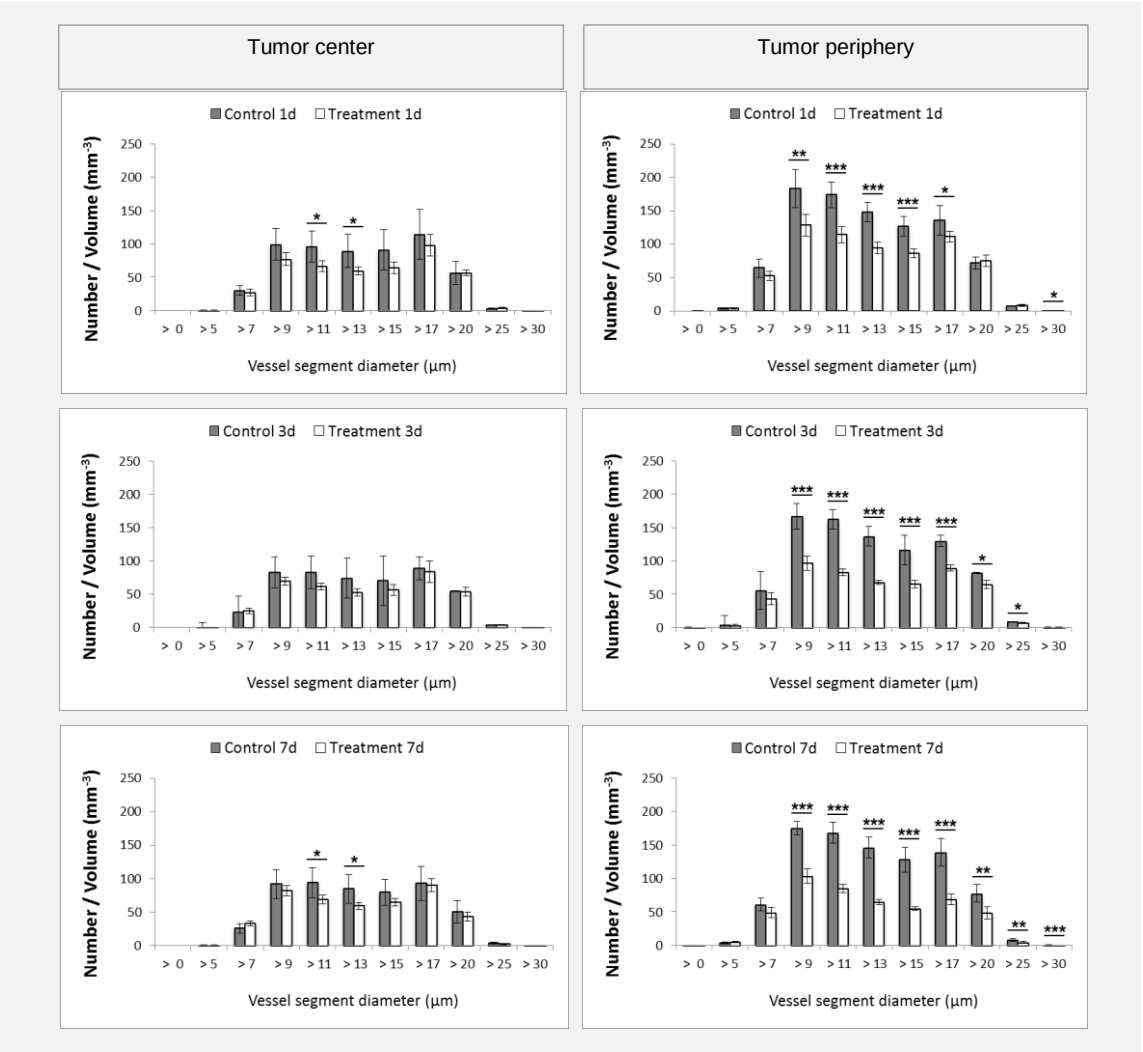

Figure 37: Visualization of vessel segment diameter distribution. The different diagrams show the diameter distribution of the vascular segments in the tumor center (left row) and in the tumor periphery (right row) of the control and treatment groups. Treatment with Bevacizumab led primarily to a significant reduction in the number of segments located inside the tumor periphery (right row), whereas the effect in the tumor center was only marginal (left row). Control group: day 1, 3 and 7; n=5 mice/day. Treatment group: day 1, 3 and 7; n=5 mice/day. Values are given as mean values ± s.d..*$P < 0.05$, **$P < 0.01$, ***$P < 0.001$; *t*-test.

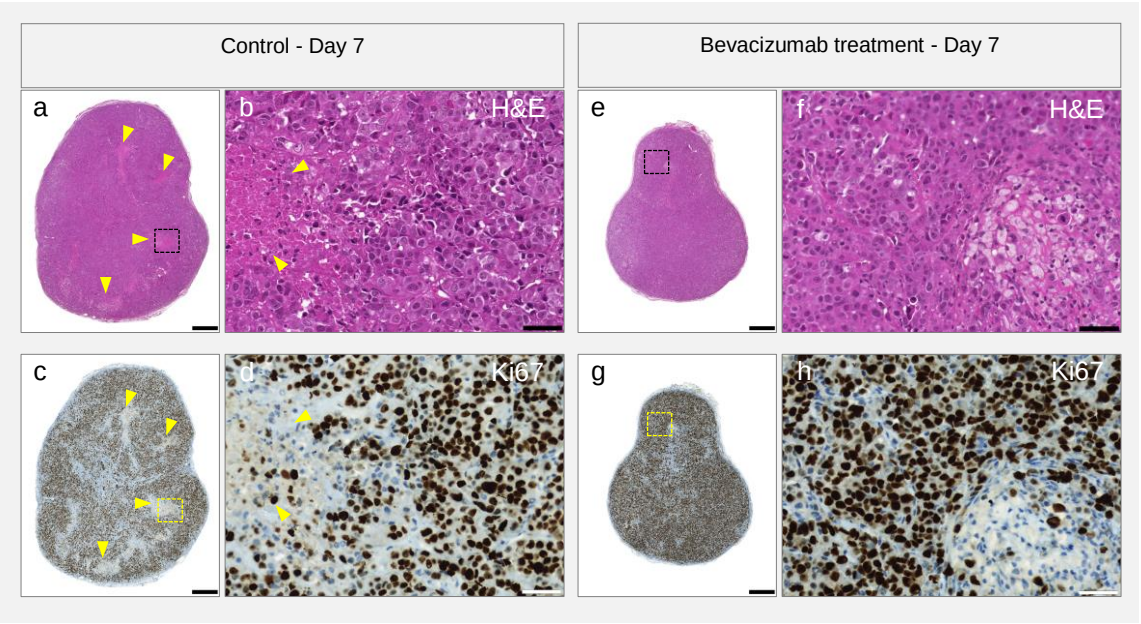

Figure 38: Treatment effect of Bevacizumab on tumor cell proliferation and necrosis. Histological comparison of the tumor morphology (H&E staining, a-d) and tumor cell proliferation (Ki67 staining, e-h) in the control and Bevacizumab treated group on day 7. (a-d) Both IHC stains of the control group revealed large areas of necrosis (yellow arrowhead) in the tumor tissue of the control group. (e-h) As opposed to this the Bevacizumab treated tumors showed a reduction of the necrotic areas. Up to this point the treatment had no clear effect on the tumor cells proliferation rate. Thus, the Ki67 staining (brown tumor cells) in the solid tissue areas in both study groups showed a very strong and homogeneous proliferation pattern. Single slices: 5 µm diameter. Scale bar: 250 µm, 50 µm (blow-up).

4.7.5.2 Drug penetration after anti-angiogenic pre-treatment

Besides analyzing the direct therapeutic effect of Bevacizumab on the vascular architecture and the tumor volume, we also investigated the influence of an anti-angiogenic pre-treatment on the penetration of the antibody trastuzumab-alexa750. Therefore, we combined the UM information of tumor vasculature from the previous chapter with the Trastuzumab-Alexa750 tumor penetration. Mice treated with PBS demonstrated a strong penetration of Trastuzumab-Alexa750 in highly vascularized tumor areas (Fig. 39a). In contrast, explanted tumors from mice pre-treated with Bevacizumab showed a significant reduction in the Trastuzumab-Alexa750 penetration (P = 0.001) after just one day of treatment (Fig. 39b). Furthermore, the anti-angiogenic therapy significantly decreased the penetration behavior of Trastuzumab from the tumor border to its center (Fig. 39d,e) and also the penetration from the tumor vessels into the surrounding tumor tissue (Fig. 39f,g). To ensure that the anti-angiogenic therapy carried out did not affect the HER2 expression level, we performed IHC staining on tumor tissue sections. Both study groups demonstrated high extracellular HER2 expression (3+) on the surface of the KPL-4 tumor cells (Fig. 40), and thus we were able to rule out an internalization and/or shedding of the extracellular domains (ECD) from the tumor cell surface. Therefore, the diminished penetration of Trastuzumab-Alexa750 can consequently only be attributed to the attendance of Bevacizumab within the tumor and the reduction in vascular permeability resulting from vascular normalization [150]. The reduced pore size in the normalized tumor vessels made it more difficult for Trastuzumab-Alexa750 to penetrate, due to its high molecular weight, and as a result more of it remained in the mainly vessels [244] (Fig. 41).

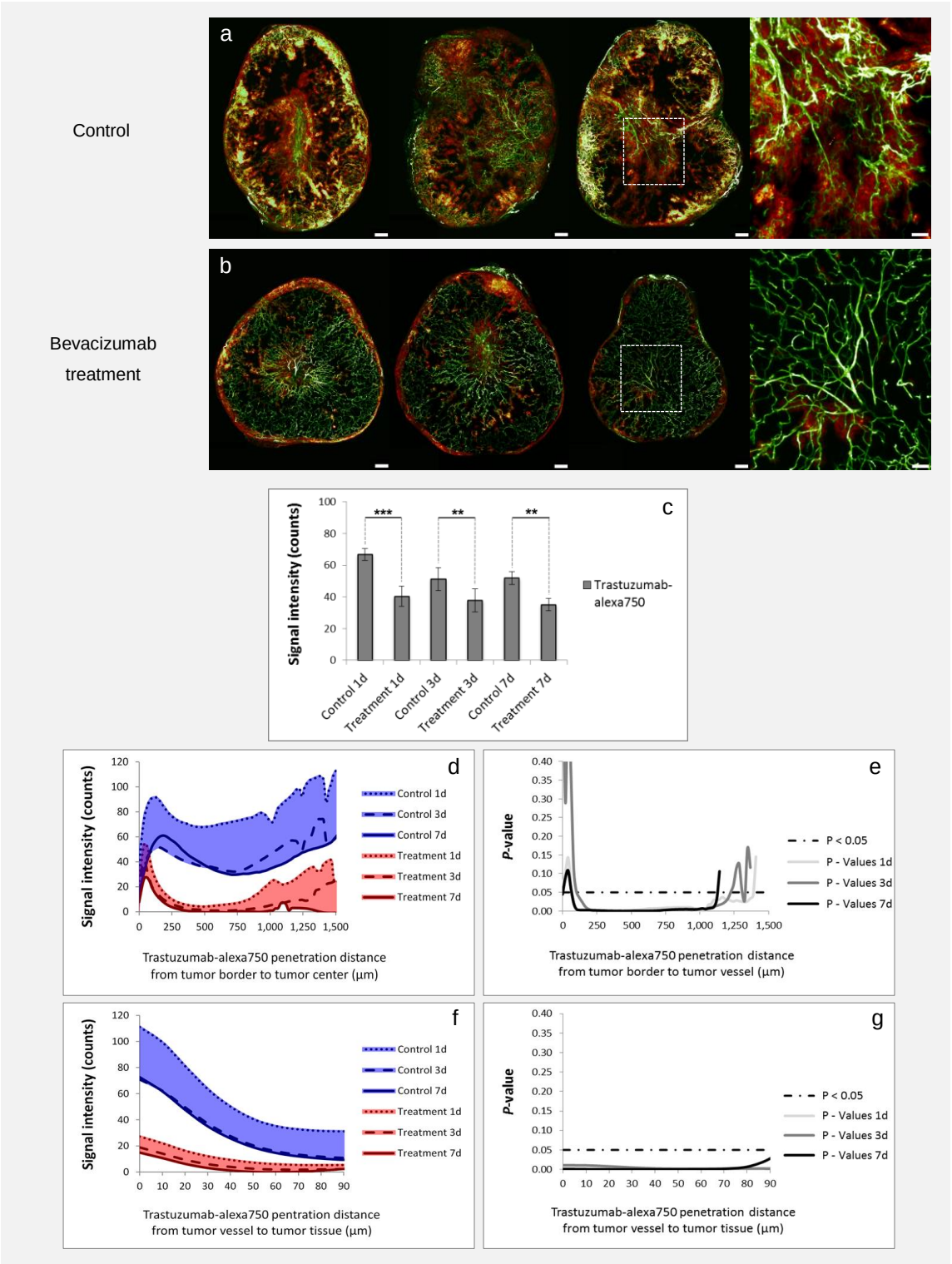

Figure 39: Monitoring of antibody penetration after anti-angiogenic pre-treatment. (a, b) The control group showed a strong penetration behavior of Trastuzumab-alexa750 in the KPL-4 xenograft (a), whereas the labeled Trastuzumab penetration was significantly reduced by anti-angiogenic pre-treatment with Bevacizumab (b). MIP: 60 slices with 5 µm diameter/slice. Scale bar: 250 µm, 100 µm (blow-up). (c-e) Pre-treatment with Bevacizumab led to a significant reduction in Trastuzumab-alexa750 penetration (c). This was seen in both the reduced penetration of Trastuzumab-alexa750 from the tumor border to its center (d, e) and in the reduced labeled Trastuzumab penetration from the tumor vessels into the surrounding tumor tissue (f, g). Control group: blue color; mean of day 1, 3 and 7; n=5 mice/day. Treatment group: red color; mean of day 1, 3 and 7; n=5 mice/day. All values are given as mean ± s.d.. *P < 0.05, **P < 0.01, ***P < 0.001, t-test.

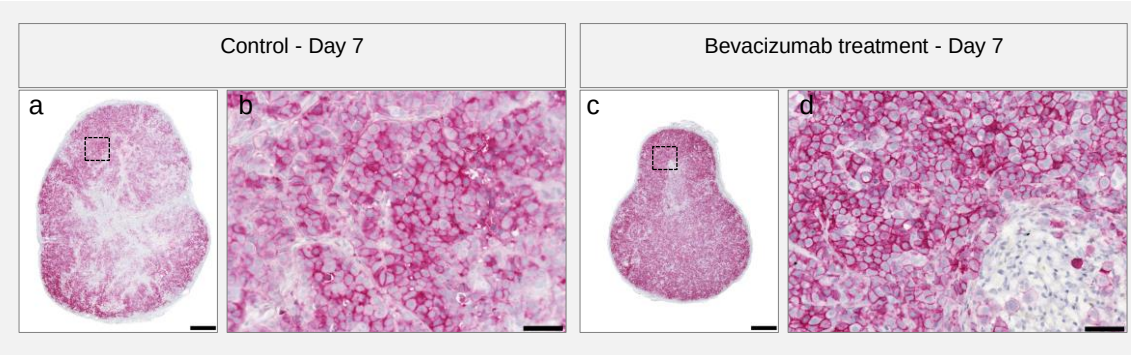

Figure 40: Visualization of extracellular HER2 receptor expression. The immunohistological comparison of the HER2 receptor status of the control (a,b) and treatment groups (c,d) on day 7 showed no significant difference in the expression pattern of the extracellular receptor domains. Bevacizumab treatment therefore does not at this time point have any direct effect on the HER2 receptor. Single slices: 5 µm diameter. Scale bar: 250 µm, 50 µm (blow-up)

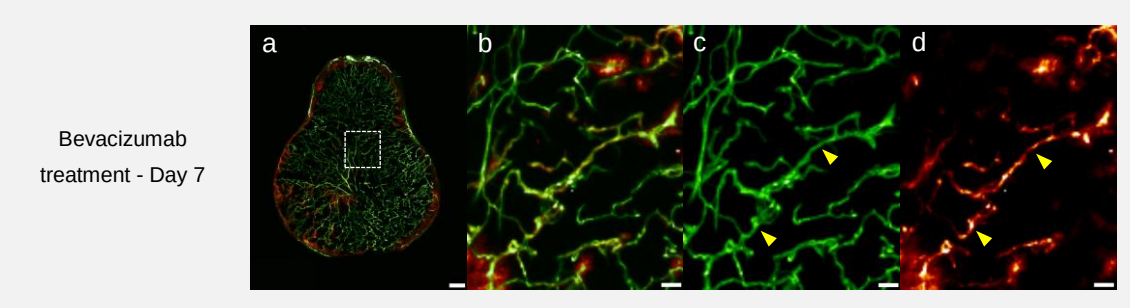

Figure 41: Penetration behavior of Trastuzumab-Alexa750 after Bevacizumab pre-treatment. (a) The seven-day treatment with Bevacizumab led to a reduction, normalization and homogenization of vascular architecture (green) and significantly reduced Trastuzumab-Alexa750 (red) penetration. (b) The blow-up of (a) clearly shows the reduced penetration of Trastuzumab-Alexa750 from the tumor vessels. In the spectral decomposition of the image from (b) into the vessel (c) and antibody channel (d) higher levels of residual Trastuzumab-Alexa750 (yellow arrowhead) were detected in the normalized tumor vessels. MIP: (a-d) 60 slices with 5 µm diameter/slice. Scale bar: (a) 250 µm, (b-d) 100 µm.

4.7.6 Visualization of different mouse organs

The great advantages of UM in the three-dimensional visualization and automatic analysis of tumor tissue was proved in an impressive way in the prior sections. Beside the evaluation and validation of multispectral fluorescence ultramicroscopy on xenograft tumors, other organs of the mouse were analyzed with this imaging technique as well. Therefore, a tumor-free SHO mouse was intravenously injected with Lectin-Alexa647 and after an incubation period of 3 minutes, different organs were extracted. Subsequently, the tissue was fixed in formalin, optically cleared and measured via ultramicroscopy. The results displayed in the following sections, give excellent insight in the anatomical structure of the different mouse organs.

4.7.6.1 Morphological visualization of the murine lymph node

Through measuring the tissue autofluorescence via UM, the basic morphological structures of the lymph node could be visualized (Fig. 42a). The single bright spots in the lymph node tissue displayed circulating erythrocytes. The vascular of the lymph node was also excellently visible in the single virtual slices (Fig. 42b), but the complexity and high branching of the vessel network only appeared in the MIP and VR (Fig. 42c,d).

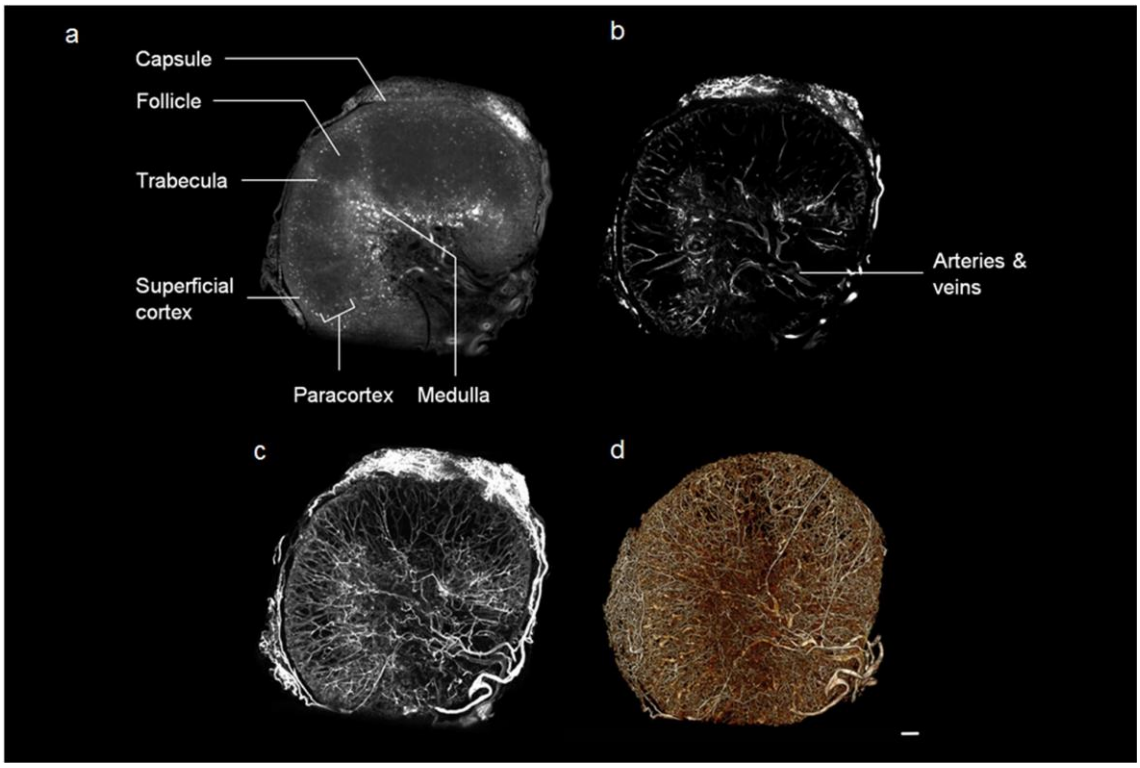

Figure 42: Morphological visualization of the mouse lymph node by UM. (a) The tissue autofluorescence signal was used to determine morphological features of the lymph node. (b) Lectin-Alexa647 bind strongly to the vessels and visualized perfectly the vessel architecture in a single slice. (c) MIP showed the complex vessel architecture. (d) Volume rendering of the entire vessel network. Magnification: 3.2 x 2.0. Single slice: (a-b) 5 µm diameter. MIP: (c) 50 slices with 5 µm diameter/slice. VR: (c) 285 slices with 5 µm diameter/slice. Scale bar: (a,b,c,d) 100 µm.

4.7.6.2 Morphological visualization of the murine kidney

During the clearing of the non-perfused mouse kidney, no ideal tissue transparency could be achieved due to high erythrocyte concentration in the organ. Thus, strong absorption and light scattering artifacts occurred during the measurement in the autofluorescence channel, which resulted in inhomogeneous illumination of the tissue and poor image quality. Only the NIR excitation light for the visualization of Lectin-Alexa647 could illuminate the different measurement planes of the kidney tissue in a complete and consistent way. Through this, a perfect image of the vessel architecture, as well as morphological information about the kidney structure could be detected (Fig. 43).

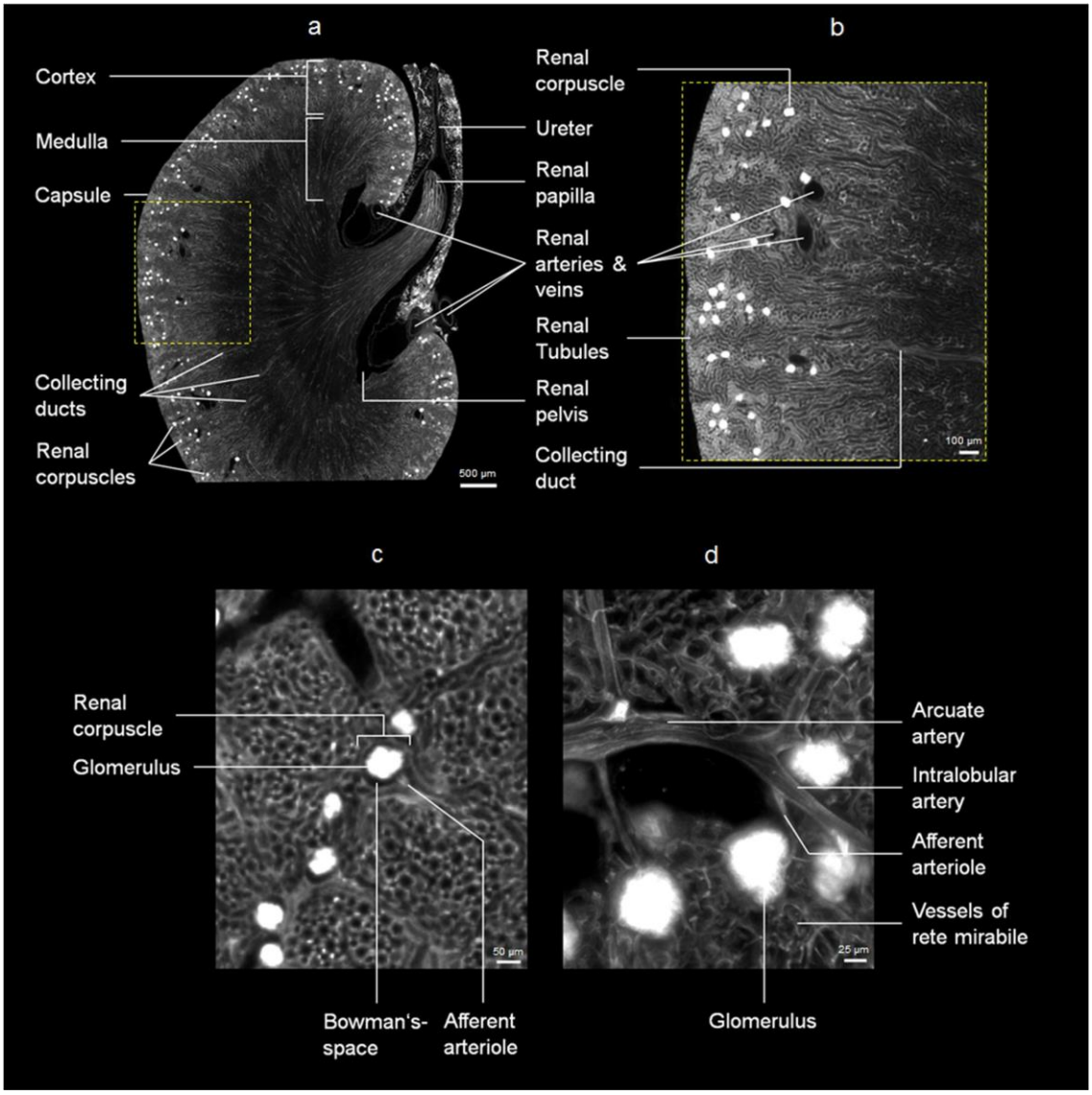

Figure 43: Morphological visualization of the mouse kidney by UM. (a-d) The Lectin-Alexa647 staining provided detailed information about vessel architecture and different morphological structures of the mouse kidney. Magnification: (a-c) 0.64, (d) 1.2. Single slice: (a-c) 5 µm diameter. MIP: (d) 80 slices with 5 µm diameter slice. Scale bar: (a) 500 µm, (b) 100 µm. (c) 50 µm. (d) 25 µm.

4.7.6.3 Morphological visualization of the murine eye

The use of UM for the three-dimensional visualization of the eye structure is a suitable alternative to conventional imaging methods. Measuring the tissue autofluorescence could detect and display the eye morphology in great detail (Fig. 44a,b). All basic eye structures were clearly visible and correlated nicely to classic H&E staining [245]. Moreover the vessel network of the eye could also be visualized by detecting Lectin-Alexa647. (Fig. 44c,d). In the following VR, especially the complex vessel structure of the retina was brilliantly visible (Fig. 44e-g).

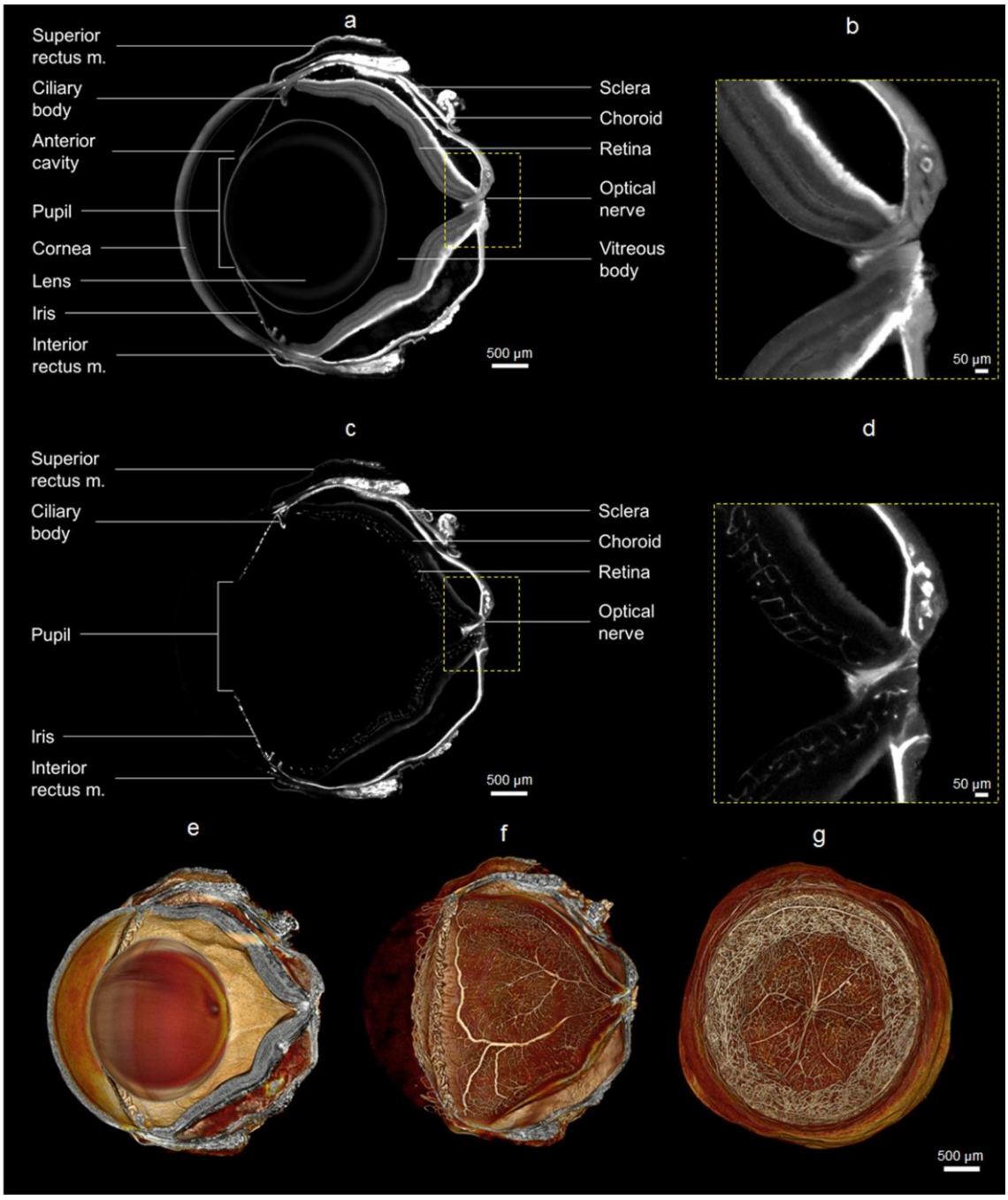

Figure 44: Morphological visualization of the mouse eye by UM. (a,b) The tissue autofluorescence signal was used to determine detailed morphological features of the eye. (c,d) Lectin-Alexa647 bind strongly to the vessels and visualized perfectly the vessel architecture of the eye. (e,f,g) VR of the tissue and vessel channel showed in detail the complex morphological structures of the eye. Magnification: 0.64. Single slice: (a-d) 5 µm diameter. VR: (e,f) 250 slices with 5 µm diameter/slice, (g) 530 slices with 5 µm diameter/slice. Scale bar: (a,c,e-g) 500 µm, (b,d) 50 µm.

5 Discussion

The present work is dedicated to improve standard procedures in preclinical drug development, such as conventional IHC and blood sampling, by using *in vivo* and *ex vivo* fluorescence imaging modalities. These fluorescent based methods were used to determine relevant parameters for the preclinical antibody development especially as: the evaluation of tumor cell receptor expression, epitope mapping, and binding specificity of monoclonal antibodies. Furthermore, these modalities were used for the identification and selection of the most suitable xenograft model, the determination of the optimal treatment (dosage and application time) for a preclinical efficacy study, and also for the non-invasive measurement of pharmacokinetic parameters through the eye of experimental animals. In addition to this, multispectral fluorescence ultramicroscopy was evaluated and validated for the three-dimensional visualization and automatic quantification of optical transparent tumor samples at cellular resolution.

Problems of tumor cell receptor evaluation using IHC

It has been shown recently by Kaoru Hashizume and colleagues for anti-HER2 antibodies in human breast carcinomas [222], that the methods of tumor tissue fixation and antigen retrieval and the problems of differential reactivity of detection antibodies and the resultant receptor staining variability, have a strong influence on the quality and validity of the staining results. Therefore, it was verified if these problems play also a relevant role for the tumor cell receptor evaluation in xenograft tumor tissue. Therefore, four different anti-HER2 detection antibodies (4B5, M15, ICR55 and SP3) were used with the same staining protocol to determine the HER2 receptor status in the HER2 overexpressing NSCLC Calu-3 xenograft model (see 4.1.1.1.) The staining results demonstrated variable expression levels of the HER2 receptor, whereas two antibody formats (4B5 and M15) showed no specific receptor staining (Fig. 2a,b). One detection antibody (ICR55) displayed a specific binding to the tumor cells as well as a cross reaction with the murine stroma tissue (Fig. 2c). Only the staining with the anti-HER2 antibody SP3 gave a positive staining result and displayed the HER2 receptor status in Calu-3 tissue correctly (Fig. 2d).

In a further experiment, the influence of three different antigen retrieval buffer (citrate, rodent decloaker and rodent decloaker + fast enzyme) on the HER2 staining was assessed by using the anti-HER2 detection antibody SP3 in Calu-3 tissue slices (see 4.1.1.2). The results showed a strong influence of the antigen retrieval buffer on the HER2 receptor staining ranging from no staining (citrate buffer, Fig. 3a), to slight HER2 expression (rodent decloaker, Fig. 3b), up to strong HER2 staining results (rodent decloaker + fast enzyme, Fig. 3c). Furthermore, the direct comparison of two anti-HER2 detection antibodies (SP3 and 4B5) in combination with two different antigen retrieval buffer gave contrary HER2 receptor staining results (see 4.1.1.2). Antigen retrieval with citrate buffer resulted in a positive HER2 receptor staining result for the anti-HER2 mab / 4B5 (Fig. 4b) and in a negative staining for the anti-HER2 mab / SP3 (Fig. 4a). Changing the antigen retrieval to rodent decloaker + fast enzyme, inverted the prior HER2 staining results (pos. SP3 staining [Fig. 4d] and neg. 4B5 staining [Fig 4c]).

These results clearly demonstrated for Calu-3 xenograft model, that the determination of the tumor cell receptor status in preclinical tissue samples depends strongly on the detection antibody selected and the appropriated antigen retrieval method. Both aspects have a strong influence on the accurate determination of the tumor associated antigen on the cell surface, the selection of the most suitable xenograft model for a preclinical efficacy study and therefore may also affect the therapeutic outcome. Even if the tumor cell receptor status of a xenograft model was correctly evaluated by conventional IHC staining using non-therapeutic, paraffin-penetrating detection antibodies, there is no information available regarding the affinity and binding behavior of the therapeutic agent to the tumor cell receptor. Thus, strong overexpression of a tumor associated cell surface antigen is a major aspect for the successful selection of a suitable xenograft model, but there is no certainty for a therapeutic treatment effect.

The most straight forward procedure to efficiently combine the tumor cell receptor overexpression with a high probability for therapeutic treatment effects is the direct visualization of interaction and binding of the therapeutic antibody to the relevant tumor target. This can be accomplished in a very efficient and elegant fashion by using fluorescent labeled antibodies. The application of *in vivo* fluorescence whole-body imaging enables the non-invasive monitoring of distribution, penetration, and accumulation of the labeled compound into the tumor region. The subsequent *ex vivo* fluorescence analysis of histological tumor section permits the possibility to determine specific antibody-receptor binding. This "*in vivo* histology" method is closer orientated to the preclinical reality, since the binding of the labeled therapeutic antibody is monitored in its "natural" environment, and should therefore provide a much better forecast about the preclinical efficacy outcome.

Direct comparison of IHC and fluorescence imaging for tumor cell receptor evaluation

To substantiate the prior assumption with reliable facts, the expression level of four different tumor cell receptors (HER1, HER2, HER3 and IGF1R) of the previous Calu-3 xenograft model was evaluated by conventional immunohistochemical staining (see 4.1.2) and fluorescent *in vivo* and *ex* vivo imaging (see 4.1.3). The fluorescence imaging experiment was performed with different Cy5 labeled therapeutic antibodies which possess a high specificity for a single tumor cell receptor, including: Cetuximab-Cy5 (anti-HER1), Trastuzumab-Cy5 (anti-HER2), anti-HER3-Cy5, and anti-IGF1R-Cy5. The last two antibody formats were already under preclinical evaluation and not in clinical use. The anti-human IgE specific therapeutic antibody Omalizumab-Cy5 possesses no binding specificity to a relevant mouse target and therefore served as a negative control.

Based on conventional IHC staining results, the tumor cell antigens HER2, HER3, and IGF1R were prioritized as potential target structures for a preclinical efficacy study (Fig. 5). In contrast to the IHC staining results, only Trastuzumab-Cy5 showed a strong *in vivo* fluorescence signal in the tumor region (Fig. 6d,f). The *ex vivo* imaging results indicated a strong localization of Omalizumab-Cy5 and anti-IGF1R-Cy5 only in the stroma tissue and had no specific antibody binding to the tumor cells. Furthermore, Cetuximab-Cy5 and anti-HER3-Cy5 were located both in the stroma tissue as well as slightly on the tumor cells. Anti-HER3-Cy5 was internalized into the tumor cells and Cetuximab-Cy5 was visualized on tumor cell surface (Fig. 6c,d). Only Trastuzumab-Cy5 showed a very high binding affinity to the overexpressed HER2 receptors (Fig. 6e) and should therefore execute the best therapeutic efficacy. In order to determine the

binding specificity and interaction of the different antibodies simultaneously, thereby allowing to reduce the number of animals, an antibody mixture with different fluorochromes, including: Cetuximab-Alexa488, anti-IGF1R-Alexa555, anti-HER3-Alexa647, and Trastuzumab-Alexa750; were injected in Calu3 bearing mice (Fig. 7). Since Alexa488 and Alexa555 are unsuitable for *in vivo* imaging application, because of the strong light absorption and low penetration depth, only *ex vivo* analysis of the receptor binding was performed. This example was also able to show that the different therapeutic antibodies are not impeding each other during receptor binding. This is an important aspect when considering and selecting potential combination of antibody therapies.

The treatment results of the different therapeutic antibodies in the Calu-3 xenograft model confirmed perfectly the predicted treatment effects form fluorescence imaging (see 4.1.4) and illustrated the problems of IHC receptor evaluation. In comparison to the Omalizumab treated control group (Fig. 8a,b), Trastuzumab induced a complete tumor growth inhibition and reduced tumor cell proliferation to a minimum (Fig. 8a,f). The Cetuximab and anti-HER3 therapy reduced the proliferation rate of the tumor cell (Fig. 8d,e) and therefore slowed down the tumor growth (Fig. 8a). Only the anti-IGF1R antibody, as expected by fluorescence imaging, had no influence on the tumor cell proliferation rate and the tumor growth at all (Fig. 8a,c).

A characterization of the antibody-target interaction and the resultant therapeutic efficacy of all four different receptors could be perfectly evaluated by fluorescence imaging. Thereby, only the HER2-Trastuzumab combination was prioritized as an appropriate target for anti-tumoral therapy in the Calu-3 xenograft model. In contrast to this, conventional immunohistochemistry selected three of the four receptors as appropriate targets for a preclinical efficacy study. This example convincingly illustrates the great potential of *in vivo* and *ex vivo* multispectral fluorescence imaging for the selection of antibodies targeting a tumor cell associated cell surface antigen. In addition, "*in vivo* histology" circumvents the problems associated with fixation and antigen retrieval. The direct visualization of the antibody-target interaction provides the possibility to answer further questions, which are relevant for the preclinical antibody development process.

Epitope mapping and evaluation of binding specificity

Another important question which was addressed by fluorescence imaging in a xenograft model is the evaluation of the binding site and specificity of antibodies targeting the same tumor cell receptor. The *in vivo* analysis of both parameters enables on one hand the selection of the antibody format with the highest target affinity and specificity and on the other hand to find out if different receptor epitopes are recognized. The determination of those parameters by *in vitro* methods (such as ELISA, FACS or surface plasmon resonance) cannot sufficiently reflect the complex *in vivo* situation and therefore provide only an artificial outcome.

The proof-of-concept for this *in vivo* fluorescence analysis was performed with the two therapeutic antibodies Trastuzumab (Herceptin) and Pertuzumab (Perjeta) in Calu-3 xenograft model. Both HER2 specific antibodies were selected for this purpose, because they bind to different HER2 receptor epitopes, showed clear therapeutic effects in preclinical [246] and clinical studies [247], and are also approved as a combination therapy with Docetaxel in first-line treatment of patients with metastatic HER2-positive mamma carcinomas [248, 249]. The usage of such excellent characterized and therapeutic relevant antibodies is perfectly suitable

for the validation of fluorescence imaging, because it can be verified if those specific and clinically relevant antibody characteristics, such as the epitope mapping and binding specificity, can be also received by *in vivo* and *ex vivo* fluorescence imaging.

In a first study, the binding specificity of both Cy5 labeled antibodies against the HER2 receptor was verified in the Calu-3 xenograft model (4.2.1). The *in vivo* imaging results and the subsequent *ex vivo* analysis determined comparable signal intensities and identical target binding for Trastuzumab-Cy5 and Pertuzumab-Cy5 (Fig.9). Therefore, both antibodies illustrated an identical affinity and specificity towards the HER2 receptor, but the study could not determine if both antibodies detect the same or different receptor epitopes. To investigate this issue, different experimental groups of the Calu-3 xenograft model were pre-treated with unlabeled Trastuzumab, Pertuzumab, and the combination of both antibodies to cover the corresponding binding sites of the HER2 receptor. The subsequent application of fluorescent labeled Trastuzumab and Pertuzumab enabled the evaluation of the related target epitope. At this the aligned combination of T / T-Cy5, P / P-Cy5, T / P / T-Cy5, and T / P / P-Cy5 (T = Trastuzumab, P = Pertuzumab) showed no specific receptor binding in the *in vivo* and *ex vivo* imaging analysis, because all free binding sites were covered due to the pre-incubation (Fig. 10). Only the combination of T / P-Cy5 and P / T-Cy5 provided strong *in vivo* fluorescence signals and a specific binding to the HER2 tumor cell receptors. This experimental setting enabled a clear *in vivo* and *ex vivo* differentiation of the binding epitopes from Trastuzumab and Pertuzumab. The same prior experimental setting in combination with the application of an antibody mixture of Trastuzumab-Alexa647 and Pertuzumab-Alexa750 provided similar imaging results and evaluated different target epitopes for both antibody formats. Further, the usage of an antibody mixture reduced the number of experimental animals and therefore support the 3R concept (3R = refine, replace, reduce) (Fig. 11). This experimental design can generally transferred and applied to any other antibody.

The high binding affinity and specificity of Trastuzumab and Pertuzumab to the HER2 receptor of Calu-3 xenograft resulted in a strong therapeutic treatment effect. In comparison to the control antibody Omalizumab, the monotherapy of both anti-HER2 antibodies induced complete tumor growth stagnation (Fig. 12a) and reduced the proliferation rate of Calu-3 tumor cells to a minimum (Fig. 12b-d).

The perfect application of fluorescence imaging for the evaluation of the antibody binding site and specificity was also used to characterize a new anti-HER2 bispecific antibody format (Crossmab) (see 4.2.2). This heterodimeric antibody combines the binding sites of Trastuzumab and Pertuzumab in a single IgG format and therefore should provide the same target specificity and therapeutic treatment efficacy. No visible differences regarding binding specificity could be ascertained in a direct comparison between Trastuzumab-Cy5, Pertuzumab-Cy5, and the new Crossmab-Cy5 format at all (Fig. 13). In addition, the epitope evaluation via fluorescence imaging could perfectly show that both arms of the Crossmab antibody possess a more or less identical affinity and specificity to the different HER2 epitopes (Fig. 14). Therefore it was ensured, that the new bispecific antibody format provides the same binding properties as the combination of Trastuzumab and Pertuzumab and thus, should develop comparable therapeutic treatment effects in the Calu-3 xenograft model. The subsequent preclinical efficacy study confirmed this issue, whereas no significant differences between the single

Crossmab and the combination therapy with Trastuzumab and Pertuzumab were detectable (Fig. 15).

These different examples clearly verify that the combination of fluorescence *in vivo* and *ex vivo* imaging is a very efficient and powerful tool for the evaluation of the binding site, affinity, and specificity of monoclonal antibodies. These parameters are the cornerstones for the successful selection of antibodies targeting a tumor antigen. In addition, fluorescence imaging provides a profound understanding regarding the antibody-target interaction which will help to prioritize the most suitable drug candidate more efficiently.

Selection of the most suitable Xenograft

The description of the interaction mechanism between antibody and antigen by fluorescence imaging can also be applied to select a suitable xenograft model for preclinical efficacy studies. This issue is an important aspect in preclinical drug development, because only an appropriate *in vivo* model, where the target of interest is overexpressed during the treatment period possesses the ability to reveal treatment effects of new therapeutic compounds in a clear and sufficient way. The direct *in vivo* assessment of target expression using fluorescent labeled antibodies can help to overcome major problems of conventional immunohistochemistry, such as inefficient antigen retrieval and the difficult selection of an appropriate non-therapeutic detection antibody; by searching the relevant tumor target with the associated labeled therapeutic agent in the “natural” *in vivo* environment.

The xenograft selection through *in vivo* and *ex vivo* fluorescence imaging was conducted with the therapeutic antibodies Trastuzumab-Cy5 (anti-HER2) and Omalizumab-Cy5 (anti-IgE) in two different NSCLC xenograft models (Calu-1 and Calu-3), whereas Omalizumab served as a negative control (see 4.2). At this the Calu-1 xenograft was not selected as a suitable tumor model for further preclinical efficacy studies because of a missingTrastuzumab-Cy5 binding to the tumor cells. In contrast, Trastuzumab-Cy5 possesses a very strong *in vivo* fluorescence intensity and a high affinity and specificity to the tumor cell receptor of the Calu-3 xenograft model, as already discussed in the prior sections (Fig. 16b,d,e).

The results received from the xenograft prioritization and created on the basis of fluorescence imaging, could be verified in the subsequent preclinical efficacy study. As predicted by the fluorescence imaging results, Trastuzumab exerted no therapeutic effect in the Calu-1 xenograft model, whereas the tumor growth inhibition in the Calu-3 xenograft was clearly evident (Fig. 17). Therefore, *in vivo* and *ex vivo* fluorescence imaging is a valuable tool for the prioritization and selection of the most suitable xenograft model.

Identification of the optimal treatment dosage

Another important parameter for conducting a preclinical efficacy study is the identification of the optimal treatment dosage, which should assure the highest possible therapeutic treatment effect and should develop no or only very low side-effects in the experimental animal. For the conventional determination of this parameter different dosages of the antibodies are tested in a xenograft model and the most effective dosage with the lowest side-effects will be selected for subsequent preclinical experiments. Another option to receive this parameter is blood sampling at different time points to quantify mab concentration in the serum. This conventional procedure is extremely time-consuming, laborious, and requires a large amount

of experimental animals, because the measurement of serum concentrations at different time points cannot be made in the same animal. Furthermore, blood analysis can only determine the circulating antibody concentration but it provides no information about the effective antibody concentration in the tumor region.

To overcome the limitations of conventional blood sampling techniques, fluorescence *in vivo* and *ex vivo* imaging was used to select the optimal treatment dosage of Trastuzumab for a preclinical efficacy study in Calu-3 xenograft model (see 4.4). For this purpose, several Calu-3 bearing animal groups were pre-treated with different concentration of Trastuzumab (0, 1, 3, 10 and 20 mg/kg) to cause a gradient of HER2 receptor coverage. After 24 hours of incubation fluorescent labeled Trastuzumab-Cy5 was injected to determine the free HER2 binding sides in the tumor region. In comparison to the control antibody Omalizumab-Cy5, which had no specific binding side and circulates through the tumor tissue, only a pre-incubation with 20 mg/kg Trastuzumab showed the ability to penetrated the whole tumor area, cover all free HER2 receptors, and prevent the specific binding of Trastuzumab-Cy5 to the tumor cells (Fig. 18). From this one can infer that a treatment dosage of 1, 3, and 10 mg/kg Trastuzumab would not cover all free HER2 receptors and therefore increases the potential for an inefficient treatment efficacy. A sufficient and overall HER2 receptor coverage in Calu-3 tumors (depending on the tumor size), will only be accomplished with a treatment dosage of about 20 mg/kg Trastuzumab. The conducted preclinical efficacy study with different treatment dosages (0, 1, 3, 10 and 20 mg/kg) confirmed the gained imaging results, whereas the treatment dosage of 20 mg/kg Trastuzumab achieved constant tumor growth inhibition at all (Fig. 19).

Therefore, the combination of *in vivo* and *ex vivo* fluorescence imaging allowed determining the optimal Trastuzumab concentration for the treatment of Calu-3 xenograft. The predicted antibody dosage of 20 mg/kg achieved the best therapeutic treatment effects during the preclinical efficacy study.

Identification of the best application time point and scheduling

Beside the determination of the optimal treatment dosage of a therapeutic antibody, the identification of the optimal application time point is another important aspect for preclinical efficacy studies. The complete coverage of all tumor cell receptors by the therapeutic agent is a pre-requisite for a successful tumor therapy. The penetration behavior of therapeutic antibodies in the tumor tissue depends on different tumor factors (such as vessel architecture, tumor micro environment, interstitial tumor pressure, and tumor cell receptor expression) as well as on the antibody design (e.g. antibody format, receptor affinity, and half-life). Monitoring and understanding the complex interaction of these factors is very difficult and partly still impossible. The conventional way to receive the optimal application time point for a therapeutic antibody is the preclinical testing of a pre-defined treatment dosage at different application intervals. Since this method is very laborious and time-consuming and, above all, requires a large number of animals, *in vivo* and *ex vivo* fluorescence imaging was also used to determine this important parameter (see 4.5).

For this, the pharmacokinetic behavior (tumor penetration, receptor binding, and clearance) of different therapeutic dosages of Trastuzmab-Cy5 (1, 3, 10, 20, and 30 mg/kg) were monitored in the Calu-3 tumor region (Fig. 20). For the therapeutic dosages of 1 and 3 mg/kg Trastuzumab-Cy5, a single antibody application is not sufficient to cover all surface receptors

the tumor area. To receive an effective tumor response the treatment dosage must be increased (> 10 mg/kg) or a short daily application interval should be selected to accumulate and increase the antibody concentration in the tumor region. For the tumor treatment with 10 and 20 mg/kg Trastuzumab-Cy5 an application interval of approx. 7 days could be predicted. When applying a treatment dosage of 30 mg/kg Trastuzumab-Cy5 a further injection should at least follow after 14 days. These imaging results were compared to the obtained tumor growth curves of the individual treatment groups, and perfectly confirmed the gained imaging prognosis (Fig. 21).

In this example *in vivo* fluorescence imaging was able to produce reliable predictions about the most suitable application time points for different therapeutic Trastuzumab dosages in Calu-3 xenograft model. It further showed the great benefit of fluorescence imaging for preclinical antibody development.

Non-invasive pharmacokinetic drug measurement

The traditional determination of pharmacokinetic parameters through blood sample analysis requires a large number of experimental animals requiring in a laborious, time-consuming, and cost-intensive workflow. The results obtained can only mirror the circulating compound concentration in the blood stream, but it gives no direct indication about the distribution and accumulation into different organs. Furthermore, since the animal protection act prohibits serial blood sampling on high frequencies, the measurement of different PK time points cannot be made in the same animal. The resultant variability of experimental animals and blood sampling time points can influence the outcome of pharmacokinetic studies and therefore makes this method prone for misinterpretation. Especially the exact determination of the peak serum concentration (C_{max}) and the time to reach that point (t_{max}), after rapid escalation of the compound concentration in the blood stream through intravenous application, is difficult to detect by conventional blood sampling techniques.

The current thesis overcomes the problems of conventional blood sampling by using planar reflectance imaging to non-invasively detect the pharmacokinetic behavior of fluorescent labeled substances through the eye of anesthetized mice. The utility of this eye imaging approach was clearly demonstrated by evaluating three different compounds: i) indocyanine green (ICG) a non-targeting fluorescence dye; ii) Pamidronate (OsteoSense750) a fluorescent labeled bisphosphonate targeting bone tissue; and iii) Alexa750 labeled Trastuzumab, which targets the HER2 antigen expressed on the surface of tumor cells (see 4.6).

The proof-of-concept for this eye imaging method was carried out using ICG, because this molecule provides a short half-life and a fast clearance rate and is therefore eminently suitable for repeated application in the same experimental animal. The non-invasive fluorescence measurement through the animals eye correctly determined the pharmacokinetic properties of ICG (t_{max} = 10 sec, $t_{1/2}$ = 1.2 min) as already described in the literature [228, 229] (see 4.6.1, Fig. 22). Furthermore, the measurement of repeated injections of equal ICG dosages in the same experimental animal showed the reproducibility of the method (see 4.6.2, Fig.23). The received curve shapes and the values for t_{max} (13, 15, and 15 sec) were nearly identical and showed only slight value variations. The increased serum half-life values of the three repeated application (1.8, 2.2, and 2.5 min) reflects a cumulative dose-effect of ICG and may be attributed to the limited clearing capacity of the mouse liver [250]. In addition to it, the ability

to detect dose dependencies of escalating ICG dosages was also determined by fluorescence eye imaging (see 4.6.3, Fig. 24).

After the successful validation of this new imaging method, eye imaging was combined with whole-body fluorescence imaging to become a comprehensive overview about serum kinetics, organ distribution, and clearance of ICG, OsteoSence750 and Trastuzumab-Alexa750. The received ICG measurement results confirmed the eye imaging data of the prior ICG experiment (Fig. 22) regarding t_{max} and $t_{1/2}$ and further showed the accumulation and clearance of the compound by the liver, which was already described in the literature (see 4.6.4, Fig. 25) [228, 230-232]. The slight t_{max} differences of both measurements can be attributed to the manual injection of the compound. A constant and reproducible compound application could be achieved by an automatic injection device and should therefore reduce value variations to a minimum.

In a further study, the combination of eye and whole body imaging enables the simultaneous detection of serum kinetics and organ distribution of OsteoSence750 (see 4.6.5, Fig. 26). The measured serum half-life ($t_{1/2}$ = 34 min) and the accumulation of the labeled bone targeting agent to the skeleton of the mouse are in accordance with published data [233-236].

In the last and most important experiment, the serum pharmacokinetic, biodistribution, accumulation, and clearance of Trastuzumab-Alexa750 were determined in a tumor free and Calu-3 bearing mouse (see 4.6.6, Fig. 27). The fluorescence imaging results gained from the tumor free mouse confirmed the serum half-life of Trastuzumab-Alexa750 ($t_{1/2}$ = 2.5 days) to already published pharmacokinetic data of other IgG1 antibodies (Fig. 27a,d) [237-240]. In contrast, the serum antibody concentration in the Calu-3 tumor bearing mouse (HER2 overexpressing) was reduced significantly faster and thus, lead to a shorter serum half-life of only 1.2 days (Fig. 27b,d). This effect could be attributed to the target mediated blood clearance of labeled Trastuzumab by the HER2 receptor. Specific binding of Trastuzumab-Alexa750 to the HER2 target, as shown by *ex vivo* fluorescence microscopy (Fig. 27c), reduces the circulating antibody concentration and consequently lead to a much faster blood clearance.

By means of the several prior imaging examples the proof-of-concept for the feasibility of pharmacokinetic eye measurements was clearly indicated. Furthermore, the combination of eye and whole-body imaging enables not only a non-invasive and longitudinal measurement of the pharmacokinetic profile of fluorescent labeled substances through the eye, but rather to capture their biodistribution pattern (e.g. penetration, accumulation, and clearance) in subcutaneous tumor models. The short acquisition times of this non-invasive fluorescence imaging technique (ranging from milliseconds to seconds), open up the possibility for fast and real-time measurements up to several hours in the same experimental animal and can therefore provide a continuous pharmacokinetic curve shape and a more detailed analysis of the compound behavior.

In addition to the non-invasive pharmacokinetic *in vivo* examination of new fluorescent labeled antibodies and fragments, their target specific binding behavior, in contrast to PET and/or SPECT imaging probes, can directly visualized in histological tissue slices on a cellular level. The possible combination and colocalization of fluorescence microscopy and conventional immunohistochemistry data sets, enables a very detailed analysis of the drug-target

interaction and the consequential therapeutic treatment effect. This favorable combination of *in vivo* and *ex vivo* fluorescence imaging methods permit a very simple, fast, and economic generation of diagnostically conclusive data and can therefore crucially contribute to a better understanding of tumor biology and therapeutic treatment effects.

3D visualization of tumor morphology, drug penetration, and treatment response

The aforementioned examples excellently demonstrate, how the combination of fluorescent labeled antibodies and fluorescence imaging modalities provide detailed insights into the pharmacokinetic behavior and interaction between antibodies and their target structures. *In vivo* and *ex vivo* multispectral fluorescence analysis complements each other in a perfect way. Macroscopic pharmacokinetic *in vivo* parameters from living mice can be connected with microscopic endpoint information at cellular resolution. However, the latter is strongly limited to small tumor volume when using conventional imaging methods such as epi-fluorescence microscopy, confocal laser-scanning microscopy and/or multi-photon laser-scanning microscopy. Therefore, a holistic analysis of the inhomogeneous tumor biology cannot be executed with those modalities. To overcome this problem and bridge the gap between conventional macroscopic and microscopic fluorescence imaging modalities, multispectral fluorescence ultramicroscopy was transferred into the field of tumor biology for the three-dimensional analysis of large post-mortem specimen at cellular resolution (see 4.7).

In a first step, a convenient UM protocol for the optimal tumor sample preparation was created, including sufficient tissue dehydration and clearing. The optimized clearing procedure provided excellent tissue transparency, even without the perfusion of the experimental animals (see 4.7.3, Fig. 32a). Optimal sample clearing in combination with the usage of NIR Alexa fluorochromes, which possess high quantum efficiency, reduced the tissue absorption and scattering of the excitation and emission light to a minimum and increased the penetration depth. Furthermore, the resultant high signal-to-noise ratio reduced the exposure time of a single fluorescence channel down to 100-500 milliseconds per slice and allowed the measurement of whole tumor samples in 10 to 20 minutes depending on the size. Optimal sample preparation and hardware configuration enables the measurement of sample diameter up to 6 mm with an almost isotropic resolution of 5.1 µm. In addition, it was also verified that the clearing procedure did not give rise to any appreciable reduction of the fluorescence signals in the tumor samples, which was confirmed with a direct comparison to frozen and paraffin sections. The clearance of the tumor samples showed also no recognizable influence on the performance of conventional immunohistochemical staining procedures. Various routine tissue staining's, such as H&E, Ki67, CD34, and HER2, could be conducted without any problems subsequently after UM measurements and illustrated perfect staining results. Furthermore, a direct comparison of the virtual data sets created by ultramicroscopy and conventionally IHC staining demonstrated an excellent morphological and anatomical correlation. Both the tissue morphology and vessel architecture of the tumor and the penetration and binding of the therapeutic antibody corresponded perfectly (see 4.7.3, Fig. 32b-j). This outstanding combination possibility of fluorescent based *in vivo* and *ex vivo* imaging and classical histology, enables a comprehensive assessment and detailed analysis of biological issues from a macroscopic down to a microscopic scale.

The proof-of-concept study for multispectral fluorescence UM imaging in tumor analysis was performed in the orthotopic KPL-4 breast cancer xenograft model. Herein, the three-

dimensional visualization of multiple tumor parameters, such as tumor vasculature and antibody penetration, was evaluated (see 4.7.1). The imaging results obtained could perfectly visualize the chaotic, irregular, and dramatically branched vascular structures by using the vessel marker Lectin-Alexa647 (Fig. 29) and the heterogeneous penetration and binding behavior of Trastuzumab-Alexa750 (Fig. 30) in single virtual UM slices and also as a MIP and 3D volume rendering (see 4.7.1.2 and 4.7.1.3). In addition, the measurement of the tumor tissue autofluorescence provided detailed morphological tissue information. It opens up the possibility to distinguish vital and necrotic tissue sections and also to visualize tumor areas with high erythrocyte accumulation (see 4.7.1.1, Fig.28). The directed combination and superposition of these multispectral information enables a profound analysis and the comprehension of potential relationships between the different tumor and/or drug parameters (see 4.7.1.4, Fig. 31). For example, the overlapping of the vascular and antibody channels clearly showed the relationship between the density and morphology of the tumor vessels and the antibody penetration. Highly vascularized areas of the tumor displayed a very strong and homogeneous antibody distribution, whereas areas with low vascular density were only slightly or not at all penetrated (Fig. 31b,c).

The fully automated analysis of the various tumor parameters was carried out with a novel set of custom-developed image analysis algorithms which were implemented into a quantification software (see 4.7.4). This new quantification tool enables the segmentation of different parameters from each fluorescence channel and analyzed their specific value without any manual user interference. Beside the determination of the total, vital, and necrotic tumor tissue volume, a detailed analysis of the tumor vessel architecture and antibody penetration behavior was for the first time realized in a three-dimensional way (Fig. 33). The complete quantification process for all parameters took less than two hours per tumor on a single processor, whereas the number of concurrent tumor quantifications is only limited by available hardware resources. Multiple engines can run simultaneously if enough hardware resources and Definiens licenses are available and thus enabling the timely and fully automatic quantification of large groups. This aspect allows a very rapid, detailed, and cost-efficient implementation and analysis of preclinical studies on a large scale. Furthermore, therapeutic effects can be detected at a very early stage with this new technology, which substantially reduces the times required for animal experiments.

This new imaging and quantification method in combination with conventional IHC was used to quantitatively monitor the anti-angiogenic treatment effect of Bevacizumab at different time points in the KPL-4 xenograft model and further investigated the influence of vessel normalization on the subsequent penetration of labeled Trastuzumab (see 4.7.5). A therapeutic effect of Bevacizumab on the tumor vessels could be detected by UM even one day after therapy initiation (see 4.7.5.1). In contrast to the chaotic and inhomogeneous vascularity of the untreated control group, Bevacizumab clearly induced a normalization and homogenization of the vessel architecture [242] and significantly reduced the vessel volume, number of vessels segments, and branching points in the tumor periphery, whereas these parameters remained virtually unchanged in the center of the tumor (Fig. 36). The normalized vessel network obviously induced an improved blood supply to the tumor, reduced the interstitial fluid pressure [243], and therefore provided a more constant supply of oxygen and nutrients [159]. These effects may led in the KPL-4 xenograft model to an evenly distributed tumor cell proliferation (Fig. 38g,h) and reduced the necrotic areas in the treatment group (day

7) by an average of 69% (Fig. 36c and Fig. 38). Such a “normalized” tumor environment should highly benefit from an additional chemotherapy, because the homogeneous and normalized vessel network offer the small chemical compound a perfect and evenly access to the proliferating tumor cells. In the clinical situation, Bevacizumab in combination with chemotherapy was associated with an significant increase in progression-free survival and overall response rates in the first-line treatment of advanced gastric, metastatic colorectal and breast cancer [251-253].

Subsequently, it was also investigated by UM how Bevacizumab pre-treatment influences the penetration behavior of Trastuzumab-Alexa750 into tumor tissue (see 4.7.5.2). The results of this study clearly indicated, that anti-angiogenic pre-treatment significantly reduced the penetration of Trastuzumab from the tumor border to its center and also from the tumor vessels into the surrounding tumor tissue (Fig. 39). The diminished antibody penetration was attributed to the reduction in vascular permeability promoted by Bevacizumab. The reduced pore size of the normalized tumor vessels made it more difficult for Trastuzumab-Alexa750 to penetrate (due to its high molecular weight) and as a result more of the antibody was confined to the vessel compartment [244] (Fig. 41). Histological examination revealed that anti-angiogenic pre-treatment did not affect the HER2 expression level. Both groups (PBS and Bevacizumab treated) demonstrated a high extracellular HER2 expression (3+) on the tumor cells surface and thus internalization and/or shedding of the extracellular receptor domains was eliminated as relevant factors for reduced antibody presence in the tumor tissue (Fig. 40).

Beside the extensive evaluation and validation of ultramicroscopy for tumor analysis, this imaging technique was further applied to visualize the morphological nature of different mouse organs, such as the lymph node, kidney, and eye (see 4.7.6). The usage of tissue autofluorescence and the vessel marker Lectin-Alexa647 enabled a correct and detailed anatomical characterization of the different mouse organs (Fig. 42-44). Especially the low absorption and scattering of NIR light and the resultant high signal-to-noise ratio provided also great insights into specimen which are difficult to clear, such as the kidney.

Hence and in summary these examples clearly demonstrate that multispectral fluorescence ultramicroscopy is a very powerful tool for preclinical cancer research and drug development, gaining unprecedented insights into biology. This new imaging technology, in combination with our novel quantification software, enables the three-dimensional visualization and quantification of multiple parameters in large specimen at cellular resolution and therefore bridges the gap between current *in vivo* imaging methods and conventional two-dimensional histology. The simultaneous three-dimensional detection of tumor parameters and therapeutic molecules provide a unique, accurate, and holistic overview of tumor progression and opens up the possibility to study in detail the drug penetration, accumulation, drug-target interaction, and resultant therapeutic treatment effects. This aspect is absolutely crucial, as we can only really gain a proper representative insight if we can capture and observe the heterogeneous tumor biology as a whole. Furthermore, this imaging modality can be also applied to monitor abnormal tissue changes in different organs of the experimental animal and therefore can give some indications of unwanted side effects of new compounds and/or treatment strategies. A profound understanding of these complex biological mechanisms allows us to efficiently design new drugs and enables a fast and purposeful selection of suitable drug candidates.

6 Conclusion

The development of target specific biologics, including therapeutic antibodies, is a very complex and cost-intensive process requiring long development periods ranging from 8-12 years and is associated with high attrition rates. Numerous approaches for improvements have been proposed to find a way out of „The Valley of Death in anti-cancer drug development“ and how to select the most suitable drug candidate more effectively. In addition, established and standard procedures of the preclinical antibody development process, such as conventional immunohistochemistry and/or blood sampling techniques, are limited in their analytical ability and need to be optimized. In the present thesis the problems of the established standard procedures have been addressed and tried to overcome the existing limitations by using fluorescent labeled antibodies in combination with *in vivo* and *ex vivo* fluorescence imaging modalities. These inexpensive, fast, easy to handle, and radiation-free imaging techniques were already applied in preclinical cancer research and drug development to answer different biological questions. Nevertheless, a detailed and profound examination of the potential of these fluorescence imaging methods in the application field of preclinical monoclonal antibody development was initially verified in the present work.

The imaging results of the conducted tumor xenograft experiments could clearly demonstrate that fluorescence imaging is a very efficient and powerful tool for the determination of relevant parameters in preclinical antibody development. The combination of eye and whole-body fluorescence imaging enables not only a non-invasive, longitudinal, and high throughput measurement of the pharmacokinetic serum profile of fluorescent labeled substances through the animals eye, but rather to capture their biodistribution, penetration, accumulation, and clearance in subcutaneous tumor xenografts. The short acquisition times of this non-invasive fluorescence imaging technique (ranging from milliseconds to seconds), allows the possibility for fast and real-time measurements up to several hours in the same experimental animal and can therefore provide a continuous pharmacokinetic curve shape and a more detailed analysis of the pharmacokinetic behavior of the compound. The semiquantitative acquisition of the different parameter is a clear disadvantage of fluorescence molecular imaging compared to nuclear imaging techniques, such as PET and SPECT. However, beside this negative aspect, near-infrared fluorescence imaging unifies all important aspects of a perfect imaging modality, including: simple, fast, cheap, non-radioactive, high throughput measurement, multispectral detection, and simple labeling technique. This begs the question if semiquantitative fluorescence imaging, especially form subcutaneous tumor xenograft models, may not sufficient enough for an expedient decision making. The present work shows perfectly the correlation between the predictions of the semiquantitative imaging results and the subsequently performed preclinical efficacy studies.

In addition to the non-invasive pharmacokinetic *in vivo* examination of new fluorescent labeled antibodies, their target specific binding behavior, in contrast to PET and/or SPECT imaging probes, can be directly visualized in histological tissue slices on a cellular level. Especially the simultaneous and multispectral measurement of different tumor events and/or a therapeutic antibodies mixture are not feasible with radioactive isotopes. In comparison to conventional IHC analysis - which is strongly dependent on tissue fixation, antigen retrieval procedures and

uses non-therapeutic, paraffin penetrating detection antibodies for target assessment - this "*in vivo* fluorescence histology" method is closer orientated to preclinical reality. The specific binding of the labeled therapeutic antibodies to the relevant tumor targets are monitored in their "natural" environment and therefore provides a much better prediction about the preclinical efficacy outcome. The direct comparison of both methods clearly demonstrated the advantage of fluorescence imaging in selecting the most suitable antibody candidate with the best therapeutic treatment effect.

To overcome the limitation of single tissue slice analysis of histological tumor section, multispectral fluorescence ultramicroscopy was successfully transferred into the field of tumor biology. The utilization of this post-mortem imaging technique in combination with a novel quantification software enables for the first time the three-dimensional visualization and automatic quantification of multiple tumor parameters and antibody penetration in large optical transparent specimen at cellular resolution. This new method bridges the gap between current *in vivo* imaging techniques – such as computed tomography – and conventional two-dimensional histology. The simultaneous three-dimensional detection of relevant tumor parameter and therapeutic molecules provide a unique, accurate, and comprehensive overview of tumor biology and offers the possibility to study the drug penetration, accumulation, drug-target interaction, and resultant therapeutic treatment effects in much more detail. Furthermore, this imaging modality can be also applied to monitor abnormal tissue changes in different organs of the experimental animal and therefore can give valuable information regarding unwanted side effects of new compounds and/or treatment strategies.

The *in vivo* and *ex vivo* fluorescence analysis complements each other in a perfect way, whereby macroscopic pharmacokinetic *in vivo* parameter from living experimental animals can be connected with microscopic endpoint information at cellular resolution. The combination of both imaging methods allows to perfectly determine important parameters for the preclinical antibody development process, such as: (I) the evaluation of the tumor cell receptor expression, (II) epitope mapping, and (III) the binding affinity and specificity of monoclonal antibodies. Furthermore, these modalities simplifies the prioritization of the best therapeutic antibody, select the most suitable xenograft model, and determine the optimal treatment dosage and application time point for a preclinical efficacy study. The obtained imaging results correlated perfectly with the corresponding preclinical efficacy data. Detailed analysis of already approved therapeutic monoclonal antibodies (Trastuzumab and Pertuzumab) could clearly demonstrate the clinical relevance of the performed imaging experiments.

This favorable combination of *in vivo* and *ex vivo* fluorescence imaging methods permits a very simple, fast, and economic generation of diagnostically conclusive data and can therefore crucially contribute to a better understanding of tumor biology and therapeutic treatment effects. A profound understanding of these complex biological mechanisms allows us to efficiently design, characterize, and optimize new drugs and treatment strategies. Furthermore, it contributes to decision making and enables a fast and purposeful selection of the most suitable drug candidate. Such new and innovative techniques will help to accelerate and enhance the various stages of preclinical drug development and provides a method to design new biologics more cost effective. Further improvement and refinement of the preclinical selection process and the reinforcement of knowledge regarding disease biology and therapeutic treatment effects, will increase the success rate of new therapeutic agents in early clinical trials and may also reduce high attrition rates.

7 List of References

1. Trotta, F., et al., *Evaluation of Oncology Drugs at the European Medicines Agency and US Food and Drug Administration: When Differences Have an Impact on Clinical Practice.* Journal of Clinical Oncology, 2011. 29(16): p. 2266-2272.
2. Malvezzi, M., et al., *European cancer mortality predictions for the year 2013.* Annals of Oncology, 2013. 24(3): p. 792-800.
3. Hicklin, D.J., et al., *Monoclonal antibody strategies to block angiogenesis.* Drug discovery today, 2001. 6(10): p. 517-528.
4. Clynes, R.A., et al., *Inhibitory Fc receptors modulate in vivo cytoxicity against tumor targets.* Nature Medicine, 2000. 6(4): p. 443-446.
5. Xin, L., et al., *Human monoclonal antibodies in cancer therapy: a review of recent developments.* Frontiers in bioscience : a journal and virtual library, 2013. 18: p. 765-72.
6. Tabrizi, M.A., C.M.L. Tseng, and L.K. Roskos, *Elimination mechanisms of therapeutic monoclonal antibodies.* Drug discovery today, 2006. 11(1-2): p. 81-88.
7. Weiner, L.M., R. Surana, and S. Wang, *Monoclonal antibodies: versatile platforms for cancer immunotherapy.* Nature Reviews Immunology, 2010. 10(5): p. 317-327.
8. Woof, J.M. and D.R. Burton, *Human antibody - Fc receptor interactions illuminated by crystal structures.* Nature Reviews Immunology, 2004. 4(2): p. 89-99.
9. Ward, E.S., et al., *From sorting endosomes to exocytosis: Association of Rab4 and Rab11 GTPases with the fc receptor, FcRn, during recycling.* Molecular Biology of the Cell, 2005. 16(4): p. 2028-2038.
10. Ezzell, C., *Magic bullets.* Scientific American, 2001. 285(4): p. 34-41.
11. Holliger, P. and P.J. Hudson, *Engineered antibody fragments and the rise of single domains.* Nature Biotechnology, 2005. 23(9): p. 1126-1136.
12. Gebauer, M. and A. Skerra, *Engineered protein scaffolds as next-generation antibody therapeutics.* Current Opinion in Chemical Biology, 2009. 13(3): p. 245-255.
13. Penichet, M.L. and S.L. Morrison, *Antibody-cytokine fusion proteins for the therapy of cancer.* Journal of Immunological Methods, 2001. 248(1-2): p. 91-101.
14. Park, J.W., et al., *Anti-HER2 immunoliposomes: Enhanced efficacy attributable to targeted delivery.* Clinical Cancer Research, 2002. 8(4): p. 1172-1181.
15. Brekke, O.H. and G.A. Loset, *New technologies in therapeutic antibody development.* Current Opinion in Pharmacology, 2003. 3(5): p. 544-550.
16. Carter, P., *Improving the efficacy of antibody-based cancer therapies.* Nature Reviews Cancer, 2001. 1(2): p. 118-129.
17. Zhou, H. and M.A. Mascelli, *Mechanisms of Monoclonal Antibody-Drug Interactions*, in *Annual Review of Pharmacology and Toxicology, Vol 51, 2011*, A.K. Cho, Editor 2011. p. 359-372.
18. Munro, T.P., et al., *Bridging the gap: facilities and technologies for development of early stage therapeutic mAb candidates.* MAbs, 2011. 3(5): p. 440-52.
19. DiMasi, J.A. and H.G. Grabowski, *Economics of new oncology drug development.* Journal of Clinical Oncology, 2007. 25(2): p. 209-216.
20. Kola, I. and J. Landis, *Can the pharmaceutical industry reduce attrition rates?* Nature Reviews Drug Discovery, 2004. 3(8): p. 711-715.
21. Moreno, L. and A.D.J. Pearson, *How can attrition rates be reduced in cancer drug discovery?* Expert Opinion on Drug Discovery, 2013. 8(4): p. 363-368.
22. Tonkens, R., *An overview of the drug development process.* Physician executive, 2005. 31(3): p. 48-52.
23. Scannell, J.W., et al., *Diagnosing the decline in pharmaceutical R&D efficiency.* Nature Reviews Drug Discovery, 2012. 11(3): p. 191-200.
24. Swinney, D.C. and J. Anthony, *How were new medicines discovered?* Nature Reviews Drug Discovery, 2011. 10(7): p. 507-519.
25. Williams, M., *Productivity Shortfalls in Drug Discovery: Contributions from the Preclinical Sciences?* Journal of Pharmacology and Experimental Therapeutics, 2011. 336(1): p. 3-8.

26. Pammolli, F., L. Magazzini, and M. Riccaboni, *The productivity crisis in pharmaceutical R&D.* Nature Reviews Drug Discovery, 2011. 10(6): p. 428-438.
27. Paul, S.M., et al., *How to improve R&D productivity: the pharmaceutical industry's grand challenge.* Nature Reviews Drug Discovery, 2010. 9(3): p. 203-214.
28. Hait, W.N., *Anticancer drug development: the grand challenges.* Nature Reviews Drug Discovery, 2010. 9(4): p. 253-254.
29. Adams, D.J., *The Valley of Death in anticancer drug development: a reassessment.* Trends in Pharmacological Sciences, 2012. 33(4): p. 173-180.
30. Goodwin, R., et al., *Targeted agents: How to select the winners in preclinical and early clinical studies?* European Journal of Cancer, 2012. 48(2): p. 170-178.
31. Garrett, M.D., et al., *The contemporary drug development process: advances and challenges in preclinical and clinical development.* Progress in cell cycle research, 2003. 5: p. 145-58.
32. Bunnage, M.E., *Getting pharmaceutical R&D back on target.* Nature Chemical Biology, 2011. 7(6): p. 335-339.
33. Bibby, M.C., *Orthotopic models of cancer for preclinical drug evaluation: advantages and disadvantages.* European Journal of Cancer, 2004. 40(6): p. 852-857.
34. Damia, G. and M. D'Incalci, *Contemporary pre-clinical development of anticancer agents - What are the optimal preclinical models?* European Journal of Cancer, 2009. 45(16): p. 2768-2781.
35. Suggitt, M. and M.C. Bibby, *50 years of preclinical anticancer drug screening: Empirical to target-driven approaches.* Clinical Cancer Research, 2005. 11(3): p. 971-981.
36. Peterson, J.K. and P.J. Houghton, *Integrating pharmacology and in vivo cancer models in preclinical and clinical drug development.* European Journal of Cancer, 2004. 40(6): p. 837-844.
37. Yap, T.A., et al., *Envisioning the future of early anticancer drug development.* Nature Reviews Cancer, 2010. 10(7): p. 514-U25.
38. Walker, I. and H. Newell, *Do molecularly targeted agents in oncology have reduced attrition rates?* Nature Reviews Drug Discovery, 2009. 8(1): p. 15-16.
39. Condeelis, J. and R. Weissleder, *In Vivo Imaging in Cancer.* Cold Spring Harbor Perspectives in Biology, 2010. 2(12).
40. Krucker, T. and B.S. Sandanaraj, *Optical imaging for the new grammar of drug discovery.* Philosophical Transactions of the Royal Society a-Mathematical Physical and Engineering Sciences, 2011. 369(1955): p. 4651-4665.
41. Seddon, B.M. and P. Workman, *The role of functional and molecular imaging in cancer drug discovery and development.* British Journal of Radiology, 2003. 76: p. S128-S138.
42. Willmann, J.K., et al., *Molecular imaging in drug development.* Nature Reviews Drug Discovery, 2008. 7(7): p. 591-607.
43. Pysz, M.A., S.S. Gambhir, and J.K. Willmann, *Molecular imaging: current status and emerging strategies.* Clinical Radiology, 2010. 65(7): p. 500-516.
44. Weissleder, R. and M.J. Pittet, *Imaging in the era of molecular oncology.* Nature, 2008. 452(7187): p. 580-589.
45. Matthews, P.M., et al., *Positron emission tomography molecular imaging for drug development.* British Journal of Clinical Pharmacology, 2012. 73(2): p. 175-186.
46. Gomes, C.M., et al., *Molecular imaging with SPECT as a tool for drug development.* Advanced Drug Delivery Reviews, 2011. 63(7): p. 547-554.
47. Ntziachristos, V., et al., *Looking and listening to light: the evolution of whole-body photonic imaging.* Nature Biotechnology, 2005. 23(3): p. 313-320.
48. Rudin, M. and R. Weissleder, *Molecular imaging in drug discovery and development.* Nature Reviews Drug Discovery, 2003. 2(2): p. 123-131.
49. Massoud, T.F. and S.S. Gambhir, *Molecular imaging in living subjects: seeing fundamental biological processes in a new light.* Genes & Development, 2003. 17(5): p. 545-580.
50. Hoppin, J., et al., *Assessing Antibody Pharmacokinetics in Mice with In Vivo Imaging.* Journal of Pharmacology and Experimental Therapeutics, 2011. 337(2): p. 350-358.
51. Weissleder, R., *Scaling down imaging: Molecular mapping of cancer in mice.* Nature Reviews Cancer, 2002. 2(1): p. 11-18.
52. Zysk, A.M., et al., *Optical coherence tomography: a review of clinical development from bench to bedside.* Journal of Biomedical Optics, 2007. 12(5).
53. Pogue, B.W. and Ieee, *Image-Guided Spectroscopy of Cancer: Translating Optical Technology into Clinical Tools*. 2012 Conference on Lasers and Electro-Optics2012.

54. Stokes, G.G., *On the change of refrangibility of light.* Philosophical Transactions of the Royal Society of London 1852. 142: p. 99.
55. Tung, C.H., *Fluorescent peptide probes for in vivo diagnostic imaging.* Biopolymers, 2004. 76(5): p. 391-403.
56. Lee, S., J. Xie, and X. Chen, *Peptides and Peptide Hormones for Molecular Imaging and Disease Diagnosis.* Chemical Reviews, 2010. 110(5): p. 3087-3111.
57. Lee, S., et al., *A near-infrared-fluorescence-quenched gold-nanoparticle imaging probe for in vivo drug screening and protease activity determination.* Angewandte Chemie-International Edition, 2008. 47(15): p. 2804-2807.
58. Ntziachristos, V., *Fluorescence molecular imaging.* Annual review of biomedical engineering, 2006. 8: p. 1-33.
59. Lee, S., J. Xie, and X. Chen, *Activatable Molecular Probes for Cancer Imaging.* Current Topics in Medicinal Chemistry, 2010. 10(11): p. 1135-1144.
60. Funovics, M., R. Weissleder, and C.H. Tung, *Protease sensors for bioimaging.* Analytical and Bioanalytical Chemistry, 2003. 377(6): p. 956-963.
61. Kobayashi, H. and P.L. Choyke, *Target-Cancer-Cell-Specific Activatable Fluorescence Imaging Probes: Rational Design and in Vivo Applications.* Accounts of Chemical Research, 2011. 44(2): p. 83-90.
62. Luo, S., et al., *A review of NIR dyes in cancer targeting and imaging.* Biomaterials, 2011. 32(29): p. 7127-7138.
63. Wang, Y. and L. Chen, *Quantum dots, lighting up the research and development of nanomedicine.* Nanomedicine-Nanotechnology Biology and Medicine, 2011. 7(4): p. 385-402.
64. Nurunnabi, M., et al., *Targeted near-IR QDs-loaded micelles for cancer therapy and imaging.* Biomaterials, 2010. 31(20): p. 5436-5444.
65. Nel, A., et al., *Toxic potential of materials at the nanolevel.* Science, 2006. 311(5761): p. 622-627.
66. Mancini, M.C., et al., *Oxidative quenching and degradation of polymer-encapsulated quantum dots: New insights into the long-term fate and toxicity of nanocrystals in vivo.* Journal of the American Chemical Society, 2008. 130(33): p. 10836-+.
67. Moore, M.N., *Do nanoparticles present ecotoxicological risks for the health of the aquatic environment?* Environment International, 2006. 32(8): p. 967-976.
68. Resch-Genger, U., et al., *Quantum dots versus organic dyes as fluorescent labels.* Nature Methods, 2008. 5(9): p. 763-775.
69. Ballou, B., L.A. Ernst, and A.S. Waggoner, *Fluorescence imaging of tumors in vivo.* Current Medicinal Chemistry, 2005. 12(7): p. 795-805.
70. Ishizawa, T., et al., *Real-Time Identification of Liver Cancers by Using Indocyanine Green Fluorescent Imaging.* Cancer, 2009. 115(11): p. 2491-2504.
71. Kosaka, N., et al., *Clinical implications of near-infrared fluorescence imaging in cancer.* Future Oncology, 2009. 5(9): p. 1501-1511.
72. Hawe, A., M. Sutter, and W. Jiskoot, *Extrinsic fluorescent dyes as tools for protein characterization.* Pharmaceutical Research, 2008. 25(7): p. 1487-1499.
73. Haughland, R.P., *Handbook of fluorescent probes and research products*. Vol. 9th edition 2002: Molecular Probes, Inc. 966.
74. Mishra, A., et al., *Cyanines during the 1990s: A review.* Chemical Reviews, 2000. 100(6): p. 1973-2011.
75. Dilek, G. and E.U. Akkaya, *Novel squaraine signalling Zn(II) ions: three-state fluorescence response to a single input.* Tetrahedron Letters, 2000. 41(19): p. 3721-3724.
76. Volkova, K.D., et al., *Spectroscopic study of squaraines as protein-sensitive fluorescent dyes.* Dyes and Pigments, 2007. 72(3): p. 285-292.
77. de la Torre, G., C.G. Claessens, and T. Torres, *Phthalocyanines: old dyes, new materials. Putting color in nanotechnology.* Chemical Communications, 2007(20): p. 2000-2015.
78. Kralova, J., et al., *Porphyrin-bile acid conjugates: from saccharide recognition in the solution to the selective cancer cell fluorescence detection.* Organic & Biomolecular Chemistry, 2008. 6(9): p. 1548-1552.
79. Donuru, V.R., et al., *Near-infrared emissive BODIPY polymeric and copolymeric dyes.* Polymer, 2010. 51(23): p. 5359-5368.
80. Hu, M., et al., *Hydroxyphthalocyanines as potential photodynamic agents for cancer therapy.* Journal of Medicinal Chemistry, 1998. 41(11): p. 1789-1802.

81. Chalfie, M., et al., *Green Fluorescent protein as a marker for gene-expression.* Science, 1994. 263(5148): p. 802-805.
82. Chudakov, D.M., S. Lukyanov, and K.A. Lukyanov, *Fluorescent proteins as a toolkit for in vivo imaging.* Trends in Biotechnology, 2005. 23(12): p. 605-613.
83. Giepmans, B.N.G., et al., *Review - The fluorescent toolbox for assessing protein location and function.* Science, 2006. 312(5771): p. 217-224.
84. Aoki, K., Y. Kamioka, and M. Matsuda, *Fluorescence resonance energy transfer imaging of cell signaling from in vitro to in vivo: Basis of biosensor construction, live imaging, and image processing.* Dev Growth Differ, 2013. 55(4): p. 515-22.
85. Aoki, K., et al., *Stable expression of FRET biosensors: A new light in cancer research.* Cancer Science, 2012. 103(4): p. 614-619.
86. Kamioka, Y., et al., *Live Imaging of Protein Kinase Activities in Transgenic Mice Expressing FRET Biosensors.* Cell Structure and Function, 2012. 37(1): p. 65-73.
87. Feng, G.P., et al., *Imaging neuronal subsets in transgenic mice expressing multiple spectral variants of GFP.* Neuron, 2000. 28(1): p. 41-51.
88. Tsukamoto, T., et al., *Visualization of gene activity in living cells.* Nature Cell Biology, 2000. 2(12): p. 871-878.
89. Zhang, S.F., C. Ma, and M. Chalfie, *Combinatorial marking of cells and organelles with reconstituted fluorescent proteins.* Cell, 2004. 119(1): p. 137-+.
90. Hillisch, A., M. Lorenz, and S. Diekmann, *Recent advances in FRET: distance determination in protein-DNA complexes.* Current Opinion in Structural Biology, 2001. 11(2): p. 201-207.
91. Patterson, G.H. and J. Lippincott-Schwartz, *A photoactivatable GFP for selective photolabeling of proteins and cells.* Science, 2002. 297(5588): p. 1873-1877.
92. Li, X.Q., et al., *Generation of destabilized green fluorescent protein transcription reporter.* Journal of Biological Chemistry, 1998. 273(52): p. 34970-34975.
93. Straight, A.F., et al., *GFP tagging of budding yeast chromosomes reveals that protein-protein interactions can mediate sister chromatid cohesion.* Current Biology, 1996. 6(12): p. 1599-1608.
94. Katz, M.H., et al., *A novel red fluorescent protein orthotopic pancreatic cancer model for the preclinical evaluation of chemotherapeutics.* Journal of Surgical Research, 2003. 113(1): p. 151-160.
95. Dooley, C.T., et al., *Imaging dynamic redox changes in mammalian cells with green fluorescent protein indicators.* Journal of Biological Chemistry, 2004. 279(21): p. 22284-22293.
96. Keyaerts, M., V. Caveliers, and T. Lahoutte, *Bioluminescence imaging: looking beyond the light.* Trends in Molecular Medicine, 2012. 18(3): p. 164-172.
97. Takeuchi, M., et al., *Ratiometric Bioluminescence Indicators for Monitoring Cyclic Adenosine 3',5'-Monophosphate in Live Cells Based on Luciferase-Fragment Complementation.* Analytical Chemistry, 2010. 82(22): p. 9306-9313.
98. Caysa, H., et al., *A redshifted codon-optimized firefly luciferase is a sensitive reporter for bioluminescence imaging.* Photochemical & Photobiological Sciences, 2009. 8(1): p. 52-56.
99. Branchini, B.R., et al., *Luciferase from the Italian firefly Luciola italica: Molecular cloning and expression.* Comparative Biochemistry and Physiology B-Biochemistry & Molecular Biology, 2006. 145(2): p. 159-167.
100. Viviani, V.R., et al., *Active-site properties of Phrixotrix railroad worm green and red bioluminescence-eliciting luciferases.* Journal of Biochemistry, 2006. 140(4): p. 467-474.
101. Mezzanotte, L., et al., *In Vivo Bioluminescence Imaging of Murine Xenograft Cancer Models with a Red-shifted Thermostable Luciferase.* Molecular Imaging and Biology, 2010. 12(4): p. 406-414.
102. Badr, C.E. and B.A. Tannous, *Bioluminescence imaging: progress and applications.* Trends in Biotechnology, 2011. 29(12): p. 624-633.
103. Gu, L., et al., *A new model for studying tissue-specific mdr1a gene expression in vivo by live imaging.* Proceedings of the National Academy of Sciences of the United States of America, 2009. 106(13): p. 5394-5399.
104. McMillin, D.W., et al., *Tumor cell-specific bioluminescence platform to identify stroma-induced changes to anticancer drug activity.* Nature Medicine, 2010. 16(4): p. 483-U171.
105. Prasad, G., et al., *Inhibition of PI3K/mTOR pathways in glioblastoma and implications for combination therapy with temozolomide.* Neuro-Oncology, 2011. 13(4): p. 384-392.

106. Lehmann, S., et al., *Longitudinal and multimodal in vivo imaging of tumor hypoxia and its downstream molecular events.* Proceedings of the National Academy of Sciences of the United States of America, 2009. 106(33): p. 14004-14009.
107. Scabini, M., et al., *In vivo imaging of early stage apoptosis by measuring real-time caspase-3/7 activation.* Apoptosis, 2011. 16(2): p. 198-207.
108. Laxman, B., et al., *Noninvasive real-time imaging of apoptosis.* Proceedings of the National Academy of Sciences of the United States of America, 2002. 99(26): p. 16551-16555.
109. Ke, S., et al., *Near-infrared optical imaging of epidermal growth factor receptor in breast cancer xenografts.* Cancer Research, 2003. 63(22): p. 7870-7875.
110. Weissleder, R., et al., *In vivo imaging of tumors with protease-activated near-infrared fluorescent probes.* Nature Biotechnology, 1999. 17(4): p. 375-378.
111. Yang, M., et al., *Whole-body optical imaging of green fluorescent protein-expressing tumors and metastases.* Proceedings of the National Academy of Sciences of the United States of America, 2000. 97(3): p. 1206-1211.
112. Leblond, F., et al., *Pre-clinical whole-body fluorescence imaging: Review of instruments, methods and applications.* Journal of Photochemistry and Photobiology B-Biology, 2010. 98(1): p. 77-94.
113. Gao, X.H., et al., *In vivo cancer targeting and imaging with semiconductor quantum dots.* Nature Biotechnology, 2004. 22(8): p. 969-976.
114. Keshava, N., *A survey of spectral unmixing algorithms.* Lincoln Laboratory Journal 2003. 14 (1): p. 23.
115. Ntziachristos, V., et al., *Planar fluorescence imaging using normalized data.* Journal of Biomedical Optics, 2005. 10(6).
116. Jobsis, F.F., *Noninvasive, infrared monitoring of cerebral and myocardial oxygen sufficiency and circulatory parameters.* Science, 1977. 198(4323): p. 1264-1267.
117. Muller, M.G., et al., *Intrinsic fluorescence spectroscopy in turbid media: disentangling effects of scattering and absorption.* Applied Optics, 2001. 40(25): p. 4633-4646.
118. Hilderbrand, S.A. and R. Weissleder, *Near-infrared fluorescence: application to in vivo molecular imaging.* Current Opinion in Chemical Biology, 2010. 14(1): p. 71-79.
119. Ntziachristos, V., J. Ripoll, and R. Weissleder, *Would near-infrared fluorescence signals propagate through large human organs for clinical studies? (vol 27, pg 333, 2002).* Optics Letters, 2002. 27(18): p. 1652-1652.
120. Ntziachristos, V., C. Bremer, and R. Weissleder, *Fluorescence imaging with near-infrared light: new technological advances that enable in vivo molecular imaging.* European Radiology, 2003. 13(1): p. 195-208.
121. Becker, A., et al., *Receptor-targeted optical imaging of tumors with near-infrared fluorescent ligands.* Nature Biotechnology, 2001. 19(4): p. 327-331.
122. Mahmood, U., et al., *Near-infrared optical imaging of protease activity for tumor detection.* Radiology, 1999. 213(3): p. 866-870.
123. Bullok, K.E., et al., *Biochemical and in vivo characterization of a small, membrane-permeant, caspase-activatable far-red fluorescent peptide for imaging apoptosis.* Biochemistry, 2007. 46(13): p. 4055-4065.
124. Li, X.D., et al., *Fluorescent diffuse photon: Density waves in homogeneous and heterogeneous turbid media: Analytic solutions and applications.* Applied Optics, 1996. 35(19): p. 3746-3758.
125. Ntziachristos, V. and R. Weissleder, *Charge-coupled-device based scanner for tomography of fluorescent near-infrared probes in turbid media.* Medical Physics, 2002. 29(5): p. 803-809.
126. Graves, E.E., et al., *A submillimeter resolution fluorescence molecular imaging system for small animal imaging.* Med Phys, 2003. 30(5): p. 901-11.
127. Ntziachristos, V. and R. Weissleder, *Experimental three-dimensional fluorescence reconstruction of diffuse media by use of a normalized Born approximation.* Optics Letters, 2001. 26(12): p. 893-895.
128. Ripoll, J., R.B. Schulz, and V. Ntziachristos, *Free-space propagation of diffuse light: Theory and experiments.* Physical Review Letters, 2003. 91(10).
129. Lasser, T., et al., *Surface reconstruction for free-space 360 degrees fluorescence molecular tomography and the effects of animal motion.* Ieee Transactions on Medical Imaging, 2008. 27(2): p. 188-194.
130. Schulz, R.B., J. Ripoll, and V. Ntziachristos, *Experimental fluorescence tomography of tissues with noncontact measurements.* Ieee Transactions on Medical Imaging, 2004. 23(4): p. 492-500.

131. Meyer, H., et al., *Noncontact optical imaging in mice with full angular coverage and automatic surface extraction.* Appl Opt, 2007. 46(17): p. 3617-27.
132. Deliolanis, N., et al., *Free-space fluorescence molecular tomography utilizing 360 degrees geometry projections.* Optics Letters, 2007. 32(4): p. 382-384.
133. Stuker, F., J. Ripoll, and M. Rudin, *Fluorescence Molecular Tomography: Principles and Potential for Pharmaceutical Research.* Pharmaceutics, 2011. 3(2): p. 45.
134. Soubret, A., J. Ripoll, and V. Ntziachristos, *Accuracy of fluorescent tomography in the presence of heterogeneities: Study of the normalized born ratio.* Ieee Transactions on Medical Imaging, 2005. 24(10): p. 1377-1386.
135. Arridge, S.R. and J.C. Schotland, *Optical tomography: forward and inverse problems.* Inverse Problems, 2009. 25(12).
136. Gaudette, R.J., et al., *A comparison study of linear reconstruction techniques for diffuse optical tomographic imaging of absorption coefficient.* Physics in Medicine and Biology, 2000. 45(4): p. 1051-1070.
137. Guven, M., et al., *Diffuse optical tomography with a priori anatomical information.* Physics in Medicine and Biology, 2005. 50(12): p. 2837-2858.
138. Ale, A., et al., *Imaging performance of a hybrid x-ray computed tomography-fluorescence molecular tomography system using priors.* Medical Physics, 2010. 37(5): p. 1976-1986.
139. Ntziachristos, V., *Going deeper than microscopy: the optical imaging frontier in biology.* Nature Methods, 2010. 7(8): p. 603-614.
140. Hyde, D., et al., *Hybrid FMT-CT imaging of amyloid-beta plaques in a murine Alzheimer's disease model.* Neuroimage, 2009. 44(4): p. 1304-1311.
141. Ale, A., et al., *FMT-XCT: in vivo animal studies with hybrid fluorescence molecular tomography-X-ray computed tomography.* Nature Methods, 2012. 9(6): p. 615-+.
142. Ntziachristos, V., et al., *Concurrent MRI and diffuse optical tomography of breast after indocyanine green enhancement.* Proceedings of the National Academy of Sciences of the United States of America, 2000. 97(6): p. 2767-2772.
143. Koenig, A., et al., *In vivo mice lung tumor follow-up with fluorescence diffuse optical tomography.* Journal of Biomedical Optics, 2008. 13(1).
144. Ntziachristos, V., et al., *Fluorescence molecular tomography resolves protease activity in vivo.* Nature Medicine, 2002. 8(7): p. 757-60.
145. von Wallbrunn, A., et al., *In vivo imaging of integrin alpha nu beta(3) expression using fluorescence-mediated tomography.* European Journal of Nuclear Medicine and Molecular Imaging, 2007. 34(5): p. 745-754.
146. Ntziachristos, V., et al., *Visualization of antitumor treatment by means of fluorescence molecular tomography with an annexin V-Cy5.5 conjugate.* Proceedings of the National Academy of Sciences of the United States of America, 2004. 101(33): p. 12294-12299.
147. Pittet, M.J. and R. Weissleder, *Intravital Imaging.* Cell, 2011. 147(5): p. 983-991.
148. Jain, R.K., L.L. Munn, and D. Fukumura, *Dissecting tumour pathophysiology using intravital microscopy.* Nature Reviews Cancer, 2002. 2(4): p. 266-276.
149. Zomer, A., et al., *Real-time intravital imaging of cancer models.* Clinical & Translational Oncology, 2011. 13(12): p. 848-854.
150. Yuan, F., et al., *Vascular-permeability and microcirculation of gliomas and mammary carcinomas transplanted in rat and mouse cranial windows.* Cancer Research, 1994. 54(17): p. 4564-4568.
151. Brown, E.B., et al., *In vivo measurement of gene expression, angiogenesis and physiological function in tumors using multiphoton laser scanning microscopy (vol 7, pg 864, 2001).* Nature Medicine, 2001. 7(9): p. 1069-1069.
152. Nugent, L.J. and R.K. Jain, *Extravascular diffusion in normal and neoplastic tissues.* Cancer Research, 1984. 44(1): p. 238-244.
153. Leu, A.J., et al., *Absence of functional lymphatics within a murine sarcoma: A molecular and functional evaluation.* Cancer Research, 2000. 60(16): p. 4324-4327.
154. Fukumura, D., et al., *Effect of host microenvironment on the microcirculation of human colon adenocarcinoma.* American Journal of Pathology, 1997. 151(3): p. 679-688.
155. Tsuzuki, Y., et al., *Pancreas microenvironment promotes VEGF expression and tumor growth: Novel window models for pancreatic tumor angiogenesis and microcirculation.* Laboratory Investigation, 2001. 81(10): p. 1439-1451.

156. Monsky, W.L., et al., *Role of host microenvironment in angiogenesis and microvascular functions in human breast cancer xenografts: mammary fat pad versus cranial tumors.* Clinical Cancer Research, 2002. 8(4): p. 1008-1013.
157. Gavins, F.N.E., *Intravital microscopy: new insights into cellular interactions.* Current Opinion in Pharmacology, 2012. 12(5): p. 601-607.
158. Helmchen, F. and W. Denk, *Deep tissue two-photon microscopy.* Nature Methods, 2005. 2(12): p. 932-940.
159. Fukumura, D., et al., *Tumor Microvasculature and Microenvironment: Novel Insights Through Intravital Imaging in Pre-Clinical Models.* Microcirculation, 2010. 17(3): p. 206-225.
160. Huisken, J., et al., *Optical sectioning deep inside live embryos by selective plane illumination microscopy.* Science, 2004. 305(5686): p. 1007-1009.
161. Huang, D., et al., *Optical coherance tomography.* Science, 1991. 254(5035): p. 1178-1181.
162. Yun, S.H., et al., *High-speed optical frequency-domain imaging.* Optics Express, 2003. 11(22): p. 2953-2963.
163. Vakoc, B.J., et al., *Cancer imaging by optical coherence tomography: preclinical progress and clinical potential.* Nature Reviews Cancer, 2012. 12(5): p. 363-368.
164. Razansky, D., et al., *Deep Tissue Optical and Optoacoustic Molecular Imaging Technologies for Pre-Clinical Research and Drug Discovery.* Current Pharmaceutical Biotechnology, 2012. 13(4): p. 504-522.
165. Berk, D.A., et al., *Direct in vivo measurement of targeted binding in a human tumor xenograft*. Proceedings of the National Academy of Sciences of the United States of America, 1997. 94(5): p. 1785-1790.
166. Martin, G.R. and R.K. Jain, *Noninvasive measurement of interstitial pH profiles in normal and neoplastic tissue unsing fluorescnece ration imaging microscopy.* Cancer Research, 1994. 54(21): p. 5670-5674.
167. Zhang, J., et al., *Genetically encoded reporters of protein kinase A activity reveal impact of substrate tethering.* Proceedings of the National Academy of Sciences of the United States of America, 2001. 98(26): p. 14997-15002.
168. van Roessel, P. and A.H. Brand, *Imaging into the future: visualizing gene expression and protein interactions with fluorescent proteins.* Nature Cell Biology, 2002. 4(1): p. E15-E20.
169. Hoffman, R.M., *Visualization of GFP-expressing tumors and metastasis in vivo.* Biotechniques, 2001. 30(5): p. 1016-+.
170. Fukumura, D., et al., *Tumor necrosis factor alpha-induced leukocyte adhesion in normal and tumor vessels: effect of tumor type, transplantation site, and host strain.* Cancer Res, 1995. 55(21): p. 4824-9.
171. Vakoc, B.J., et al., *Three-dimensional microscopy of the tumor microenvironment in vivo using optical frequency domain imaging.* Nature Medicine, 2009. 15(10): p. 1219-U151.
172. Padera, T.P., et al., *Conventional and high-speed intravital multiphoton laser scanning microscopy of microvasculature, lymphatics, and leukocyte-endothelial interactions.* Molecular imaging, 2002. 1(1): p. 9-15.
173. Hoshida, T., et al., *Imaging steps of lymphatic metastasis reveals that vascular endothelial growth factor-C increases metastasis by increasing delivery of cancer cells to lymph nodes: Therapeutic implications.* Cancer Research, 2006. 66(16): p. 8065-8075.
174. Stroh, M., et al., *Quantum dots spectrally distinguish multiple species within the tumor milieu in vivo.* Nature Medicine, 2005. 11(6): p. 678-682.
175. Chary, S.R. and R.K. Jain, *Direct measurement of interstitial convection and diffusion of albumin in normal and neoplastic tissue by fluorescnece photobleaching.* Proceedings of the National Academy of Sciences of the United States of America, 1989. 86(14): p. 5385-5389.
176. Bonapace, L., et al., *If You Don't Look, You Won't See: Intravital Multiphoton Imaging of Primary and Metastatic Breast Cancer.* Journal of Mammary Gland Biology and Neoplasia, 2012. 17(2): p. 125-129.
177. Siedentopf, H. and R. Zsigmondy, *Über Sichtbarmachung und Größenbestimmung ultramikoskopischer Teilchen, mit besonderer Anwendung auf Goldrubingläser.* Annals of Physics 1902. 315: p. 39.
178. Voie, A.H., D.H. Burns, and F.A. Spelman, *Orthogonal-plane fluorescnece optical sectioning: 3-dimensional imaging of macroscpic biological speciment.* Journal of Microscopy-Oxford, 1993. 170: p. 229-236.

179. Fuchs, E., et al., *Thin laser light sheet microscope for microbial oceanography.* Optics Express, 2002. 10(2): p. 145-154.
180. Dodt, H.-U., et al., *Ultramicroscopy: three-dimensional visualization of neuronal networks in the whole mouse brain.* Nature Methods, 2007. 4(4): p. 331-336.
181. Menzel, R., *Ultramicroscopy - imaging a whole animal or a whole brain with micron resolution.* Frontiers in neuroscience, 2011. 5: p. 11-11.
182. Jahrling, N., K. Becker, and H.-U. Dodt, *3D-reconstruction of blood vessels by ultramicroscopy.* Organogenesis, 2009. 5(4): p. 145-8.
183. Tomer, R., K. Khairy, and P.J. Keller, *Shedding light on the system: Studying embryonic development with light sheet microscopy.* Current Opinion in Genetics & Development, 2011. 21(5): p. 558-565.
184. Spalteholz, W., *Über das Durchsichtigmachen von menschlichen und tierischen Präparaten*1914: Leipzig, S. Hirzel.
185. Genina, E.A., A.N. Bashkatov, and V.V. Tuchin, *Tissue optical immersion clearing.* Expert Review of Medical Devices, 2010. 7(6): p. 825-842.
186. Ertürk, A. and F. Bradke, *High-resolution imaging of entire organs by 3-dimensional imaging of solvent cleared organs (3DISCO).* Experimental neurology, 2013. 242: p. 57-64.
187. Dent, J.A., A.G. Polson, and M.W. Klymkowsky, *A whole-mount immunohistochemical analysis of the expression of the intermediate filament protein vimentin in xenopus.* Development, 1989. 105(1): p. 61-74.
188. Keller, P.J. and E.H.K. Stelzer, *Quantitative in vivo imaging of entire embryos with Digital Scanned Laser Light Sheet Fluorescence Microscopy.* Current Opinion in Neurobiology, 2008. 18(6): p. 624-632.
189. Huisken, J. and D.Y.R. Stainier, *Selective plane illumination microscopy techniques in developmental biology.* Development, 2009. 136(12): p. 1963-1975.
190. Scherz, P.J., et al., *High-speed imaging of developing heart valves reveals interplay of morphogenesis and function.* Development, 2008. 135(6): p. 1179-1187.
191. Keller, P.J., et al., *Fast, high-contrast imaging of animal development with scanned light sheet-based structured-illumination microscopy.* Nature Methods, 2010. 7(8): p. 637-U55.
192. Holekamp, T.F., D. Turaga, and T.E. Holy, *Fast three-dimensional fluorescence imaging of activity in neural populations by objective-coupled planar illumination microscopy.* Neuron, 2008. 57(5): p. 661-672.
193. Ertürk, A., et al., *Three-dimensional imaging of the unsectioned adult spinal cord to assess axon regeneration and glial responses after injury.* Nature Medicine, 2012. 18(1): p. 166-171.
194. Brede, C., et al., *Mapping immune processes in intact tissues at cellular resolution.* Journal of Clinical Investigation, 2012. 122(12): p. 4439-4446.
195. Cohen, C.M., *A path to improved pharmaceutical productivity.* Nature Reviews Drug Discovery, 2003. 2(9): p. 751-753.
196. Frank, R. and R. Hargreaves, *Clinical biomarkers in drug discovery and development.* Nature Reviews Drug Discovery, 2003. 2(7): p. 566-580.
197. Weissleder, R. and V. Ntziachristos, *Shedding light onto live molecular targets.* Nature Medicine, 2003. 9(1): p. 123-128.
198. Luker, G.D. and K.E. Luker, *Optical imaging: Current applications and future directions.* Journal of Nuclear Medicine, 2008. 49(1): p. 1-4.
199. Czernin, J., W.A. Weber, and H.R. Herschman, *Molecular imaging in the development of cancer therapeutics*, in *Annual Review of Medicine*2006. p. 99-118.
200. Contag, C.H. and P.R. Contag, *Illuminating drug discovery.* Chemistry & Industry, 1999(17): p. 664-666.
201. Hagen, A., et al., *Late-fluorescence mammography assesses tumor capillary permeability and differentiates malignant from benign lesions.* Optics Express, 2009. 17(19): p. 17016-17033.
202. van de Ven, S., et al., *A Novel Fluorescent Imaging Agent for Diffuse Optical Tomography of the Breast: First Clinical Experience in Patients.* Molecular Imaging and Biology, 2010. 12(3): p. 343-348.
203. Tromberg, B.J., et al., *Assessing the future of diffuse optical imaging technologies for breast cancer management.* Medical Physics, 2008. 35(6): p. 2443-2451.
204. Ell, C., *Improving endoscopic resolution and sampling: fluorescence techniques.* Gut, 2003. 52: p. 30-33.

205. DaCosta, R.S., B.C. Wilson, and N.E. Marcon, *Light-induced fluorescence endoscopy of the gastrointestinal tract.* Gastrointestinal endoscopy clinics of North America, 2000. 10(1): p. 37-vi.
206. Jichlinski, P., *New diagnostic strategies in the detection and staging of bladder cancer.* Current Opinion in Urology, 2003. 13(5): p. 351-355.
207. Gahlen, J., et al., *Improving diagnostic staging laparoscopy using intraperitoneal lavage of delta-aminolevulinic acid (ALA) for laparoscopic fluorescence diagnosis.* Surgery, 1999. 126(3): p. 469-473.
208. Gahlen, J., et al., *Laparoscopic fluorescence diagnosis for intraabdominal fluorescence targeting of peritoneal carcinosis experimental studies.* Annals of Surgery, 2002. 235(2): p. 252-260.
209. Lee, B.T., et al., *The FLARE Intraoperative Near-Infrared Fluorescence Imaging System: A First-in-Human Clinical Trial in Perforator Flap Breast Reconstruction.* Plastic and Reconstructive Surgery, 2010. 126(5): p. 1472-1481.
210. Tagaya, N., et al., *Intraoperative identification of sentinel lymph nodes by near-infrared fluorescence imaging in patients with breast cancer.* American Journal of Surgery, 2008. 195(6): p. 850-853.
211. van Dam, G.M. and V. Ntziachristos, *Current Concepts and Future Perspectives on Intraoperative Fluorescence Imaging in Cancer: Clinical Need.* Current Medical Imaging Reviews, 2012. 8(3): p. 233-243.
212. van Dam, G.M., et al., *Intraoperative tumor-specific fluorescence imaging in ovarian cancer by folate receptor-alpha targeting: first in-human results.* Nature Medicine, 2011. 17(10): p. 1315-U202.
213. Nunn, A.D., *The cost of developing imaging agents for routine clinical use (vol 41, pg 206, 2006).* Investigative Radiology, 2006. 41(5): p. CP2-CP2.
214. Hoffman, J.M., S.S. Gambhir, and G.J. Kelloff, *Regulatory and reimbursement challenges for molecular imaging.* Radiology, 2007. 245(3): p. 645-660.
215. Homann, H., *Implementation of a 3D thinning algorithm.* The Insight Journal, 2007. July-December: p. 4.
216. Pollard, K., et al., *Fixation, processing, and immunochemical reagent effects on preservation of T-lymphocyte surface membrane antigens in paraffin-embedded tissue.* Journal of Histochemistry & Cytochemistry, 1987. 35(11): p. 1329-1338.
217. Williams, J.H., B.L. Mepham, and D.H. Wright, *Tissue preparation for immunocytochemistry.* Journal of Clinical Pathology, 1997. 50(5): p. 422-428.
218. von Wasielewski, R., et al., *Influence of fixation, antibody clones, and signal amplification on steroid receptor analysis.* The Breast Journal, 2003. 4(1): p. 7.
219. Atkins, D., et al., *Immunohistochemical detection of EGFR in paraffin-embedded tumor tissues: Variation in staining intensity due to choice of fixative and storage time of tissue sections.* Journal of Histochemistry & Cytochemistry, 2004. 52(7): p. 893-901.
220. van den Broek, L. and M.J. van de Vijver, *Assessment of problems in diagnostic and research immunohistochemistry associated with epitope instability in stored paraffin sections.* Applied Immunohistochemistry & Molecular Morphology, 2000. 8(4): p. 316-321.
221. Wester, K., et al., *Paraffin section storage and immunohistochemistry - Effects of time, temperature, fixation, and retrieval protocol with emphasis on p53 protein and MIB1 antigen.* Applied Immunohistochemistry & Molecular Morphology, 2000. 8(1): p. 61-70.
222. Engel, K.B. and H.M. Moore, *Effects of Preanalytical Variables on the Detection of Proteins by Immunohistochemistry in Formalin-Fixed, Paraffin-Embedded Tissue.* Archives of Pathology & Laboratory Medicine, 2011. 135(5): p. 537-543.
223. Tubbs, R.R., et al., *Discrepancies in clinical laboratory testing of eligibility for trastuzumab therapy: Apparent immunohistochemical false-positives do not get the message.* Journal of Clinical Oncology, 2001. 19(10): p. 2714-2721.
224. Hashizume, K., et al., *Interlaboratory comparison in HercepTest assessment of HER2 protein status in invasive breast carcinoma fixed with various formalin-based fixatives.* Applied Immunohistochemistry & Molecular Morphology, 2003. 11(4): p. 339-344.
225. Schaefer, W., et al., *Immunoglobulin domain crossover as a generic approach for the production of bispecific IgG antibodies.* Proceedings of the National Academy of Sciences of the United States of America, 2011. 108(27): p. 11187-11192.

226. Croasdale, R., et al., *Development of tetravalent IgG1 dual targeting IGF-1R-EGFR antibodies with potent tumor inhibition.* Archives of Biochemistry and Biophysics, 2012. 526(2): p. 206-218.
227. Krejsa, C., M. Rogge, and W. Sadee, *Protein therapeutics: new applications for pharmacogenetics.* Nat Rev Drug Discov, 2006. 5(6): p. 507-21.
228. Desmettre, T., J.M. Devoisselle, and S. Mordon, *Fluorescence properties and metabolic features of indocyanine green (ICG) as related to angiography.* Survey of Ophthalmology, 2000. 45(1): p. 15-27.
229. Saxena, V., M. Sadoqi, and J. Shao, *Polymeric nanoparticulate delivery system for Indocyanine green: Biodistribution in healthy mice.* International Journal of Pharmaceutics, 2006. 308(1-2): p. 200-204.
230. Paumgartner, G., *The handling of indocyanine green by the liver.* Schweizerische medizinische Wochenschrift, 1975. 105(17 Suppl): p. 1-30.
231. Shinohara, H., et al., *Direct measurement of hepatic indocyanine green clearance with near-infrared spectroscopy: Separate evaluation of uptake and removal.* Hepatology, 1996. 23(1): p. 137-144.
232. Dorshow, R.B., et al., *Noninvasive fluorescence detection of hepatic and renal function.* Journal of Biomedical Optics, 1998. 3(3): p. 340-5.
233. Zaheer, A., et al., *In vivo near-infrared fluorescence imaging of osteoblastic activity.* Nature Biotechnology, 2001. 19(12): p. 1148-1154.
234. Pongchaidecha, M. and P.T. Daleyyates, *Clearance and tissue uptake following 4-hour and 24-hour infusions of pamidronate in rats.* Drug Metabolism and Disposition, 1993. 21(1): p. 100-104.
235. Hoffman, A., et al., *Mode of administration-dependent pharmacokinetics of bisphosphonates and bioavailability determination.* International Journal of Pharmaceutics, 2001. 220(1-2): p. 1-11.
236. Kumar, D., et al., *Evaluation of biodistribution by local versus systemic administration of Tc-99m-labeled pamidronate.* Journal of Orthopaedic Science, 2006. 11(5): p. 512-520.
237. Covell, D.G., et al., *Pharmacokinetics of monoclonal immunoglobulin G1, F(ab')2, and Fab' in mice.* Cancer Research, 1986. 46(8): p. 3969-3978.
238. Burvenich, I.J.G., et al., *Biodistribution and planar gamma camera imaging of I-123- and I-131-labeled F(ab ')(2) and Fab fragments of monoclonal antibody 14C5 in nude mice bearing an A549 lung tumor.* Nuclear Medicine and Biology, 2007. 34(3): p. 257-265.
239. Milenic, D.E., et al., *Targeting HER2 A report on the in vitro and in vivo pre-clinical data supporting trastuzumab as a radioimmunoconjugate for clinical trials.* MAbs, 2010. 2(5): p. 550-564.
240. Heskamp, S., et al., *Optimization of IGF-1R SPECT/CT Imaging Using In-111-Labeled F(ab ')(2) and Fab Fragments of Article the Monoclonal Antibody R1507.* Molecular Pharmaceutics, 2012. 9(8): p. 2314-2321.
241. Lee, T.C., R.L. Kashyap, and C.N. Chu, *Building skeleton models via 3-D medial surface/axis thinning algorithms.* Cvgip-Graphical Models and Image Processing, 1994. 56(6): p. 462-478.
242. Jain, R.K., *Normalization of tumor vasculature: An emerging concept in antiangiogenic therapy.* Science, 2005. 307(5706): p. 58-62.
243. Tong, R.T., et al., *Vascular normalization by vascular endothelial growth factor receptor 2 blockade induces a pressure gradient across the vasculature and improves drug penetration in tumors.* Cancer Research, 2004. 64(11): p. 3731-3736.
244. Pastuskovas, C.V., et al., *Effects of Anti-VEGF on Pharmacokinetics, Biodistribution, and Tumor Penetration of Trastuzumab in a Preclinical Breast Cancer Model.* Molecular Cancer Therapeutics, 2012. 11(3): p. 752-762.
245. Bassett, E.A., et al., *Conditional deletion of activating protein 2 alpha (AP-2 alpha) in the developing retina demonstrates non-cell-autonomous roles for AP-2 alpha in optic cup development.* Molecular and Cellular Biology, 2007. 27(21): p. 7497-7510.
246. Scheuer, W., et al., *Strongly Enhanced Antitumor Activity of Trastuzumab and Pertuzumab Combination Treatment on HER2-Positive Human Xenograft Tumor Models.* Cancer Research, 2009. 69(24): p. 9330-9336.
247. Vogel, C.L., et al., *Efficacy and safety of trastuzumab as a single agent in first-line treatment of HER2-overexpressing metastatic breast cancer.* Journal of Clinical Oncology, 2002. 20(3): p. 719-726.

248. Baselga, J. and S.M. Swain, *CLEOPATRA: A Phase III Evaluation of Pertuzumab and Trastuzumab for HER2-Positive Metastatic Breast Cancer.* Clinical Breast Cancer, 2010. 10(6): p. 489-491.
249. Baselga, J., et al., *Pertuzumab plus Trastuzumab plus Docetaxel for Metastatic Breast Cancer.* New England Journal of Medicine, 2012. 366(2): p. 109-119.
250. Wenger, G.R., *CUMULATIVE DOSE-RESPONSE CURVES IN BEHAVIORAL PHARMACOLOGY.* Pharmacology Biochemistry and Behavior, 1980. 13(5): p. 647-651.
251. Ohtsu, A., et al., *Bevacizumab in Combination With Chemotherapy As First-Line Therapy in Advanced Gastric Cancer: A Randomized, Double-Blind, Placebo-Controlled Phase III Study.* Journal of Clinical Oncology, 2011. 29(30): p. 3968-3976.
252. Hochster, H.S., *Bevacizumab in combination with chemotherapy: First-line treatment of patients with metastatic colorectal cancer.* Seminars in Oncology, 2006. 33(5): p. S8-S14.
253. Montagna, E., et al., *Metronomic Chemotherapy Combined With Bevacizumab and Erlotinib in Patients With Metastatic HER2-Negative Breast Cancer: Clinical and Biological Activity.* Clinical Breast Cancer, 2012. 12(3): p. 207-214.

8 List of Abbreviations

Terms and reagents

AAALAC	Association for assessment and accreditation of laboratory animal care
ATCC	American type culture collection
BLI	Bioluminescence imaging
bin	Binning
BODIPY	Borondipyrromethane
CCD	Charge-coupled device
CLSM	Confocal laser-scanning microscopy
CMOS	Complementary metal oxide semiconductor
CO_2	Carbon dioxide
CPU	Computer processing unit
CT	Computer tomography
Cy	Cyanine
DAB	3,3´-Diaminobenzidin
DAPI	4´,6-Diamidin-2´-phenylindol
dH_2O	destilliertes Wasser
DMEM	Dulbecco´s Modifiziertes Eagle Medium
DNA	Deoxyribonucleic acid
ECD	Extracellular domain
EDTA	Ethylenediaminetetraacetic acid
EGFR	Epidermal growth factor receptor
FCS	Fetal calf serum
FDA	Food and drug administration
Felasa	Federation for laboratory animal science associations
FISH	Fluoreszenz-in-situ-Hybridisierung
FMT	Fluorescence molecular tomography
FOV	Field of view
FP	Fluorescent protein
FRET	Fluorescence resonance energy transfer
FRI	Fluorescence reflectance imaging
GFP	Green fluorescent protein
GV-Solas	Society for laboratory animal science (Germany)
H&E	Hematoxylin & Eosin
HER	Human epidermal growth receptor
HRP	Horseradish peroxidase

H_2O	Water
IGFR	Insulin-like growth factor rezeptor
Ig	Immunoglobulin
IHC	Immunohistochemistry
i.p.	Intraperitoneal
IR	Infrared
ITK	Insight segmentation and registration toolkit
i.v.	Intravenös
LCTF	Liquid crystal tunable filter
LSFM	light-sheet based fluorescence microscopy
mAb	Monoclonal antibody
max	Maximum
min	Minimum
MPM	Multi-photon microscopy
MRT	Magnetic resonance tomography
NHS	N-Hydroxy-succinimidester
NIRF	Near-infrared fluorescence
NK	Natural killer
OI	Optical imaging
OPFOS	Orthogonal-plane fluorescence optical sectioning
PBS	Phosphate buffered saline
PET	Positron-emission tomography
PHASIS	Pharmacology animal study information system
RAM	Random access memory
ROI	Region of interest
ROI	Reactive oxygen species
RPMI	Roswell Park Memorial Institute
RT	Room temperature
s.c.	Subcutaneous
SCID	Severe combined immunodeficiency
SHO	Severe combined immunodeficiency hairless outbred
SPECT	Single-photon-emission computed tomography
SPF	Specific pathogenic free
SPIM	Selective plane illumination microscopy
SPR	Surface plasmon resonance
SD	Standard deviation
TBST	Tris buffered saline and Tween 20
THF	Tetrahydrofuran
TierSchG	Animal protection act (Germany)

TLSM	Thin-light sheet microscopy
UM	Ultramicroscopy
U.S.	United States
USD	United states dollar
WHO	World health organization

Units

°C	Degree centigrade
cm^2	Square centimeter
cm^3	Cubic centimeter
g	Gram
GB	Gigabyte
GHz	Gigahertz
h	Hour
kDa	Kilodalton
kg	Kilogram
l	Liter
mg	Milligram
min	Minutes
ml	Milliliter
mM	Millimole
mm	Millimeter
mm^3	Cubic millimeter
ms	Millisecond
nm	Nanometer
rpm	Rotations per minute
sec	Second
µg	Microgram
µl	Microliter
µm	Micrometer
%	Percentage
2D	Two-dimensional
3D	Three-dimensional

9 List of Figures

10 List of Tables

11 List of Videos